ABSTRACT

Title of Dissertation: NITROGEN-VACANCY CENTER MAGNETOMETRY FOR CONDENSED MATTER SYSTEMS

Shantam Ravan
Doctor of Philosophy, 2026

Dissertation Directed by: Professor Ronald L. Walsworth
Department of Physics

Nitrogen-vacancy (NV) centers in diamond are atomic-scale quantum sensors that combine nanoscale spatial resolution with quantitative magnetic-field readout under ambient conditions. This dissertation develops and applies NV magnetometry to three problems in nanoscale magnetism, in each case extending the sensing technique and using it to access physics that is difficult to reach by other means.

We first use spatially resolved NV magnetometry to image the nonlinear scattering dynamics of driven magnons in a yttrium iron garnet (YIG) thin film. A two-tone wave-mixing protocol isolates the elementary four-magnon interaction and extracts its strength directly from the spatial growth profile of the scattering product. Under strong single-tone driving, the system organizes into a spontaneous cascade of discrete, power-tunable parametric resonances whose growth is maximized where the magnon group velocity vanishes, resolving the pre-thermal approach to equilibrium as a structured hierarchy of discrete scattering channels rather than a diffusive continuum.

Second, we introduce a spectrum analyzer based on qubit dressed states that extends NV noise magnetometry beyond the conventional Rabi-rate limit. Embedding an off-resonant microwave probe in a dynamical-decoupling sequence uses the AC Stark shift to parametrically mix the probe with the target noise, so the accessible center frequency is set by the probe rather than the pulse repetition rate. We validate the method against a commercial spectrum analyzer and use it to extract the thermal magnon noise spectrum and group velocity in a YIG thin film at frequencies hundreds of megahertz above the NV resonance.

Third, we apply NV-ensemble magnetic-field imaging to artificial spin ice for the first time, mapping the stray fields of a pinwheel array through a field-driven reversal at room temperature with a diamond microchip placed directly on the sample. The maps resolve the full reversal of the superferromagnetic domain structure, from a uniform configuration through the nucleation, growth, and coalescence of mesoscopic domains to the reversed state, and show that the reversal is stochastic yet nucleates at the same locations.

Together, these projects extend NV magnetometry along three axes: spatial imaging of nonlinear many-body dynamics, the frequency range of noise spectroscopy, and confocal imaging of patterned magnetic systems. They help to establish NV magnetometry as a quantitative, noninvasive probe of magnetism at the nanoscale.

NITROGEN-VACANCY CENTER MAGNETOMETRY FOR CONDENSED MATTER SYSTEMS

by

Shantam Ravan

Dissertation submitted to the Faculty of the Graduate School of the
University of Maryland, College Park in partial fulfillment
of the requirements for the degree of
Doctor of Philosophy
2026

Advisory Committee:
Professor Ronald L. Walsworth, Chair/Advisor
Professor John Cumings, Dean's Representative
Professor Christopher Jarzynski
Professor Amir Yacoby
Professor Victor Yakovenko

© Copyright by
Shantam Ravan
2026

Dedication

To my family.

Acknowledgements

This dissertation is the product of many people's generosity, and it is a pleasure to thank them here.

First, my advisor, Ron Walsworth. Ron gave me a rare kind of latitude: the freedom to pursue the topics I found interesting, and support in everything I chose to look into. He has a gift for guiding a student toward the interesting question without taking the wheel, and for introducing and helping build the relationships that made these projects successful. Every project in this dissertation exists in part because of a door Ron opened.

I owe an equal debt to Amir Yacoby, who welcomed me into his lab at Harvard and cosupervised the work presented here. What I will remember most about Amir is his tenacity, and his belief that I would produce results even in the stretches when nothing in the lab was going well. His sharp instinct for pushing science in novel directions, and his steadfastness, helped me stay focused.

I thank Eugene Demler, who has a remarkable instinct for turning experimental data into mathematical models and an eye for identifying phenomena that most scientists would miss entirely. I thank Nikola Maksimovic, who has an excellent sense of where to push the boundaries of the field and what will help it most; I will also fondly remember our coffee chats and our conversations over drinks in the kitchen. I thank the remaining members of my committee, John Cumings, Christopher Jarzynski, and Victor Yakovenko, for their time and their service.

I met Johannes Cremer over Zoom at the height of COVID, and only met him in person six months later, once the two of us were running the magnon experiment by ourselves in Harvard's Northwest building while masking policies were still in effect. Johannes trained me when I first arrived: he taught me the ins and outs of NV physics and of building NV experimental setups, helped guide and direct the experiment, and pushed us toward exploring magnon nonlinearities. He is an excellent physicist and a natural teacher, and working with him has been a great joy.

Aaron Müller has been my doppelganger on the theory side. He led the theory effort and its simulations, and this work came to a head in large part because of him. Even when my questions reached Switzerland late into his night, he always took the time to respond and to think them through. I thank Jan Rueschkamp, who led the work of Chapter 2; I greatly enjoyed working with him during his master's and helping him understand and build on the magnon physics I had been developing over the preceding years. And I thank Katrijn Everaert, who led the work of Chapter 3. We collaborated virtually for nearly the whole project, together in person for only the few weeks she spent helping me with the experimental setup. She is a great scientist with a real passion for magnetic sensing, and many of the best ideas in the ASI project trace to her, not least through the conferences she attended and the ASI community she drew in.

I have never met a more welcoming group of people than the Yacoby group. I began my PhD at the University of Maryland, and when the opportunity came to move up to Harvard and build an NV experiment in the Northwest building, they took me in with open arms, offering support, advice, and friendship. I owe thanks to Patrick Forrester, a true friend throughout my time in the group, and Seung Hwan Lee, who was enormously helpful when I first joined. I also would like to thank the other members of the NV subgroup, who helped me navigate the intricacies of NV experiments, including Shaowen Chen, Ruolan Xue, and Daniel Fernandez. The group's social events made me feel at home even though I was far from my home institution. Though I worked

with the Walsworth group mostly remotely, I enjoyed being around them, attending group meetings virtually, and watching everyone's projects grow from a seed into a broader idea.

I thank the cleanroom staff, without whom this work would not have been possible, and the administrative staff of both the University of Maryland and Harvard physics departments.

To my housemates, Rodrigo Araiza Bravo, Jordan Sosa, Greg Cunningham, Ahmed Sherif, and Yusuf Ilker Yaman: you made Boston feel like home when I arrived knowing nobody. From nights at Shay's to Super Smash Bros. on the couch, those are memories I will cherish for the rest of my life, and I hope that as we grow our separate ways we will continue to stay connected. To my countless other friends: thanking each of you individually would make this section far too long, so please accept my gratitude as a collective.

Finally, my family. I thank my parents for being so supportive and steadfast throughout this time. And I thank my brother, who did his undergraduate degree at MIT while I was in Boston: it was a joy to watch you grow from a shy high schooler into the confident young man you are today.

Table of Contents

Dedication ii

Acknowledgements iii

Table of Contents v

List of Figures viii

List of Abbreviations xv

Introduction 1

Chapter 1: Spatially Resolving the Pre-Thermal Anatomy of a Driven Bosonic Fluid 4
- 1.1 Introduction . . . 5
- 1.2 Experimental Details . . . 7
  - 1.2.1 Sample Details . . . 7
  - 1.2.2 Sample Fabrication . . . 9
  - 1.2.3 Experimental Setup . . . 11
- 1.3 Results . . . 12
  - 1.3.1 Single Frequency Magnon Generation and Detection . . . 12
  - 1.3.2 Spatially Resolving the Nonlinear Four-Magnon Interaction Strength . . . 16
  - 1.3.3 Cascaded Parametric Instabilities . . . 20
- 1.4 Discussion . . . 25

Chapter 2: A Nanoscale Magnetic Spectrum Analyzer Based on Qubit Dressed States 28
- 2.1 Introduction . . . 29
- 2.2 Experimental Details . . . 30
  - 2.2.1 Experimental setup . . . 30
  - 2.2.2 Noise creation . . . 31
  - 2.2.3 Measurement sequence . . . 33
- 2.3 Results . . . 35
  - 2.3.1 Demonstration on a test signal . . . 35
  - 2.3.2 Measurements on a YIG thin film . . . 41
- 2.4 Discussion . . . 44

Chapter 3: Imaging Magnetization Reversal of Pinwheel Artificial Spin Ice with an Ensemble of NV Centers in Diamond 47
- 3.1 Introduction . . . 48
- 3.2 Experimental Details . . . 49
  - 3.2.1 Sample fabrication . . . 49
  - 3.2.2 Experimental Setup . . . 51

3.3 Results . . . 52
3.3.1 ASI magnetic field imaging . . . 52
3.3.2 Magnetization reversal imaging . . . 54
3.3.3 Reversal state dependent magnetic field strength . . . 56
3.4 Effect of the microwave field on ASI magnetic field reversal . . . 58
3.5 Discussion and outlook . . . 58

Conclusion **61**

Appendix A: Supplementary Information: Spatially Resolving the Pre-Thermal Anatomy of a Driven Bosonic Fluid **64**
A.1 Sample Fabrication and Experimental Setup . . . 64
A.1.1 YIG Thin Film . . . 64
A.2 NV Center Physics . . . 65
A.2.1 Coherent Dynamics: Rabi Frequency . . . 65
A.2.2 Incoherent Dynamics: T_1 Transition Probability . . . 66
A.3 Magnon Physics and NV Coupling . . . 67
A.3.1 Dispersion Relation . . . 68
A.3.2 Injection Profile . . . 69
A.3.3 Magnetic Field at the NV Center . . . 70
A.3.4 Ensemble Averaging and Momentum Filter Tensors . . . 70
A.3.5 Macroscopic Rabi Frequency . . . 72
A.3.6 1D Propagation and Population Extraction . . . 73
A.4 Height Mapping . . . 75
A.4.1 Thermal Magnon Noise and T_1 Relaxation . . . 75
A.4.2 Height Map Calculation . . . 76
A.5 Stimulated Four-Magnon Scattering Model . . . 76
A.5.1 Approximation Scheme for Driven Nonlinear Systems . . . 77
A.5.2 Bogoliubov Decomposition . . . 79
A.5.3 Perturbative Expansion . . . 79
A.5.4 Application to Two-Tone Drive . . . 80
A.5.5 Derivation of the Idler Envelope Equation . . . 81
A.5.6 Solution for Damon–Eshbach Propagation . . . 82
A.5.7 Connection to Measured Signal . . . 83
A.6 Cascaded Scattering Model . . . 84
A.6.1 Parametric Instability from Four-Magnon Scattering . . . 84
A.6.2 Coupled Mode Equations . . . 85
A.6.3 Spatial Growth Rate . . . 85
A.6.4 Selection Rules for Unstable Modes . . . 87
A.6.5 Cascade Hierarchy . . . 87
A.6.6 Mean-Field Frequency Shift and Resonance Condition . . . 88
A.6.7 Fitting the Cascade Resonances . . . 89
A.6.8 Numerical Prediction of the Resonance Map . . . 89
A.7 Power Calibration . . . 94

A.7.1 Stripline Current Calibration 94
A.7.2 Calculating the Pump and Signal Magnon Amplitudes 96

Appendix B: Supplementary Information: A Nanoscale Magnetic Spectrum Analyzer Based on Qubit Dressed States **99**
B.1 Theoretical framework 99
B.1.1 AC Stark shift and three-level dressed state picture 99
B.1.2 Qubit dressed state spectrum analyzer 103
B.1.3 Scaling for broadband noise 109
B.2 Characterization results 110
B.2.1 Spectra 110
B.2.2 Experimental parameter calibrations and systematic dependencies 111
B.3 YIG 115
B.3.1 Damon-Eshbach magnons 115
B.3.2 Characterization by NV ODMR and T_1 measurements 116
B.3.3 Fits 117

Bibliography **120**

List of Figures

1.1 NV measurement setup. **(A)** Confocal microscope setup, sample holder indicated by green rectangle. The magnet used to apply the static field can be seen above the gold sample holder printed circuit board (PCB). The YIG and diamond chips are mounted facing towards the optical table, and the optical illumination and collection paths are directed from the bottom side of this image. **(B)** PCB with the sample mounted and wire bonded to its traces. **(C)** A microscope image of wire bonds connecting the PCB to bond pads with a microwave stripline in between. **(D)** A microscope image of the stripline antenna on the YIG chip used in this experiment, with no diamond chip present. **(E)** A microscope image of just a single 20×20 μm diamond chip on the YIG. 8

1.2 **Chiplet transfer process**. **(A)** Schematic of assembled sample, stage, and NV-diamond chiplet. The process described in the text is pictured in **(B-F)**. The conical shadow in **(B-F)** is the tungsten tip used to manipulate the chips. 11

1.3 Optical setup for NV measurements. The laser is in the top left corner and the excitation beam is indicated by the green line. The collection path is indicated as a red line and the neutral light by the blue line. The orange oval is a longpass filter. . 13

1.4 Experimental setup and single-frequency magnon detection. **(A)** Schematic diagram of the experimental geometry showing the YIG thin film, diamond chip with NV centers, microwave stripline antenna, and magnetic bias field orientation. Spin waves in the YIG film are a result of the precession of individual magnetic dipoles around the equilibrium magnetization, as indicated by the dashed circle. **(B)** Optical camera image of the diamond chip placed on the surface of the YIG adjacent to the stripline antenna. The green dot indicates the laser spot of the confocal microscope, used for NV excitation, which is scanned across the diamond chip to probe magnons at different positions along the YIG film. The white arrow indicates the scan direction. **(C)** Example NV optically detected magnetic resonance (ODMR) spectrum acquired with a 20 mT bias field. There is a broad dip in NV photoluminescence (PL) around 2.05 GHz due to nonlinear magnon generation, paired with a sharp PL dip at the NV resonance frequency. **(D)** Coherent NV Rabi oscillation data taken at a series of positions on the diamond chip and hence the YIG film, as indicated by the black arrows. The stripline is driven with a single microwave frequency tone at the NV resonance and the resulting NV PL signal is fit to an oscillating sinusoid. As the chip does not sit fully flat against the YIG film, the NV/YIG separation slightly increases as one moves further from the stripline, leading to a weaker magnon-driven stray field and lower Rabi frequency (see Appendix A for technical details). 14

1.5 **(A)** (i) Pulse sequence to acquire data in (C): a standard NV ODMR sequence with a microwave signal at fixed frequency f_p and an additional driving tone at swept frequency f_s. (ii) Pulse sequence to acquire data in (D). The length of the microwave signal for both f_p and f_s is swept to drive Rabi oscillations between the NV spin states. **(B)** Schematic of the four magnon NV mixing process. The left side indicates that the consumption of two f_p magnons and the emission of f_s and f_i magnons conserves energy. If the f_i idler magnon is at the NV spin resonance, then the NV ensemble will be coherently driven. **(C)** Example measured NV ODMR spectrum along the diamond chip and hence the YIG film, as well as swept drive frequency f_s, under the application of the microwave dual-tone drive at fixed bias magnetic field (16 mT). The zero to one scale of this plot indicates normalized ODMR photoluminescence (PL) contrast (see Appendix A). Four ODMR resonances are visible in the spectrum, labeled as (i), (ii), (iii) and (iv). (i) and (iii) are NV PL dips due to the $\pm$ first order stimulated four-magnon scattering processes ($2f_p - f_s$ or $2f_s - f_p$ respectively) being resonant with the NV transition. (ii) represents a set of higher order stimulated four-magnon scattering processes ($(n+1)f_p - nf_s$) on spin resonance with the NV transition. (iv) is direct microwave field driving of the NV spin resonance (f_{NV}). White dashed line indicates the value of f_p. **(D)** NV Rabi frequency data taken as a function of position during a lateral scan of the diamond chip and hence the YIG film, along the direction of the arrow in Fig. 1.4(B). The YIG film is driven with a two-tone microwave signal, such that the idler frequency f_i is resonant with the NV ODMR transition, thereby driving Rabi oscillations (similar to those seen in Fig. 1.4(D)). These Rabi oscillations are fit to a decaying sinusoid whose frequency is extracted and plotted here. **(E)** Idler magnon mode population density $\langle n_{\boldsymbol{k}} \rangle$ as a function of position, for f_p values detuned 20–80 MHz from f_{NV} at a bias field of 16 mT. $\langle n_{\boldsymbol{k}} \rangle$ values are calculated from experimentally-determined Rabi frequencies. From top to bottom, the datasets correspond to detunings of 20, 40, 60, and 80 MHz. Solid lines are fits of the data to the coupled-mode theory (Eq. (1.2)). **(F)** Extracted four-magnon couplings g_{si}^{pp} (purple dots) from the model in Eq. (1.2) as a function of magnon wavenumber k_p for a series of bias fields from 16 mT to 20 mT and f_p values detuned similarly as in (E), compared with the T-matrix prediction (orange dashed line). 19

1.6 **(A)** Three successive stages of the cascaded magnon scattering process are illustrated. (i) A pair of pump magnons at $\boldsymbol{k}_0$, indicated by the stars in the right panel, scatters into daughter modes $\boldsymbol{k}_1$ and $\boldsymbol{k}_2$. The bow-tie-shaped contour represents the on-shell phase space available to these daughter modes. The red contours mark vanishing y-component of the group velocity and delimit the gray region in which exponential spatial growth is allowed. The strongest instability occurs near the intersection of the on-shell contour with a slow-magnon line, and the corresponding daughter mode becomes a pump for the next generation. (ii) and (iii) show the subsequent scattering stages, in which the most unstable mode from the preceding generation acts as a new pump, producing modified on-shell phase-space contours and slow-magnon lines. **(B)** Example measured NV ODMR spectrum along the diamond chip and hence the YIG film, as a function of scan position and single-tone microwave drive frequency at fixed bias magnetic field (22 mT). The zero to one scale of this plot indicates normalized ODMR photoluminescence (PL) contrast (see Appendix A). Discrete NV PL resonances (highlighted in red) are observed when cascaded four-magnon scattering populates magnons at the NV frequency. **(C)** Comparison of each identified spin transition resonance frequency (diamonds), identified from a series of measured ODMR spectra, plotted as a function of bias magnetic field at a fixed position approximately 3–5 μm from the microwave stripline antenna, overlaid with expected PL resonance frequencies (dashed lines) for each magnon cascade order calculated from the two-dimensional model (see Appendix A). We find reasonable agreement between the predicted and measured (i)-(iii) resonances up to fourth order. Blue shading indicates the regions in which the model permits parametric instability, while the dashed lines mark the frequencies of maximum calculated growth rate. **(D)** NV ODMR spectra, as a function of microwave drive current, around the magnon-scattering-induced PL resonances in (B) and (C); (i)-(iii) are measured at fixed spatial positions and bias magnetic fields (indicated by gray boxes) in (B) and (C). At each driving current, a peak finding algorithm is used to extract the central PL frequency of each resonance as a function of microwave drive current (circular markers). **(E)** Center frequencies of two sets of magnon-scattering-induced PL resonances from (C) plotted as a function of drive current through the microwave stripline antenna. Each set of points (PL resonance frequencies) represents a different bias magnetic field, as given in the legend above. Fits to our quadratic model given in Eq. (1.4) are plotted as dashed lines for each bias field. 22

2.1 Visualization of MW delivery for YIG experiment. (a) Full PCB with SMA and SMB connectors. (b) View of the 100nm thick commercial YIG film with patterned bonding pads. The 3 wire bonds per pad are clearly visible. (c) View of the 10um stripline with the diamond chiplet containing the NV ensemble sitting on top of the YIG film. 31

2.2 Visualisation of artificial noise time traces uploaded to the AWG. (a) Example of three different time traces uploaded $x_i(t)$. The fast oscillations are at f_{IF} while the envelope is given by the noise BW. (b) Averaged power spectral density (PSD) of the Fourier transformations of the sum of 100 different time traces. 33
2.3 Visualization of spin echo sequence used to determine the NV spin phase and magnitude resulting from application of the probe field. 34
2.4 Measurement of qubit dressed states using a spin echo protocol. (a) Dressed state spin echo sequence with a probe field during one arm of length τ, which acts as an effective B field on the qubit (see Appendix B.1.1). Bloch sphere representation (above) shows effect of pulse sequence on qubit spin. (b) Calculated dressed state energies (within the rotating frame) in comparison to the qubit bare states as a function of detuning, Δ, of the probe field from the bare resonance relative to the probe field Rabi rate, Ω_{probe}. The black dotted line describes the bare qubit excited state in the rotating frame, while the dashed line gives the summed energy of the bare qubit ground state and the MW probe field photon. The orange lines are the dressed states, which diverge from the bare states due to the AC Stark effect with a quadratic dependency on the probe field strength, Ω_{probe}. (c) NV spin echo measurement of the dressed state frequency shift induced by the probe field as a function of detuning Δ, and a fit of the expected $1/\Delta$ dependency for $\tau = 1500$ ns. From the fit we obtain $\Omega_{\text{probe}} = 2\pi \times (3.70 \pm 0.04)$MHz. 37
2.5 Measurement of broadband noise spectra using qubit dressed states. (a) Dressed state spin echo sequence with probe field and noisy RF signal during both arms of length τ. The noise mixes with the probe field via the quadratic dependence of the qubit AC Stark shift on the total field amplitude. This mixing effectively imprints the noise onto the probe field, producing a fluctuating effective Rabi rate that induces decoherence in the qubit's x–y plane. Sweeping the spin echo sequence filter function, which is set by the probe field frequency f_{probe}, and repeating spin echo measurements allows determination of S, the noise spectral density of the RF signal field. Bloch sphere representation (upper panel) shows effect of pulse sequence and applied fields on the qubit spin. Schematic spectrum (lower panel) illustrates relative frequency locations and bandwidths of the qubit bare resonance, swept spin echo filter function, and noise signal. (b) Noise spectral density from NV decoherence measurements for three noise spectra. Solid lines represent independent measurements obtained using a conventional spectrum analyzer. The scale of S is indicated at the top of the panel. 40
2.6 Scaling of dressed state DD RF noise measurements on experimental parameters. (a) Dependence of the experimentally determined NV spin phase variance $\langle \phi^2 \rangle$ on probe field amplitude, B_{probe}, measurement time, τ, and probe field detuning from the NV resonance, Δ. The data is well-fitted by the scalings predicted by our model of this measurement scheme (Eq. 2.8). (b) Estimate of noise floor, i.e. minimal detectable RF noise spectral density, as a function of Rabi rate Ω_{probe} and noise signal frequency f, obtained by extrapolating the noise floor in our experiment for one second of integration where the Rabi rate $\approx$ 2.5 MHz. 41

2.7 Probing the spin wave properties of YIG using dressed state DD. (a) Experimental setup consists of a gold stripline antenna that produces a MW probe field to coherently drive the electronic spins of an NV ensemble in two ways: directly and by launching magnons into the thin YIG film beneath. The NV spins are also affected by intrinsic thermal magnon MW noise produced by the YIG. (b) Dressed state spin echo sequence, for which the experimentally determined phase variance $\langle\phi^2\rangle$ of the NV sensor as a function of probe field frequency resolves both the NV bare resonance ($|0\rangle \rightarrow |-1\rangle$) and thermally populated magnons at the FMR enhanced by quadratic mixing with the coherent magnons induced by the stripline MW drive. (c) Dressed state single arm sequence reveals coherent interference between the probe field and propagating magnons in the YIG. Light blue lines in (b) and (c) are fits of $\langle\phi^2\rangle$ data to the model described in Appendix B.3.3. 45

3.1 **ASI Image** An SEM image of the pinwheel array, with island dimensions indicated. 50

3.2 **NV ensemble imaging of the ASI magnetic field.** (a) Schematic diagram of the experimental geometry showing the ASI sample, diamond microchip with NV centers, stripline antenna, as well as the permanent magnet and optical objective. The sample is mounted on an XYZ translation stage, which is used to scan over the NV diamond. (b) Detailed schematic of the measured sample. The silicon carrier wafer with the ASI and the SiO_2 buffer layer is placed directly on the stage, and the diamond chip is stacked on top. The diamond is placed such that the NV sensing layer is facing the SiO_2 buffer layer. Optical NV excitation and photoluminescence collection is performed through the top side of the diamond chip. (c) Example NV ODMR spectra measured at different positions on the NV layer. The resonance frequency is positioned at a value of $D - \gamma_{\mathrm{NV}}\left(B_{\mathrm{DC}} + B_{\mathrm{ASI}}\right)$, allowing the extraction of local ASI stray fields B_{ASI} from the spectra, with known NV zero field splitting D, gyromagnetic ratio γ_{NV}, and static field B_{DC}. 53

3.3 **Magnetization reversal images** (a) A series of magnetic field maps $B_{\mathrm{ASI}}(x, y)$ of the NV ensemble taken across the ASI region at increasing target field. Each image is labeled with the target field value in mT, beginning with 16 mT in the top left corner and increasing to 28.5 mT in the bottom right corner. A 10 μm scale bar is provided for reference. The field is ramped in the direction of the purple arrow. (b) Magnetic field maps $B_{\mathrm{ASI}}(x, y)$ of four fields (labeled in mT) are reproduced from (a), along with line cuts through the ASI region denoted by the colored lines. To the right, each line cut is plotted as a function of position (in μm) along the x-axis, with the magnetic field (in mT) plotted on the y-axis. The dashed lines indicate the expected magnetic field from mumax3. 55

3.4 **Influence of the microwave field on the magnetization reversal at fixed static field.** NV f_{res} maps of the ASI acquired during the reversal at increasing microwave drive power (top to bottom). Left column: the measured f_{res} maps. Right column: the difference between each map and the one acquired at the lowest drive power. At the two lowest powers ($P_{\mathrm{MW}} = -25$ and -20 dBm), representative of the powers used for imaging, the difference maps are featureless and the inferred switching is indistinguishable from the static-field reversal of Fig. 3.3. At the highest power ($P_{\mathrm{MW}} = -1$ dBm) the difference map reveals a visibly modified switching pattern, showing that sufficiently strong microwave driving perturbs the reversal trajectory. . 57

A.1 **Height mapping of NV-YIG separation.** (a) Momentum filter function $\tilde{\mathcal{D}}_{\boldsymbol{q}}^{\downarrow,+-}$ for $\theta_{\mathrm{NV}} = -71^\circ$ and the equilibrium magnetization angle θ_0. Due to the geometry, the dominant contributions along the propagation axis q_y arise from the density-like tensor elements. (b) Spatial map of the diamond chip showing the five measurement positions and the extracted height map of z_{NV} across the chip. The variation in z_{NV} (250–500 nm) reflects non-uniform contact between the diamond and YIG surfaces. (c) T_1 relaxation rate vs. applied magnetic field at five different positions on the diamond chip. Solid lines show fits to the thermal magnon noise model with z_{NV} as the free parameter. 77

A.2 **Mean-field frequency shifts of the cascade resonances.** Fitted parameters of the resonance condition Eq. (A.61), extracted from the power-dependent frequency shift of the cascade resonances. For each applied magnetic field H_{ext}, we plot the mean-field shift coefficient β (defined via $\omega_{\mathrm{NL}} = \beta I^2$) together with the fitted cascade order n. (a) Results for the resonance shown in Fig. 1.6(C)(i). The fitted cascade order $n = 1.51(\pm 0.91)$ is consistent with $n = 2$. (b) Results for the resonance shown in Fig. 1.6(C)(ii). The fitted cascade order $n = 2.85(\pm 0.77)$ is consistent with $n = 3$. 89

B.1 Magnitude Λ and frequency shift with respect to the detuning of the probe field. Close to resonance the magnitude decreases due to a resonant drive. The full and the simple model are fitted to the frequency shift. 103

B.2 Visualization of the convolution of a spin echo filter function $W_{\tau=4000\mathrm{ns}}(f)$ (orange) and a perfectly rectangular noise power spectral density $S_s(f)$ (green). The result is directly proportional to the probe frequency dependent phase variance $\langle\phi^2\rangle(f_{\mathrm{p}})$ (blue). 109

B.3 Dressed state spin echo and reference spin echo measurements for the probe field on and off, with application of a Lorentzian noise signal. Data is expressed in terms of the unnormalized NV ensemble spin (a) magnitude Λ and (b) phase ϕ. For the dressed state spin echo measurement, mixing of the probe field and noise signal due to the AC Stark shift leads to a clear decrease in Λ when the probe field frequency overlaps with the Lorentzian noise spectrum. No such decrease is observed for the reference measurement, as the noise signal is weak and detuned from the NV bare resonance by $\Delta = 25$ MHz. Here, the frequency zero on the x-axis is about 2.903 GHz. The MW switches induce an offset of about -0.3 rad in the NV spin phase determination, as indicated in (b). 110

B.4 Calibration of the probe field. (a) B_{probe} as a function of the voltage applied on the I and Q channels of the I-Q mixer and connected to MW2 to generate the probe field, for two values of probe field detuning Δ from the NV bare resonance. The output of the I-Q mixer saturates after the linear regime up to 0.4 V. The magnetic field is calculated from the accumulated phase. (b) NV phase variance $\langle\phi^2\rangle$ as a function of the probe I-Q voltage and hence B_{probe}, determined from dressed state spin echo measurements in the presence of the rectangular noise spectrum shown in Fig. 2.5. 111
B.5 2D map of echo-arm duration τ dependency of the NV spin phase variance $\langle\phi^2\rangle$. Defined signal and reference regions are used to normalize the data to a 1D spectral representation, as in Fig. 2.5. 113
B.6 Dependence of the NV spin phase variance $\langle\phi^2\rangle$ dependency on the probe field detuning Δ. For each value of the applied noise signal (with a rectangular spectrum), dressed state spin echo measurements are performed and the probe field frequency is swept, as is done in Fig. B.3. The spectrum of the applied noise signal is then shifted by 2.5 MHz; and the dressed state spin echo measurements, with sweeping of the probe field frequency, are repeated. The Rabi rate Ω used for the measurements is ~ 2.5 MHz, thus enabling operation in the large detuning regime, $\Omega \ll \Delta$. 114
B.7 Dispersion relation of Damon-Eshbach magnons. The frequency range of the x-axis is scaled to the relevant frequency range for NV measurements reported here. The YIG film ferromagnetic resonance (FMR) is at ≈ 2280 MHz for bias magnetic field $B_{\text{ext}} = 303$ G. 115
B.8 Characterization of effect of YIG film on NV PL behavior in presence of probe field drive by the stripline antenna. (a) Continuous NV ODMR measurement with probe field frequency iteratively swept over about 400 MHz, from the expected NV resonance to the FMR of the YIG film. The applied probe field power is -20 dBm. (b) Modified NV T_1 measurements for a timescale used in the dressed state spectrum analyzer pulse sequences (500 ns) rule out FMR-enhanced longitudinal NV spin relaxation as the origin of observed decreases in NV PL contrast and NV spin magnitude far from the NV bare resonance. Consistent results are found for three probe field powers. 117

List of Abbreviations

AC	Alternating Current
ALD	Atomic Layer Deposition
AOM	Acousto-Optic Modulator
APD	Avalanche Photodiode
ASI	Artificial Spin Ice
AWG	Arbitrary Waveform Generator
BEC	Bose–Einstein Condensate
BLS	Brillouin Light Scattering
BVM	Backward-Volume Mode
CVD	Chemical Vapor Deposition
DAQ	Data Acquisition
DC	Direct Current
DD	Dynamical Decoupling
DE	Damon–Eshbach (mode)
DMC	Diamond Microchip
ESR	Electron Spin Resonance
FMR	Ferromagnetic Resonance
GGG	Gadolinium Gallium Garnet
ICP	Inductively Coupled Plasma
LPE	Liquid Phase Epitaxy
MFM	Magnetic Force Microscopy
MOKE	Magneto-Optical Kerr Effect
MW	Microwave
NA	Numerical Aperture
NV	Nitrogen-Vacancy
ODMR	Optically Detected Magnetic Resonance
PCB	Printed Circuit Board
PEEM	Photoemission Electron Microscopy
PL	Photoluminescence
RF	Radio Frequency
RIE	Reactive Ion Etching
RWA	Rotating-Wave Approximation
SEM	Scanning Electron Microscopy
SIMS	Secondary Ion Mass Spectrometry
SPCM	Single-Photon Counting Module
SQUID	Superconducting Quantum Interference Device
TEM	Transmission Electron Microscopy
WTT	Wave Turbulence Theory
XMCD	X-ray Magnetic Circular Dichroism
YIG	Yttrium Iron Garnet

Introduction

The nitrogen-vacancy (NV) center in diamond is an atomic-scale point defect whose electronic spin can be optically initialized, coherently driven with microwave fields, and read out through its photoluminescence, which makes it a sensitive quantum sensor of its local magnetic environment [1, 2]. Because the sensing spin sits inside a chemically inert crystal, NV magnetometry delivers quantitative, calibrated field readout at nanoscale spatial resolution, from cryogenic temperatures to well above room temperature, with little back-action on the system under study. The same defect serves either as a single scanning probe, for the highest spatial resolution, or as a dense ensemble in a diamond chip that images an extended sample in a single shot. These properties have made NV magnetometry a leading tool for nanoscale magnetic sensing, used across condensed matter physics to image static magnetic order and to probe the dynamics of spins, currents, and collective excitations [3, 4]. This thesis presents three ways we use NV centers for nanoscale magnetics, summarized in the three paragraphs that follow.

The first application is the spatial imaging of nonlinear magnetic dynamics. When a magnetic system is driven far from equilibrium, nonlinear interactions redistribute energy among its collective excitations, and whether this redistribution proceeds through a smooth turbulent cascade or through discrete scattering channels is a long-standing question tied to how such systems thermalize. In Chapter 1 we use spatially resolved NV magnetometry to image the nonlinear scattering

dynamics of driven magnons in a thin film of yttrium iron garnet (YIG), a material that combines exceptionally low damping with strong magnon-magnon interactions [5, 6]. By scanning the NV sensor along the magnon propagation direction, we use distance from the excitation source as a proxy for interaction time, turning a steady-state measurement into a dynamical map. We isolate the elementary four-magnon interaction with a two-tone wave-mixing protocol and extract its strength directly from the spatial growth profile, and under strong driving we observe a spontaneous cascade of discrete, power-tunable parametric resonances whose growth is maximized where the magnon group velocity vanishes. This resolves the pre-thermal regime as a structured hierarchy of scattering channels rather than a featureless continuum, and it rests on the absolute, calibrated field readout and wide field of view of NV magnetometry [7, 8].

The second application is broadband spectroscopy of magnetic noise. The spectrum of fluctuating magnetic fields encodes the dynamics of spins, currents, and quasiparticles in a material, but NV noise spectroscopy based on dynamical decoupling is restricted to frequencies below roughly 100 MHz, set by the achievable Rabi rate. In Chapter 2 we introduce a dressed-state spectrum analyzer that extends NV noise magnetometry beyond this Rabi limit. Exposing the NV qubit to a microwave dressing field during a dynamical-decoupling sequence parametrically mixes a target signal with a strong probe field through the AC Stark shift, producing a spectrum analyzer whose center frequency is set by the probe and is continuously tunable [9]. We validate the protocol on artificial test signals, finding excellent agreement with a commercial spectrum analyzer, and then apply it to a YIG thin film to extract the thermal magnon noise spectrum and group velocity at frequencies hundreds of megahertz above the NV resonance, a range inaccessible to conventional dynamical decoupling. The method preserves the nanoscale spatial resolution of NV sensing while

substantially extending its frequency reach.

The third application is confocal imaging of patterned magnetic textures. Artificial spin ices, lithographically defined arrays of interacting nanomagnets, are model systems for geometric frustration, emergent magnetic monopoles, and collective dynamics, and studying them calls for imaging that combines quantitative field readout with sub-micron resolution over a large area [10]. In Chapter 3 we apply NV-ensemble magnetic-field imaging to artificial spin ice for the first time, placing a diamond microchip directly on the sample and mapping the stray fields of a pinwheel array as it reverses under an applied static field at room temperature. The stray-field maps resolve the full reversal, from a uniform configuration through the nucleation, growth, and coalescence of mesoscopic domains to the reversed uniform state, and repeated cycles show that the reversal is stochastic yet nucleates at the same locations. Micromagnetic simulations reproduce the measured field maps, and a control measurement confirms that the microwave sensing field does not perturb the reversal. Using a dense NV ensemble rather than a single scanning probe, we obtain vector magnetometry across a roughly 100 μm field of view at sub-micron resolution, capturing the entire array and establishing NV imaging as a quantitative, non-invasive, room-temperature probe of these systems [2, 11].

Chapter 1: Spatially Resolving the Pre-Thermal Anatomy of a Driven Bosonic Fluid

This chapter is adapted from a forthcoming publication: S. Ravan, A. Müller, J. Cremer, J. Curtis, D. Fernandez, R. Walsworth, E. Demler, and A. Yacoby, "Spatially Resolving the Pre-Thermal Anatomy of a Driven Bosonic Fluid" (in preparation).

Author contributions: I led the concept development, experimental design, sample preparation, data acquisition, validation, and supervision of all project components, with help from J. Cremer. I drafted the manuscript with A. Müller, with assistance from the other co-authors. A. Müller led the model development and simulations presented in Fig. 1.6. This work was performed under the supervision of A. Yacoby, E. Demler, and R. Walsworth.

Notation in this chapter: this chapter reproduces a standalone publication and keeps its notation, in which several symbols are reused with different meanings elsewhere in the thesis. Here $\gamma = \mu_0\gamma_e$ is the electron spin gyromagnetic ratio scaled by the vacuum permeability, whereas Chapters 2 and 3 use a bare gyromagnetic ratio (written γ_{NV} in Chapter 3) that carries no factor of μ_0. The symbol D is the YIG film thickness, and the nitrogen-vacancy zero-field splitting is written Δ; in Chapter 2 D instead denotes the magnon spectral density, and in Chapter 3 D denotes the zero-field splitting. Within this chapter α is the Gilbert damping constant, β the nonlinear frequency-

shift coefficient, and S_k the coherent stripline injection amplitude, each of which denotes a different quantity in Chapter 2.

1.1 Introduction

Relaxation of interacting many-body systems to equilibrium is one of the longest-standing fundamental problems in physics. Since Boltzmann introduced the idea of ergodicity, the general picture has been that systems relax to local equilibrium on microscopic timescales, retaining only coarse-grained memories of density and temperature, before hydrodynamic variables relax toward global equilibrium [12]. Over the years, several exceptions to this canonical scenario have been identified, including integrable systems [13] and many-body localization [14]. In these cases, strong disorder or kinematic constraints strictly prevent the system from exploring phase space, effectively halting thermalization.

In this chapter, we report the experimental observation of a distinct relaxation scenario in which dynamics proceed through a cascade of scattering processes at well-defined momenta. Many earlier works studying the redistribution of energy towards equilibrium have commonly used Wave Turbulence Theory (WTT) to model a smooth, stochastic process [15, 16]. This includes work on quark-gluon plasmas [17] and sea-state spectra [18, 19]. However, concrete examples from ultracold atomic gases and photonics have hinted that coherence flows through discrete, phase-matched channels long before it thermalizes. In Bose–Einstein condensates (BECs), periodic modulation triggers parametric instabilities that emit 'firework' patterns of excitations at well-defined momenta [20, 21], generate Faraday waves and granulation [22], and form density patterns stabilized by non-equilibrium fixed points [23, 24]. Similarly, in semiconductor microcavities, driven

exciton-polaritons scatter into specific signal and idler modes governed by strict phase-matching rules [25, 26].

We utilize magnons, the bosonic quanta of spin waves, in yttrium iron garnet (YIG) to demonstrate this novel relaxation phenomenon in a room-temperature solid-state system. YIG supports strong nonlinear interactions with exceptionally low damping [5, 6], enabling landmark observations of magnon Bose–Einstein condensation [27, 28] and thermalization [29, 30], and allowing us insight into magnon-magnon scattering dynamics. While these have been previously characterized by Brillouin light scattering [31, 32], nitrogen-vacancy (NV) diamond magnetometry [7, 8] has proven to be a powerful tool for studying magnonics, especially given its ability to measure the absolute magnetic field, with both high spatial resolution and wide field-of-view across a sample of interest.

In our work, we leverage NV magnetometry to directly image the scattering dynamics of magnons in a YIG thin film. We first isolate a single scattering process via stimulated wave mixing, extracting the four-magnon interaction strength from its spatial growth profile. We then track the spontaneous cascade of magnon scattering processes under strong driving, discovering that the system populates a hierarchy of discrete, power-tunable resonances. These are cascaded parametric modes where a coherent drive spawns successive generations of daughter magnonic waves. Standard perturbative approaches like S-theory (the mean-field theory of parametrically excited waves) [33, 34] predict the primary instability threshold but fail to capture the multi-stage kinetics preceding thermalization. We develop a new model which demonstrates that the buildup of these modes is governed by dynamic selection rules that favor $\boldsymbol{k}$-values where the group velocity vanishes, effectively isolating the instability. At these slow magnon points the magnon energy den-

sity is compressed and the four-magnon interaction amplified, in analogy to the enhancement of optical nonlinearities in slow-light media [35–37]. By correlating spatial growth with mean-field frequency shifts and modeling this process using conjugate wave optics and Bogoliubov theory, we identify these resonances as the nonlinear pathways (the stepping stones) by which the coherent fluid restructures itself before equilibration. Our results establish thin-film magnonics and NV imaging as a platform for visualizing the deterministic anatomy of thermalization in driven quantum many-body systems.

1.2 Experimental Details

1.2.1 Sample Details

We use a 4 mm $\times$ 6 mm sample chip diced from a 100 nm-thick YIG thin film grown on a 3-inch-diameter GGG substrate. The sample chip is patterned with a stripline antenna, with a width of 10 μm made from a 10 nm Ti, 300 nm Au stack, with wide pads on either end. The chip is mounted on a PCB, with both ends of the stripline antenna wirebonded to PCB traces: one side connects to the microwave drive circuit, and the other to a 50 Ω termination. The PCB is shown in Fig. 1.1b, and an example of wirebonded pads is shown in Fig. 1.1c. The circuit drives currents at selected frequencies through the stripline antenna.

On the YIG film, we place a 50 μm by 50 μm diamond chip. This chip, with thickness $\sim$1–2 μm, was commercially fabricated from a bulk single-crystal CVD diamond substrate (Element Six, natural isotopic abundance) cut along the $\langle 111 \rangle$ direction. The diamond is implanted with nitrogen ions with implantation energy of 10 keV and a dose calibrated to yield > 1000 NVs per μm^2, without extra steps to create additional vacancies and anneal the diamond [38]. The resulting

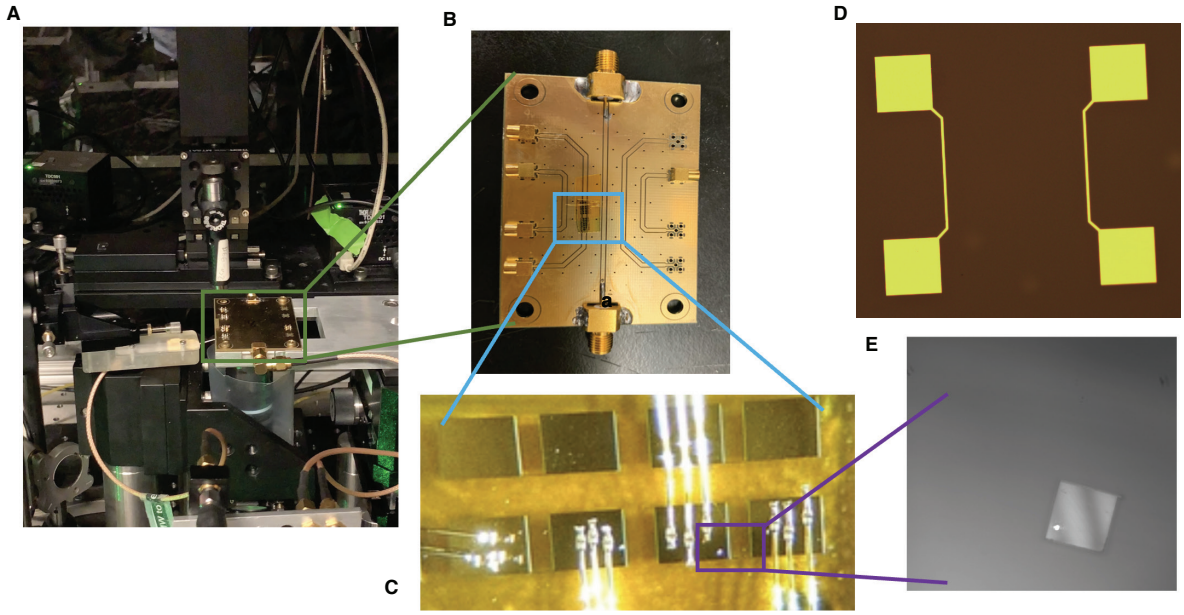


Figure 1.1: NV measurement setup. **(A)** Confocal microscope setup, sample holder indicated by green rectangle. The magnet used to apply the static field can be seen above the gold sample holder printed circuit board (PCB). The YIG and diamond chips are mounted facing towards the optical table, and the optical illumination and collection paths are directed from the bottom side of this image. **(B)** PCB with the sample mounted and wire bonded to its traces. **(C)** A microscope image of wire bonds connecting the PCB to bond pads with a microwave stripline in between. **(D)** A microscope image of the stripline antenna on the YIG chip used in this experiment, with no diamond chip present. **(E)** A microscope image of just a single 20 $\times$ 20 μm diamond chip on the YIG.

implanted nitrogen atoms are at a depth of approximately 10 nm from the diamond surface [38], with approximately 50 NVs per confocal volume along each of the four NV orientation classes within the diamond [39]. On the surface of the diamond chip with the NV centers, we deposit a 210 nm-thick layer of TiO_2 via ALD to increase the separation between the NVs and the YIG surface. We then use a pick and place technique, using a probe station and tungsten tips, to place the diamond chip on the YIG, with the NV side facing (in proximity to) the YIG surface. The diamond chip is placed approximately 3–5 μm from the antenna and is not perfectly flush with the YIG surface (see Fig. 1.4(B)). The NV/YIG separation across the diamond chip (in the direction of the white arrow in Fig. 1.4(B)) is measured using NV T_1 relaxometry measurements (see Appendix A), and is between 250–500 nm. Data is also collected on a second diamond chip to confirm the general behavior, but all data presented in this chapter and related quantitative calculations are acquired using a single chip.

1.2.2 Sample Fabrication

The stripline antenna is patterned on the YIG chip by direct-write photolithography and metal liftoff, carried out at the Harvard University Center for Nanoscale Systems. We first solvent-clean the diced YIG chip by sonication in acetone and then isopropanol (IPA), and blow it dry with nitrogen. We promote photoresist adhesion with a spin-coated hexamethyldisilazane (HMDS) primer and a 115 °C dehydration bake, then spin-coat a $\sim$1.5 μm layer of S1813 positive photoresist and softbake at 115 °C. The stripline pattern is exposed in a Heidelberg MLA-150 maskless laser lithography system and developed in MF-319 developer followed by deionized-water rinses. Before metallization we apply a brief oxygen-plasma descum (50 W, 1 min), which we find im-

proves edge definition and liftoff. We then deposit the metal stack by thermal evaporation onto the rotating chip under high vacuum (base pressure $\sim 5 \times 10^{-7}$ Torr): a 10 nm Ti adhesion layer at 0.4 Å/s, followed by 300 nm of Au at 0.5 Å/s. Finally, the remaining resist and excess metal are removed by liftoff, soaking in Remover PG at 70 °C and then sonicating in fresh Remover PG and IPA, which leaves the 10 μm-wide Ti/Au stripline antenna on the YIG surface, as pictured in Fig. 1.1d.

The TiO_2 spacer layer on the diamond chip is grown by atomic layer deposition (ALD) on a Savannah ALD system using tetrakis(dimethylamido)titanium (TDMAT) as the titanium precursor. We first transfer the diamond chip NV-side up onto a quartz carrier, then deposit the TiO_2 over the NV-bearing face at a reduced chamber temperature of 90 °C, chosen for its higher TiO_2 growth rate; 3077 deposition cycles yield the $\sim$210 nm film. The coated chip is subsequently placed NV-side down onto the YIG surface.

The chiplet transfer process is shown in Fig. 1.2. The diamond chip is placed on top of the YIG substrate with free space beneath so that any broken chips will fall from the fabricated diamond sample onto the YIG. Panels **B-C** show the breakage process under an optical microscope. A sharp tungsten probe tip is used to break a diamond chip that is 20 microns by 20 microns by gently pushing down on it using a motorized stage. Afterwards, we remove the diamond superstructure and locate the chips on the sample as shown in panel D. In panels **E-F**, we show that we use the same tungsten probe to move the fallen chips to the desired location on the YIG sample next to the microwave stripline.

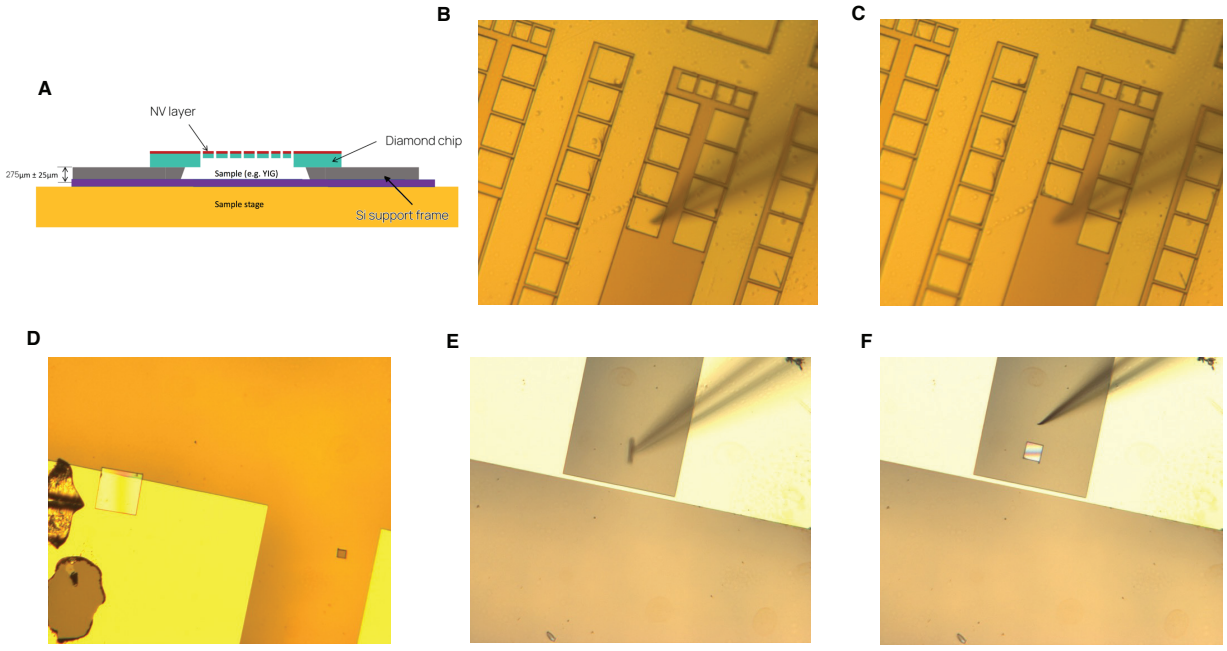


Figure 1.2: **Chiplet transfer process**. **(A)** Schematic of assembled sample, stage, and NV-diamond chiplet. The process described in the text is pictured in **(B-F)**. The conical shadow in **(B-F)** is the tungsten tip used to manipulate the chips.

1.2.3 Experimental Setup

We utilize a confocal microscope with a 0.9 NA objective and an estimated 350 nm spot size. It is equipped with a 520 nm Cobolt diode laser to initialize the NVs into the $m_s = 0$ state, and a single photon detector to measure the NV photoluminescence (PL). The diamond/YIG sample is mounted on a 3-axis Newport translation stage. The focus of the objective is fixed in space and we sweep the stage position to scan across the diamond chip. To apply the bias field, we use a permanent magnet mounted on an independent translation stage. We calibrate the position of the magnet to specify the field magnitude and to reliably align the field along one of the four NV ensemble orientation classes within the diamond [39], and we calculate the associated lab-frame directions of these classes. A photograph of these components is given in Fig. 1.1a. Due to the

$\langle 111 \rangle$ orientation of the diamond, we apply the field -71° from the surface normal.

The microwave circuit is driven by two signal generators (Agilent E4428 and Rohde & Schwarz SMA100A) and terminated with a Signal Hound spectrum analyzer, serving as the 50 Ω load. The signals are pulsed using Mini-Circuits switches. These are driven using a Tektronix AWG, which is programmed using our experimental control software. The AWG is also used to modulate the laser diode. NV PL measurements from the single photon detector are digitized using a National Instruments DAQ. The pulse sequence creation, data collection, and analysis are performed using a custom Matlab interface on our lab computer.

The optical setup for the NV measurements is shown in Fig. 1.3. The green light is produced by a 520-nanometer Cobolt laser pictured in the top left of this image. It is directed through a coupled fiber into the confocal microscope, where it then proceeds through a dichroic and is focused down by an objective lens onto the diamond chip. The collected red photoluminescence is gathered by the same objective and proceeds back through the excitation path. It is then separated by a dichroic mirror, proceeding to a pinhole element to isolate the photoluminescence from the NV layer and then directed onto a single photon detector. There is an additional flippable mirror that allows us to illuminate the sample with neutral light and capture optical images of the sample.

1.3 Results

1.3.1 Single Frequency Magnon Generation and Detection

To directly image the spatial evolution of the magnon gas, we employ a dense ensemble of nitrogen-vacancy (NV) centers in close proximity to a room-temperature, 100 nm-thick YIG thin film (Fig. 1.4(A, B)). The diamond chip (50 μm $\times$ 50 μm), that hosts the NV ensemble, is posi-

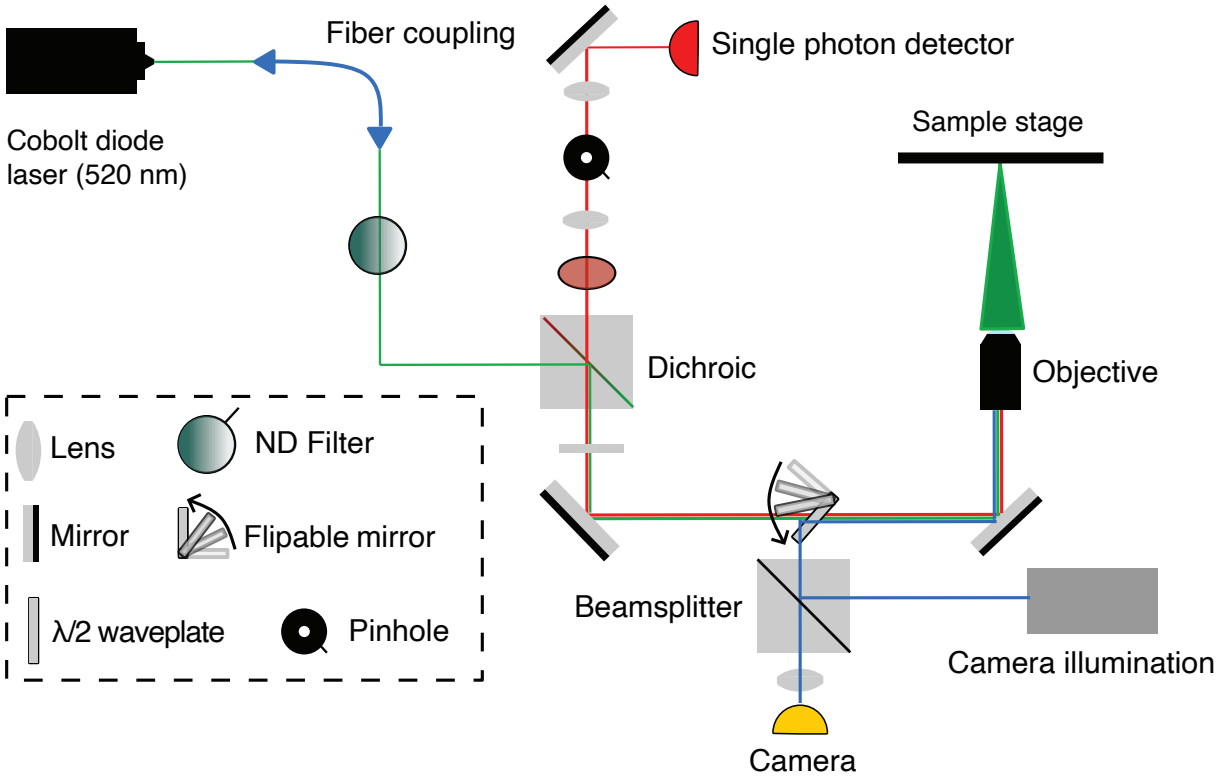


Figure 1.3: Optical setup for NV measurements. The laser is in the top left corner and the excitation beam is indicated by the green line. The collection path is indicated as a red line and the neutral light by the blue line. The orange oval is a longpass filter.

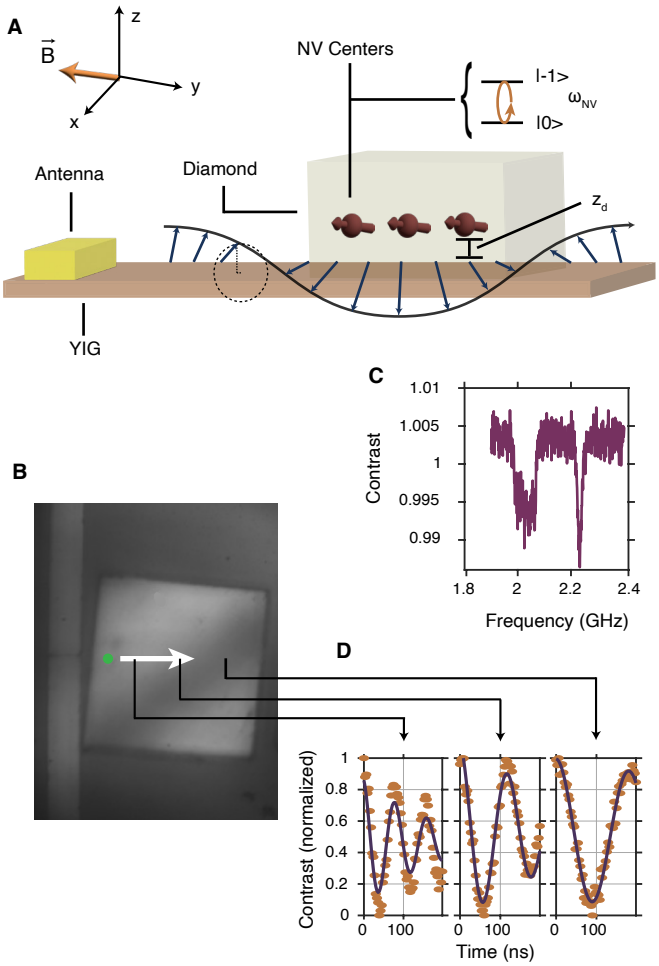


Figure 1.4: Experimental setup and single-frequency magnon detection. **(A)** Schematic diagram of the experimental geometry showing the YIG thin film, diamond chip with NV centers, microwave stripline antenna, and magnetic bias field orientation. Spin waves in the YIG film are a result of the precession of individual magnetic dipoles around the equilibrium magnetization, as indicated by the dashed circle. **(B)** Optical camera image of the diamond chip placed on the surface of the YIG adjacent to the stripline antenna. The green dot indicates the laser spot of the confocal microscope, used for NV excitation, which is scanned across the diamond chip to probe magnons at different positions along the YIG film. The white arrow indicates the scan direction. **(C)** Example NV optically detected magnetic resonance (ODMR) spectrum acquired with a 20 mT bias field. There is a broad dip in NV photoluminescence (PL) around 2.05 GHz due to nonlinear magnon generation, paired with a sharp PL dip at the NV resonance frequency. **(D)** Coherent NV Rabi oscillation data taken at a series of positions on the diamond chip and hence the YIG film, as indicated by the black arrows. The stripline is driven with a single microwave frequency tone at the NV resonance and the resulting NV PL signal is fit to an oscillating sinusoid. As the chip does not sit fully flat against the YIG film, the NV/YIG separation slightly increases as one moves further from the stripline, leading to a weaker magnon-driven stray field and lower Rabi frequency (see Appendix A for technical details).

tioned with an average distance of $z_{\mathrm{NV}} \approx 300$ nm above the YIG surface, and the NVs are probed with a custom-built setup including a confocal microscope and microwave antenna (see Sec. 1.2), ensuring non-invasive sensing of the local dipolar fields from the YIG film while maintaining sub-micron spatial resolution [39, 40]. An external magnetic bias field H_{ext} is applied at $\theta_{\mathrm{NV}} = -71^{\circ}$ relative to the surface normal, to enable probing of one orientation class of NVs within the diamond chip and to orient the magnetization for the excitation of Damon-Eshbach YIG spin waves [41].

We utilize two complementary NV sensing modalities to map the spectral and spatial magnon characteristics of the excitations. First, we employ NV optically detected magnetic resonance (ODMR) spectroscopy to identify the local magnon spectrum. As shown in Fig. 1.4(C), the ODMR spectrum with a 20 mT bias field reveals a sharp resonance at 2.2 GHz, corresponding to direct excitation of magnons at the NV resonance frequency. Crucially, we also observe a broad, anomalous magnon absorption feature centered at 2.05 GHz. As we discuss in the following sections, this signature arises not from direct magnon driving, but from the nonlinear generation of cascaded magnon scattering products.

Second, to quantify the local spin wave amplitude, we drive coherent Rabi oscillations of the NV sensor at the magnon frequency (Fig. 1.4(D)). By scanning the confocal volume of probed NVs away from the microwave antenna, we observe a spatial decay in the Rabi frequency Ω_R, which is proportional to the local microwave field amplitude $B_{\mathrm{mw}} \propto \Omega_R$. This calibration confirms our ability to spatially resolve the propagation of coherent magnon excitations over finite distances, a prerequisite for imaging the kinetic buildup of the cascade of magnon scattering processes [42].

1.3.2 Spatially Resolving the Nonlinear Four-Magnon Interaction Strength

We begin by isolating the elementary four-magnon scattering process using a stimulated wave-mixing protocol. These magnon-magnon processes, which underlie the second-order Suhl instability [43], have recently emerged as a powerful tool for studying magnon dynamics, including creating spin-wave frequency combs [44] and coherently generating target magnon modes [45]. However, these efforts largely exploit the nonlinearity as a tool, rather than explore the intricate many-body dynamics that it produces. While Brillouin light scattering experiments have directly observed these scattering processes at finite wavevectors [32,46], quantitative measurements of the microscopic interaction vertex g remain rare [33].

Here, we implement a spatially resolved scheme, using NV magnetic imaging (Fig. 1.5(A)), similar to that employed in Ref. [45]. This approach coherently generates and images a specific scattering product, allowing us to extract the magnon coupling strength for the four-magnon scattering process (see Fig. 1.5(B) for graphical definition of k_p, k_s, and k_i) directly from its spatial magnon growth profile, thereby demonstrating the first component of the cascade of magnon scattering processes.

We apply a dual-tone microwave drive to the YIG film consisting of a pump at frequency f_p and a signal f_s that acts as a seed. In the perpendicular pumping configuration (see Appendix A), the dominant nonlinearity arises from the dipole-dipole interaction, which mixes these modes to generate an idler magnon at $f_i = 2f_p - f_s$. By tuning f_p and f_s such that the resulting idler frequency f_i coincides with the NV spin transition frequency f_{NV}, we use the NV ensemble magnetometer within the confocal volume as a spectrally selective filter to image only the nonlinear scattering product, effectively blind to the pump and signal fields; see Fig. 1.5(B).

Figure 1.5(C) shows a map of the measured spectral landscape of this process. We fix the pump frequency f_p and sweep the seed f_s, measuring the NV photoluminescence (PL) as a function of distance from the antenna, using the pulse sequence in Figure 1.5(A)(i). We observe a rich structure of resonances. Beyond the expected direct driving of the NV spin transition frequency (labeled (iv) in Fig. 1.5(C)), we detect distinct magnon mixing orders, labeled as follows in Fig. 1.5(C): (i) the primary four-magnon signal at $f_i = 2f_p - f_s$; (iii) the inverse process $2f_s - f_p$; and (ii) a set of higher-order processes at $f_i = (n+1)f_p - nf_s$, where n is an integer indicating the order. The visibility of these higher orders confirms the high coherence of the nonlinear four-magnon interaction process, a prerequisite for the formation of stable pre-thermal states.

We focus on the first-order idler mode (i) to extract the four-magnon interaction strength. Since the scattering is phase-coherent, the generated idler magnons drive coherent Rabi oscillations of the NV sensor. By measuring the Rabi frequency Ω_R as a function of position y (Fig. 1.5(D)), using the pulse sequence in Fig. 1.5(A)(ii), we map the spatial envelope of nonlinear magnon generation. We convert this Rabi frequency to the local magnon population density $\langle n_{\boldsymbol{k}} \rangle$ via the relation (derived in Appendix A):

$$\langle n_{\boldsymbol{k}} \rangle = s_{\text{eff}} \left(\frac{\Omega_R}{\gamma \mathcal{C}} \right)^2 \tag{1.1}$$

where $\gamma = \mu_0 \gamma_e$ is the electron gyromagnetic ratio scaled by the vacuum permeability, $s_{\text{eff}} = M_s/(\gamma\hbar)$ is the effective spin density of the YIG film, set by the saturation magnetization $M_s = 1.55 \times 10^5$ A/m, and $\mathcal{C}$ collects the saturation magnetization together with the geometric, evanescent, and ellipticity factors.

To extract the four-magnon coupling g_{si}^{pp}, we fit the spatial growth of the idler population density to a coupled-mode theory derived from the nonlinear Schrödinger equation (see Appendix A).

Assuming the pump and seed amplitudes remain undepleted over the measurement range, the idler amplitude $A_i(y)$ evolves as:

$$A_i(y) = \frac{A_0}{\lambda_0 - \lambda_i - i\Delta k^y} \left[e^{-\lambda_i y} - e^{(-\lambda_0 + i\Delta k^y)y}\right] \tag{1.2}$$

Here, $A_0 = -ig_{si}^{pp} A_p^2 A_s^* / v_i^y$ is the nonlinear source term, v_i^y is the y-component of the idler group velocity, $\lambda_{p,s,i}$ are the spatial decay rates of the pump, seed, and idler, $\lambda_0 = 2\lambda_p + \lambda_s$ is the combined decay rate of the source, and Δk^y is the momentum mismatch ($\Delta k^y = 2k_p^y - k_s^y - k_i^y$) for the four-magnon scattering process. This model captures the competition between nonlinear gain and propagation loss, providing reasonable fits to the experimental data in magnon dynamics and spatial growth (Fig. 1.5(E)).

The extracted four-magnon interaction strengths g_{si}^{pp} from this fitting procedure are plotted in Fig. 1.5(F) (purple dots), alongside theoretical predictions from standard T-matrix theory [47] (orange dashed line). To calculate g_{si}^{pp}, we extract A_0 from the fits and determine A_p and A_s from the microwave power injected into the stripline, assuming a linear relationship between the drive current and the magnetization amplitude [8]. We attribute the discrepancy between the measured and predicted values of g_{si}^{pp} to our restriction to $k_x = 0$ in the scattering model. In practice, the large magnon populations injected at the pump and signal frequencies may also scatter into $k_x \neq 0$ modes at f_{NV}, enhancing Ω_R and hence the inferred A_0, and thereby yielding a larger extracted g_{si}^{pp} than predicted.

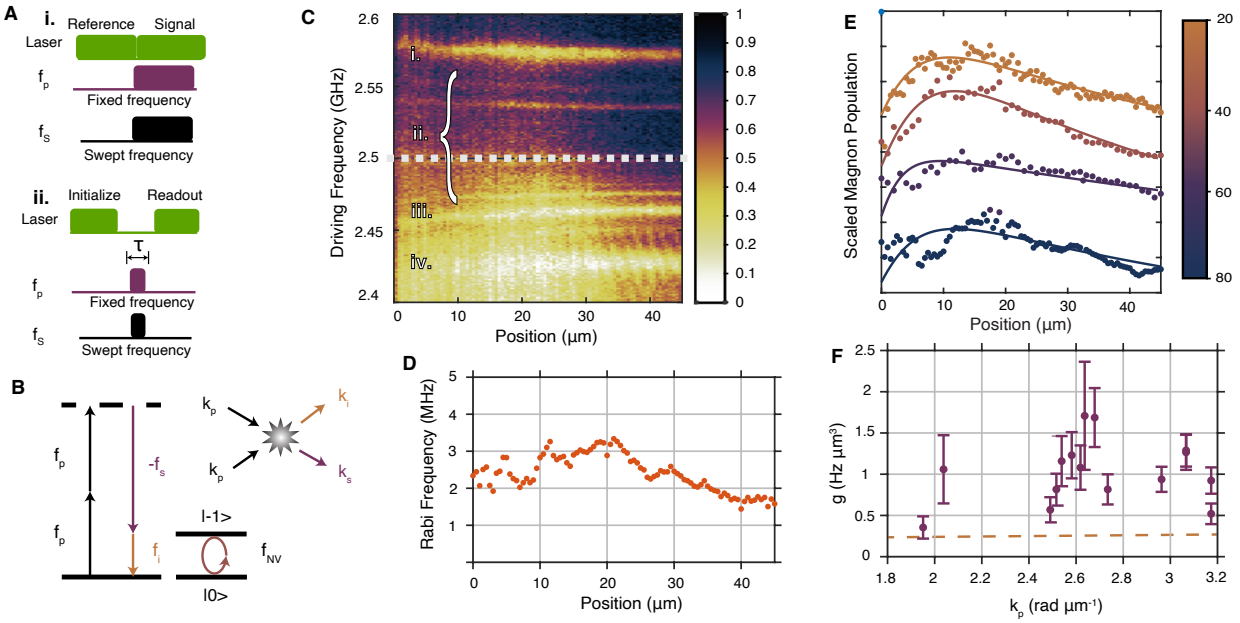


Figure 1.5: **(A)** (i) Pulse sequence to acquire data in (C): a standard NV ODMR sequence with a microwave signal at fixed frequency f_p and an additional driving tone at swept frequency f_s. (ii) Pulse sequence to acquire data in (D). The length of the microwave signal for both f_p and f_s is swept to drive Rabi oscillations between the NV spin states. **(B)** Schematic of the four magnon NV mixing process. The left side indicates that the consumption of two f_p magnons and the emission of f_s and f_i magnons conserves energy. If the f_i idler magnon is at the NV spin resonance, then the NV ensemble will be coherently driven. **(C)** Example measured NV ODMR spectrum along the diamond chip and hence the YIG film, as well as swept drive frequency f_s, under the application of the microwave dual-tone drive at fixed bias magnetic field (16 mT). The zero to one scale of this plot indicates normalized ODMR photoluminescence (PL) contrast (see Appendix A). Four ODMR resonances are visible in the spectrum, labeled as (i), (ii), (iii) and (iv). (i) and (iii) are NV PL dips due to the $\pm$ first order stimulated four-magnon scattering processes ($2f_p - f_s$ or $2f_s - f_p$ respectively) being resonant with the NV transition. (ii) represents a set of higher order stimulated four-magnon scattering processes ($(n+1)f_p - nf_s$) on spin resonance with the NV transition. (iv) is direct microwave field driving of the NV spin resonance (f_{NV}). White dashed line indicates the value of f_p. **(D)** NV Rabi frequency data taken as a function of position during a lateral scan of the diamond chip and hence the YIG film, along the direction of the arrow in Fig. 1.4(B). The YIG film is driven with a two-tone microwave signal, such that the idler frequency f_i is resonant with the NV ODMR transition, thereby driving Rabi oscillations (similar to those seen in Fig. 1.4(D)). These Rabi oscillations are fit to a decaying sinusoid whose frequency is extracted and plotted here. **(E)** Idler magnon mode population density $\langle n_{\boldsymbol{k}} \rangle$ as a function of position, for f_p values detuned 20–80 MHz from f_{NV} at a bias field of 16 mT. $\langle n_{\boldsymbol{k}} \rangle$ values are calculated from experimentally-determined Rabi frequencies. From top to bottom, the datasets correspond to detunings of 20, 40, 60, and 80 MHz. Solid lines are fits of the data to the coupled-mode theory (Eq. (1.2)). **(F)** Extracted four-magnon couplings g_{si}^{pp} (purple dots) from the model in Eq. (1.2) as a function of magnon wavenumber k_p for a series of bias fields from 16 mT to 20 mT and f_p values detuned similarly as in (E), compared with the T-matrix prediction (orange dashed line).

1.3.3 Cascaded Parametric Instabilities

Having characterized the elementary four-magnon vertex, we now turn to the regime of strong single-tone microwave driving near the ferromagnetic resonance (FMR) of the YIG film, where the system spontaneously organizes into a hierarchy of non-equilibrium states (Fig. 1.6(A)). Previous studies have hinted that high-power driving can redistribute magnon populations via three-magnon splitting [48] or four-magnon scattering [30].

We drive the system with a single frequency ω_0 near the FMR and spatially scan the NV confocal volume to map the resulting magnon concentration. The measured NV ODMR spectral response, shown in Fig. 1.6(B) for a magnetic bias field of 22 mT, reveals a striking pattern. Beyond the direct excitation of the NV spin transition at 2.27 GHz, we observe a series of discrete, magnetic-field-dependent resonances (highlighted in red). These features signify that magnons driven near the FMR are undergoing spontaneous four-magnon scattering events, generating daughter populations that are resonant with the NV sensor.

To describe this hierarchy of magnon interactions, we model the system as a cascade of parametric resonances. A pair of pump waves $(\omega_0, \mathbf{k}_0)$ scatters into a pair of daughter modes $(\omega_1, \mathbf{k}_1)$ and $(\omega_2, \mathbf{k}_2)$. Uniquely, our theoretical framework relaxes the standard on-shell assumption, and analyzes nonequilibrium dynamics in a system without translational invariance. By solving the coupled-mode equations in the steady state (see Appendix A), we derive the spatial growth rate λ for daughter modes propagating perpendicular to the microwave stripline antenna (i.e., along the

direction probed by the NV sensor, as shown by the white arrow in Fig. 1.4(B)):

$$\lambda = \pm\sqrt{\frac{|g_{12}^{00}A_0^2|^2}{v_{\boldsymbol{k}_1}^y v_{\boldsymbol{k}_2}^y} - \left(\frac{\tilde{\omega}(\boldsymbol{k}_2) + \tilde{\omega}(\boldsymbol{k}_1) - 2\omega_0}{v_{\boldsymbol{k}_1}^y + v_{\boldsymbol{k}_2}^y}\right)^2} \tag{1.3}$$

Here, g_{12}^{00} is the four-magnon interaction vertex, A_0 is the pump amplitude, $v_{\boldsymbol{k}_{1,2}}^y$ are the group velocities of the daughter modes, and $\tilde{\omega}(\mathbf{k})$ includes the mean-field frequency shifts. The structure of this equation reveals the dynamic selection mechanism of the cascade. The instability growth is maximized at the specific phase-space coordinates where the resonant manifold (the black surface satisfying the on-shell condition) intersects with the contours of vanishing group velocity ($v^y \to 0$, red lines in Fig. 1.6(A)). The gain term in Eq. (1.3) scales as $1/\sqrt{v_{\boldsymbol{k}_1}^y v_{\boldsymbol{k}_2}^y}$ and is sharply enhanced as the daughter group velocities approach zero. As modes with low group velocities experience an extended spatial overlap with the active pumping region, they accumulate a larger amplitude per unit propagation length, maximizing the parametric gain along these slow-magnon lines.

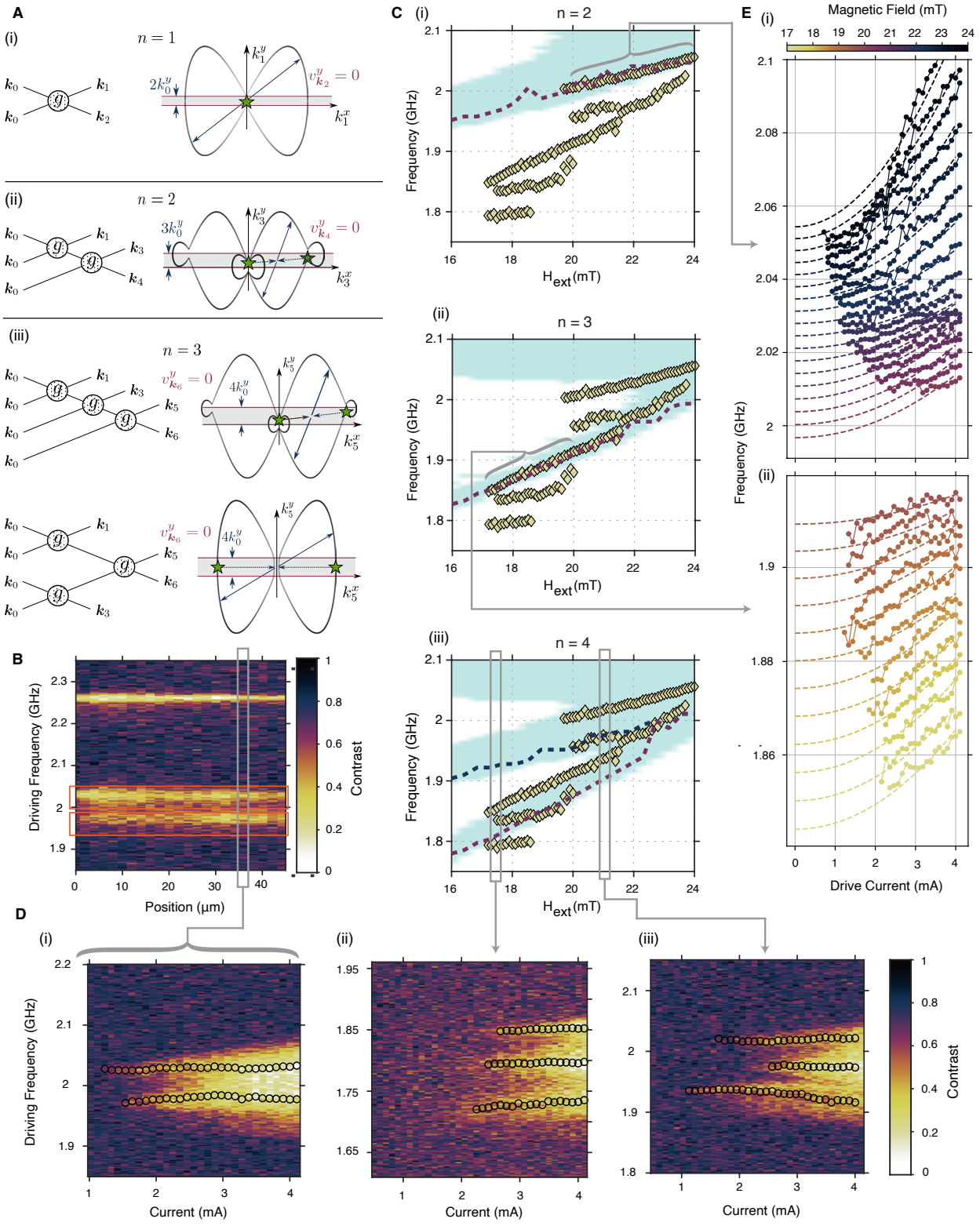

A
(i)
n = 1
(ii)
n = 2
(iii)
n = 3
B
Driving Frequency (GHz)
Position (μm)
Contrast
C
(i)
n = 2
(ii)
n = 3
(iii)
n = 4
Frequency (GHz)
H_ext (mT)
D
(i)
(ii)
(iii)
Driving Frequency (GHz)
Current (mA)
E
(i)
Magnetic Field (mT)
(ii)
Frequency (GHz)
Drive Current (mA)

Figure 1.6: **(A)** Three successive stages of the cascaded magnon scattering process are illustrated. (i) A pair of pump magnons at $\boldsymbol{k}_0$, indicated by the stars in the right panel, scatters into daughter modes $\boldsymbol{k}_1$ and $\boldsymbol{k}_2$. The bow-tie-shaped contour represents the on-shell phase space available to these daughter modes. The red contours mark vanishing y-component of the group velocity and delimit the gray region in which exponential spatial growth is allowed. The strongest instability occurs near the intersection of the on-shell contour with a slow-magnon line, and the corresponding daughter mode becomes a pump for the next generation. (ii) and (iii) show the subsequent scattering stages, in which the most unstable mode from the preceding generation acts as a new pump, producing modified on-shell phase-space contours and slow-magnon lines. **(B)** Example measured NV ODMR spectrum along the diamond chip and hence the YIG film, as a function of scan position and single-tone microwave drive frequency at fixed bias magnetic field (22 mT). The zero to one scale of this plot indicates normalized ODMR photoluminescence (PL) contrast (see Appendix A). Discrete NV PL resonances (highlighted in red) are observed when cascaded four-magnon scattering populates magnons at the NV frequency. **(C)** Comparison of each identified spin transition resonance frequency (diamonds), identified from a series of measured ODMR spectra, plotted as a function of bias magnetic field at a fixed position approximately 3–5 μm from the microwave stripline antenna, overlaid with expected PL resonance frequencies (dashed lines) for each magnon cascade order calculated from the two-dimensional model (see Appendix A). We find reasonable agreement between the predicted and measured (i)-(iii) resonances up to fourth order. Blue shading indicates the regions in which the model permits parametric instability, while the dashed lines mark the frequencies of maximum calculated growth rate. **(D)** NV ODMR spectra, as a function of microwave drive current, around the magnon-scattering-induced PL resonances in (B) and (C); (i)-(iii) are measured at fixed spatial positions and bias magnetic fields (indicated by gray boxes) in (B) and (C). At each driving current, a peak finding algorithm is used to extract the central PL frequency of each resonance as a function of microwave drive current (circular markers). **(E)** Center frequencies of two sets of magnon-scattering-induced PL resonances from (C) plotted as a function of drive current through the microwave stripline antenna. Each set of points (PL resonance frequencies) represents a different bias magnetic field, as given in the legend above. Fits to our quadratic model given in Eq. (1.4) are plotted as dashed lines for each bias field.

Once a daughter magnon population reaches a critical threshold, it acts as a secondary pump for a subsequent magnon scattering generation. This stepwise thermalization explains the discrete bands observed in our data: each NV PL dip corresponds to a specific generation (n) of the cascade. We track these resonances across a broad magnetic field range (17–24 mT, Fig. 1.6(C)), confirming their robust nature.

However, the mode with the highest theoretical growth rate is not necessarily the dominant signal in our measurement. As detailed in Appendix A, the NV sensor acts as a momentum filter,

sensitive only to modes within a finite window of k-space defined by the sensor-sample stand-off distance. While the global instability maximum often occurs at large transverse wavevectors inaccessible to our sensor, the observed NV PL signal in Fig. 1.6 arises from integrating the instability spectrum over the accessible momentum window. Consequently, off-resonant contributions, where parametric gain dominates the off-shell penalty in Eq. (1.3), contribute significantly to the integrated signal. This effect explains the robustness of the observed bands: the NV sensor captures the spectral tails of the instability, allowing for the detection of discrete scattering patterns even when the divergence peak lies outside the maximal sensitivity window.

Having established that these discrete resonances are robustly detected across a range of magnetic fields (Fig. 1.6(C)), we next examine their evolution with microwave drive power. We measure the NV PL spectrum at a fixed spatial position while sweeping the drive current (Fig. 1.6(D)), and extract the central frequency of each resonance at each power level. A signature feature revealed by this measurement is the microwave-power-dependence of the observed resonance frequencies. As shown in Fig. 1.6(E), the resonance positions shift quadratically with microwave drive current. This effect arises from the Hartree-Fock mean-field shift $\omega_{\mathrm{NL}} \propto \beta I^2$ induced by the high magnon density. As the driven magnon amplitude scales linearly with current ($A_0 \propto I$), the population-dependent mean-field shift scales quadratically ($\langle n_{\boldsymbol{k}} \rangle \propto |A_0|^2 \propto I^2$) (see Appendix A). For an n-th order cascade, the resonance condition becomes:

$$\omega_0(n, I) = \frac{\omega_{\mathrm{NV}} + (n-1)\Delta_0}{n} + \frac{2(n-1)}{n}\beta I^2 \tag{1.4}$$

where Δ_0 is the FMR gap. We fit the power-dependent resonance spectrum to this model (dashed lines in Fig. 1.6(E)), allowing us to extract the cascade order n and the effective nonlinearity

coefficient β.

Taken together, the two-dimensional resonance model and the power-dependent fits reveal distinct families of instabilities. The higher-field branch (Fig. 1.6(C)(i) and (E)(i)) is consistent with an $n \approx 2$ cascade process, while the lower-field branch (Fig. 1.6(C)(ii) and (E)(ii)) corresponds to $n \approx 3$. A third, weaker branch (Fig. 1.6(C)(iii)) is consistent with an $n \approx 4$ cascade in the two-dimensional model, demonstrating that the hierarchy extends to at least four generations of daughter magnons before the signal falls below our detection threshold. The deviation from integer values extracted from the power-dependent fits indicates that the dominant scattering channels involve modes with non-zero transverse momentum ($k_x \neq 0$). This result is physically expected, as the most unstable modes reside at finite k_x, where the system can simultaneously satisfy the vanishing group velocity condition and minimize the off-shell penalty. This mode mixing is further evidenced by the positive sign of the extracted β coefficients (see Appendix A), a feature that T-matrix theory predicts only for modes with finite k_x.

1.4 Discussion

Our results provide a spatially resolved map of the specific kinetic pathways through which a driven bosonic fluid redistributes energy away from equilibrium. By deconstructing the approach to equilibrium in a YIG thin film, we reveal that the pre-thermal regime is not a featureless, diffusive continuum, but a structured hierarchy of discrete interactions. The observation of these cascaded parametric instabilities challenges the standard continuum assumptions of Wave Turbulence Theory [15, 16]. Instead of a smooth flow of energy toward the thermal bath, we observe a cascade of parametric magnon scattering events, where energy accumulates along specific slow-magnon

contours in phase space.

This discrete anatomy implies that the pathway to equilibrium is governed by strict dynamic selection rules. We find that the driven YIG film naturally selects scattering channels that balance two competing forces: the maximization of parametric gain (favored by vanishing group velocity) and the minimization of the off-shell penalty. This behavior mirrors the "fireworks" emission in driven Bose–Einstein condensates [20, 21], suggesting a universality in how driven systems restructure themselves near kinetic bottlenecks.

These observations are enabled by the strong four-magnon nonlinearity and low intrinsic damping of YIG, which together allow the parametric gain to overcome dissipation and sustain several generations of scattering at accessible microwave drive powers. Crucially, our stimulated wave-mixing measurement provides direct, spatially resolved access to the underlying four-magnon vertex g, rather than relying on an analytically approximated coupling [47]. Anchoring the cascade model in this measured interaction is what allows us to quantitatively reproduce the observed hierarchy of resonances and to establish the dynamic selection rules as the organizing principle of the pre-thermal cascade.

Methodologically, our work establishes spatially resolved NV magnetometry as a powerful technique for "chronocounting" quasi-particle interactions. By using propagation distance as a proxy for interaction time, we transformed a steady-state measurement into a dynamical map of the scattering evolution. Unlike inductive or optical techniques that integrate over large volumes, the sub-micron resolution of the NV sensor allows us to resolve the fine structure of these instabilities and directly extract the microscopic interaction strength local to the scattering events.

Looking forward, this platform offers a controlled measurement testbed for simulating the

nonlinear kinetics of diverse physical systems. The ability to tune the interaction vertex via geometry and the cascade hierarchy via drive power opens the door to studying the crossover from discrete parametric cascades to hydrodynamic flow. Future experiments could probe the phase-space correlations of these scattering events. Because parametric amplification generates correlated magnon pairs, the daughter populations should retain distinct statistical signatures absent in a purely stochastic wave-turbulent cascade. Spatially mapping the second-order coherence function $g^{(2)}$ would directly expose these pairwise correlations, providing a definitive test of the discrete relaxation pathways. By bridging the gap between microscopic scattering rules and macroscopic fluid dynamics, thin-film magnonics provides a tangible window into the non-equilibrium evolution of quantum many-body systems.

Chapter 2: A Nanoscale Magnetic Spectrum Analyzer Based on Qubit Dressed States

This chapter is adapted from the preprint: J. Rueschkamp, S. Ravan, D. Fernandez, N. Delegan, F. J. Heremans, D. D. Awschalom, R. L. Walsworth, N. Maksimovic, and A. Yacoby, "A nanoscale magnetic spectrum analyzer based on qubit dressed states," arXiv:2606.05426 (2026).

Author contributions: I led the experimental design, sample preparation, data acquisition, validation, and analysis primarily of the YIG noise magnetometry component of this project, assisted by J. Rueschkamp and N. Maksimovic. I assisted J. Rueschkamp in drafting the manuscript, with assistance from the other co-authors. This work was performed under the supervision of A. Yacoby, N. Maksimovic, and R. Walsworth.

Notation in this chapter: here γ denotes the bare electron spin gyromagnetic ratio, following the convention of this work; unlike Chapter 1, where $\gamma = \mu_0\gamma_e$ is the gyromagnetic ratio scaled by the vacuum permeability, here γ carries no factor of μ_0. The symbol h denotes Planck's constant. Several further symbols differ from their meaning in Chapter 1: Δ is the probe detuning (probe frequency minus resonance frequency), whereas in Chapter 1 Δ is the nitrogen-vacancy zero-field splitting; α and β are noise-scaling prefactors, whereas in Chapter 1 they are the Gilbert damping and the nonlinear frequency-shift coefficient; $S(f)$ is the noise spectral density, whereas S_k in

Chapter 1 is a stripline injection amplitude; and $D(f,k)$ is the magnon spectral density, whereas D is the film thickness in Chapter 1 and the zero-field splitting in Chapter 3. The saturation magnetization M_s is quoted here in Gaussian units (1850 G), versus the SI value used in Chapter 1.

2.1 Introduction

A variety of phenomena in physics, chemistry, and quantum technology manifest as magnetic fluctuations on nanometer length scales. Examples include spin dynamics in magnets [49] and spin liquids [50, 51], electrical current dynamics in superconductors [52, 53] and hydrodynamic metals [54], spin dynamics and correlations in small-scale chemistry [55,56], and noise in quantum device hardware [57]. Fluctuation phenomena can even be used to extract entanglement properties of a many-body quantum system [58].

For the purpose of detecting these phenomena, quantum sensors based on atomic-scale color centers in semiconductors, such as the nitrogen-vacancy (NV) center in diamond, are a promising platform that sets new benchmarks in magnetic field sensitivity and spatial resolution [39]. These solid-state spin qubit sensors measure radio-frequency (RF) magnetic fields using dynamical decoupling (DD) protocols [59, 60], a technique that manipulates the spin state of the qubit by using microwave (MW) control pulses, allowing for both homodyne [61, 62] and heterodyne [56] detection of coherent signals, as well as noise spectroscopy [49]. The latter, in particular, is vital for the investigation of many physical phenomena where spectral responses are often broadband [63]. While DD noise magnetometry using spin-qubits provides an unparalleled combination of sensitivity, spatial resolution, and practicality, it is limited in frequency bandwidth and range by the

speed of the DD qubit control sequence as defined by the Rabi rate – proportional to the amplitude of the pulsed control field. In NV diamond, for example, DD noise sensing is limited to $\sim$100 MHz [64, 65]. This bandwidth/range limitation is coincidentally similar in other nanoscale RF magnetic probes like RF SQUIDs [66].

In this work, we introduce a method for spectral analysis of RF noise, based on well-established DD protocols, that extends the accessible frequency range beyond the Rabi limit by leveraging qubit dressed states [9]. We demonstrate this dressed state DD technique using small NV ensembles to detect both artificial test signals and the spin wave dynamics of a magnetic thin film of Yttrium Iron Garnet (YIG). From the resulting measured RF spectra, we characterize magnetic excitations in the YIG film under conditions that are inaccessible with other quantum sensing protocols, highlighting the value of the dressed state DD technique in practical sensing applications.

2.2 Experimental Details

2.2.1 Experimental setup

2.2.1.1 Sample

The first set of experiments involving a test signal was conducted on an NV confocal experiment built by collaborators and is not discussed here. More information can be found in the published work. For experiments on the YIG sample, we used the same experimental setup as given in Chapter 1. To reiterate, MW delivery is through a 10um gold stripline that is patterned by photolithography and connected to the PCB through wire bonds. A picture of the PCB, the diamond

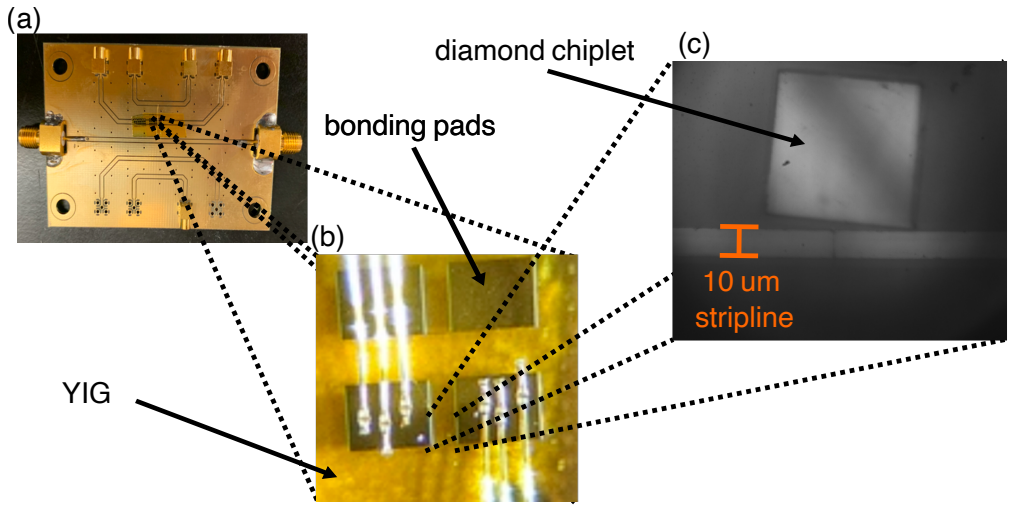


Figure 2.1: Visualization of MW delivery for YIG experiment. (a) Full PCB with SMA and SMB connectors. (b) View of the 100nm thick commercial YIG film with patterned bonding pads. The 3 wire bonds per pad are clearly visible. (c) View of the 10um stripline with the diamond chiplet containing the NV ensemble sitting on top of the YIG film.

chiplet and the YIG sample is shown in Fig. 2.1. Typical values in the chiplet are $T_1 = 0.46$ ms and $T_2 = 2.3$ μs.

2.2.2 Noise creation

To generate the RF noise signals in order to characterize the dressed state DD spectrum analyzer we use the fact that providing an RF signal at frequency f_{IF} on both the I and Q channels of an IQ mixer will create two sidebands according to:

$$\cos\left(f_{\mathrm{LO}}t\right)\cdot\cos\left(f_{\mathrm{IF}}t\right) \tag{2.1}$$

$$=\tfrac{1}{2}\left[\cos\left(\left(f_{\mathrm{LO}}-f_{\mathrm{IF}}\right)t\right)+\cos\left(\left(f_{\mathrm{LO}}+f_{\mathrm{IF}}\right)t\right)\right] \tag{2.2}$$

where f_{LO} is in our case the on resonant drive frequency of the NV spin transition. We use this simple technique, with IF signals generated by the AWG, to create arbitrary signal spectra.

To generate the broadband (rectangular) noise as seen in Fig. 2.5, we upload time traces to the AWG that follow Eq. 2.3. Each trace is a superposition of many randomly phased cosine tones whose frequencies are uniformly distributed within a rectangular band around a chosen center frequency f_{noise}. Uploading multiple traces (~ 100) and looping over them creates a band-limited, approximately white noise signal centered at our frequency of choice. See Fig. 2.2 for an illustration.

The i-th noise time-trace is given by:

$$x_i(t) = A_{\text{noise}} \frac{\sum_{k=1}^{K} \cos\big(2\pi f_k t + \phi_k\big)}{\max_t \left| \sum_{k=1}^{K} \cos\big(2\pi f_k t + \phi_k\big) \right|}, \tag{2.3}$$

where

$$f_k \sim \mathcal{U}(f_{\text{noise}} - \tfrac{\text{BW}}{2},\ f_{\text{noise}} + \tfrac{\text{BW}}{2}),$$

$$\phi_k \sim \mathcal{U}(0, 2\pi),$$

A_{noise} is the peak amplitude,

K is the number of microtones (typically 512),

BW is the total bandwidth,

f_{noise} is the center frequency of the noise band.

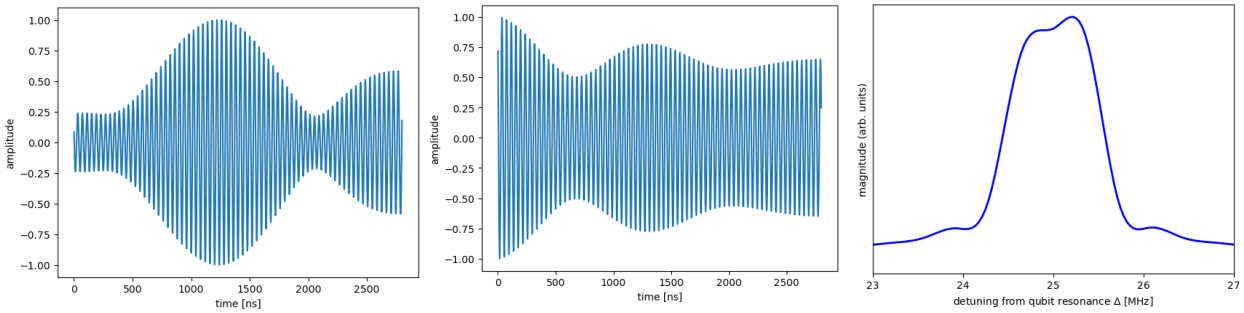


Figure 2.2: Visualisation of artificial noise time traces uploaded to the AWG. (a) Example of three different time traces uploaded $x_i(t)$. The fast oscillations are at f_{IF} while the envelope is given by the noise BW. (b) Averaged power spectral density (PSD) of the Fourier transformations of the sum of 100 different time traces.

2.2.3 Measurement sequence

Initialization of NV centers to $m_s = 0$ is done by applying a laser pulse of 2.1 μs length. We drive the NV electronic spin with MW pulses of frequency $f_{0\to+1}$ equal to the splitting between the $|0\rangle$ and $|+1\rangle$ spin states. Applying a pulse with $f_{0\to+1}$ for one quarter of the Rabi cycle duration rotates the NV spin from the state $|0\rangle$ to a coherent superposition, e.g., $|0\rangle + |+1\rangle/\sqrt{2}$. Typical Rabi rates of the setup are 2 MHz.

Fig.2.3 shows details of the dressed state spin echo sequence used to acquire the experimental results shown in Fig. 2.4. After NV spin state initialization via a green laser (A), a $\frac{\pi}{2}$ MW pulse prepares the NV spin into a coherent superposition in the transverse plane of the Bloch sphere (B). The probe field at frequency f_{probe} is then applied for time τ, inducing acquisition of phase ϕ (C). The full NV phase acquired, including the magnetic environment, is therefore $\phi + \phi_{\text{env}}$. The spin is then flipped $180°$ by a π MW pulse (D) and is left unperturbed for the same duration τ (E). This echo procedure cancels phase accumulation due to static magnetic fields from the environment, leaving a net accumulated phase of just ϕ. Note that by applying the probe field during the second half of the echo sequence, we also cancel the effect of the AC Stark shift on the NV phase as the

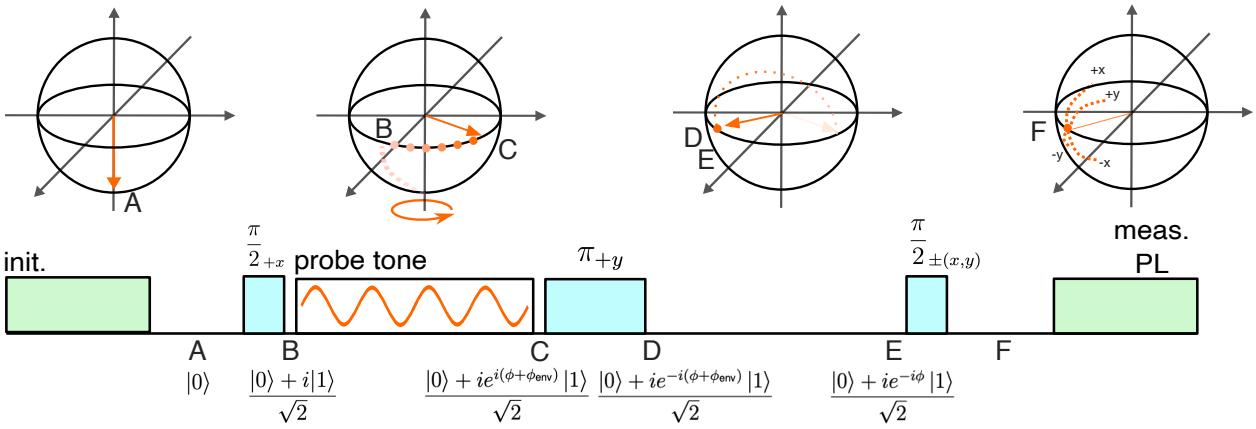


Figure 2.3: Visualization of spin echo sequence used to determine the NV spin phase and magnitude resulting from application of the probe field.

AC Stark shift acts as an effective, static magnetic field. As a final step, another $\frac{\pi}{2}$ MW pulse is applied and the NV spin projection onto the longitudinal (z) axis of the Bloch sphere is read out via NV PL induced by a green laser pulse. By iterating the rotation axis of the final $\frac{\pi}{2}$ MW pulse to be (+x, -x, +y, -y) through repeated runs of the experiment, we can reconstruct the NV spin's position on the Bloch sphere prior to the final MW pulse (F). Defining $S_{\text{rot. axis}}$ as the PL measured after a rotation around the respective axis, we introduce the tomography signals $\delta_{x/y} = S_{+x/y} - S_{-x/y}$. From these quantities, the NV spin magnitude Λ and accumulated phase ϕ prior to the final MW pulse follow as:

$$\Lambda = \sqrt{\delta_x^2 + \delta_y^2}, \qquad \phi = \arctan\left(\frac{\delta_y}{\delta_x}\right). \tag{2.4}$$

2.3 Results

2.3.1 Demonstration on a test signal

Our technique relies on parametrically mixing a weak RF noise signal with a strong MW probe field. This mixing is enabled by the quadratic scaling of the AC Stark effect on the total AC magnetic field amplitude. This quadratic dependence gives rise to a measurable cross term – a term proportional to the product of the signal and probe field. Embedding this mixing within a DD protocol allows us to amplify and measure a target noise signal at arbitrary frequency. Note that the technique presented here complements recent work using quantum frequency mixing to extend the frequency range of high-spectral-resolution NV sensing of coherent RF signals [9, 67].

Before introducing the signal of interest, we first establish the origin of this nonlinearity, which arises from the AC Stark shift: an off-resonant MW probe field at frequency f_{probe} hybridizes the qubit eigenstates into dressed states whose energy splitting is shifted relative to the bare splitting by an amount set by the probe field strength and detuning [68]. We measure the AC Stark shift using a standard spin echo DD sequence (Fig. 2.4(a)), applying the probe field during one arm of the echo. The resulting energy shift acts as an effective static magnetic field along the qubit quantization axis, causing the qubit to accumulate a phase on the Bloch sphere equator, which we read out via quantum state tomography (see section 2.2.3).

We define the detuning $\Delta = f_{\text{probe}} - f_{\text{res}}$, where f_{res} is the bare resonance frequency of the qubit in the absence of any applied MW drive fields, and the probe field strength is $\Omega_{\text{probe}} = \gamma B_{\text{probe}}/\sqrt{2}$, where γ is the gyromagnetic ratio, and B_{probe} is the probe field amplitude.

In a frame rotating at f_{res}, the dressed states (see Appendix B.1.1) have energies:

$$E_{\pm} = \pm\frac{h}{2}\sqrt{\Delta^2 + \Omega_{\text{probe}}^2} \approx \pm\frac{h}{2}(\Delta + \frac{\Omega_{\text{probe}}^2}{2\Delta}), \tag{2.5}$$

where the last step assumes operation in the high detuning regime $\Delta \gg \Omega_{\text{probe}}$. The energy shift relative to the bare splitting is $\delta E = (E_+ - E_-) - h\Delta = h\frac{\Omega_{\text{probe}}^2}{2\Delta}$, which scales quadratically with the Rabi rate, i.e., with the probe field amplitude (Fig. 2.4(b)). The qubit phase accumulated during an echo arm of length τ is:

$$\phi = \frac{1}{h}\int_0^{\tau} dt\, \delta E = -\frac{\Omega_{\text{probe}}^2}{2\Delta}\tau. \tag{2.6}$$

We implement this protocol experimentally using a room-temperature diamond pillar containing a small nanoscale ensemble of NV centers that is subject to a 0.3 mT external magnetic field along the pillar axis to split the $|-1\rangle$ and $|+1\rangle$ electronic spin transitions in the NV ground state manifold. MW signals are delivered via a wire bond near the pillar. The measurement qubit is encoded in the $|0\rangle$ and $|+1\rangle$ states and optically initialized and read out using standard NV techniques [39, 69].

Fig. 2.4(c) shows the measured dressed state frequency shift $\delta f = \frac{\phi}{2\pi\tau}$ as a function of the probe/resonance detuning; applying a $1/\Delta$ fit to the data using Eq. 2.6, we extract $\Omega_{\text{probe}} = 2\pi \times (3.70 \pm 0.04)$ MHz.

If the spin qubit is also subject to a noisy RF signal, the total Rabi rate becomes $\Omega_{\text{eff}} = \Omega_{\text{probe}} + \Omega_{\text{signal}}$. Because the AC Stark shift depends on Ω_{eff}^2 (Eq. 2.5), expanding the square produces the terms Ω_{probe}^2 and Ω_{signal}^2, as well as a cross term $\propto \Omega_{\text{probe}} \cdot \Omega_{\text{signal}}$. Intuitively, the cross term can be used as a parametric mixer because its amplitude scales with the probe field strength [9]. Since the

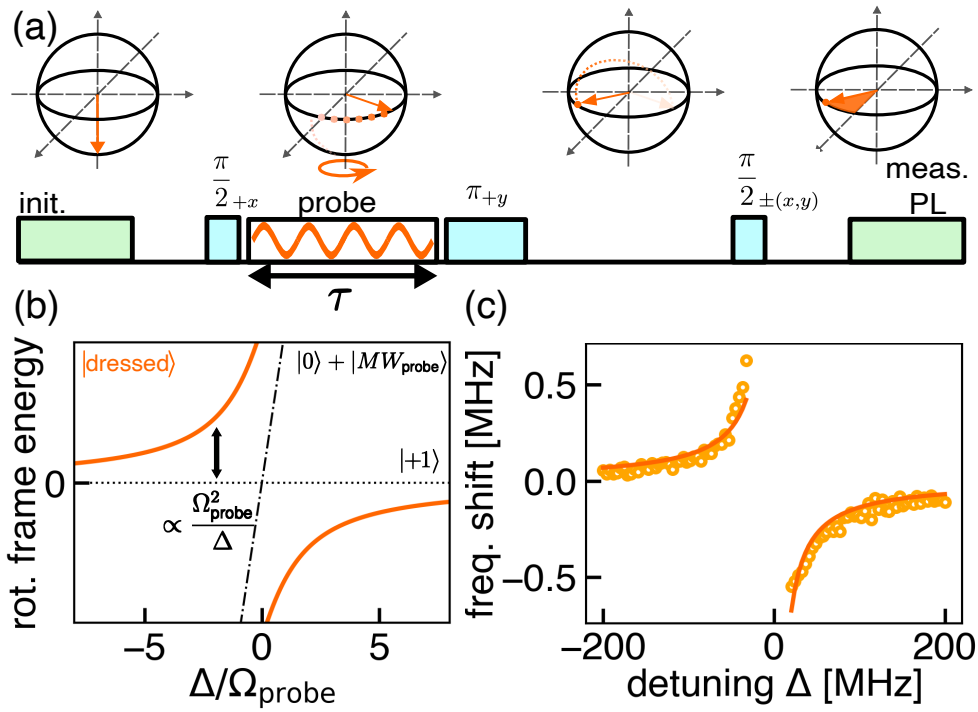


Figure 2.4: Measurement of qubit dressed states using a spin echo protocol. (a) Dressed state spin echo sequence with a probe field during one arm of length τ, which acts as an effective B field on the qubit (see Appendix B.1.1). Bloch sphere representation (above) shows effect of pulse sequence on qubit spin. (b) Calculated dressed state energies (within the rotating frame) in comparison to the qubit bare states as a function of detuning, Δ, of the probe field from the bare resonance relative to the probe field Rabi rate, Ω_{probe}. The black dotted line describes the bare qubit excited state in the rotating frame, while the dashed line gives the summed energy of the bare qubit ground state and the MW probe field photon. The orange lines are the dressed states, which diverge from the bare states due to the AC Stark effect with a quadratic dependency on the probe field strength, Ω_{probe}. (c) NV spin echo measurement of the dressed state frequency shift induced by the probe field as a function of detuning Δ, and a fit of the expected $1/\Delta$ dependency for $\tau = 1500$ ns. From the fit we obtain $\Omega_{\text{probe}} = 2\pi \times (3.70 \pm 0.04)$MHz.

noisy signal field is weak and far off resonance, the Ω^2_{signal} term is negligible (see Appendix B.1.2).

Because the noisy signal field is broadband, embedding the probe field in both arms of a DD sequence (Fig. 2.5a) selects a specific spectral component of the cross term. Moreover, the phase-evolution symmetry of this dressed state DD sequence cancels the deterministic AC Stark shift term $\propto \Omega^2_{\text{probe}}$. Computing the resulting qubit phase variance $\langle\phi^2\rangle$ (see Appendix B.1.2) yields:

$$\begin{aligned}\langle\phi^2\rangle(f_{\text{probe}}) &= 2\frac{\Omega^2_{\text{probe}}}{\Delta^2}\int_{-\infty}^{\infty} df\, \mathcal{S}(f) W_\tau(f - f_{\text{probe}}) \\ &= 2\frac{\Omega^2_{\text{probe}}}{\Delta^2}(\mathcal{S} * W_\tau)(f_{\text{probe}}) \end{aligned} \tag{2.7}$$

where $\mathcal{S}$ is the noise spectral density of the signal field and W_τ is the filter function of the spin sequence, centered at the probe field frequency f_{probe} and with bandwidth $\approx 1/\tau$. The operation $*$ denotes a convolution. Intuitively, the dressed state DD sequence provides a tunable RF noise detector and amplifier, where f_{probe} scans the filter across the RF noise spectrum, and the probe field amplifies the target noise signal (Fig. 2.5a, lower panel).

We determine the phase variance via the NV spin coherence magnitude Λ, given by the total photoluminescence (PL) contrast of the NV spin at the end of repeated spin echo measurements with a fixed evolution time (see section 2.2.3) [70]. Normalization is given by a probe-free reference measurement, Λ_{ref}, to remove the effect of intrinsic decoherence: $\langle\phi^2\rangle(f_{\text{probe}}) = -\frac{1}{2}\ln\left(\frac{\Lambda(f_{\text{probe}})}{\Lambda_{\text{ref}}}\right)$. When $\mathcal{S}$ is much broader than W_τ,

$$\langle\phi^2\rangle(f_{\text{probe}}) = \mathcal{S}(f_{\text{probe}})\, 2\tau \left(\frac{2\gamma B_{\text{probe}}}{\Delta}\right)^2. \tag{2.8}$$

As a proof of principle experiment using the small NV ensemble in the diamond pillar,

we apply the measurement sequence in Fig. 2.5a to probe broadband noise spectra centered at ~ 2.9 GHz that are generated as described in section 2.2.2; this frequency regime is inaccessible to conventional NV DD measurement protocols due to the limited Rabi rate for driving NV electronic spins [67]. Fig. 2.5(b) compares the NV data for three classes of broadband noise spectra with independent measurements from a commercial spectrum analyzer, showing excellent agreement.

For fixed signal noise spectral density, S, Eq. 2.8 predicts that $\langle\phi^2\rangle$ scales with B^2_{probe}, τ, and $1/\Delta^2$, all of which are borne out in the experimental data (Fig. 2.6(a)). The small deviation in linear τ dependence for $\tau < 700$ ns can be attributed to the fact that the noise bandwidth approaches the bandwidth of the spin echo measurement (see Appendix B.2.2).

Crucially, the actual measured decoherence depends on the probe field strength, which can be increased arbitrarily to amplify a target noise signal. The measurement here is done at $\Omega_{\text{probe}} \sim 2.5$ MHz. In practice, NV Rabi rates ~ 100 MHz are experimentally attainable [64, 65], enabling the detection of noisy RF signals across a wide frequency range. Quantitatively, we define the noise floor η through the uncertainty of a data point in Fig. 2.5(b) normalized to one second of integration time, $\eta \equiv \delta\mathcal{S}(f_{\text{res}} + 26.5\text{ MHz}) = 5900\ (\text{nT})^2/\text{Hz}$. Extrapolating this noise floor to higher probe field strengths using Eq. 2.8 reveals that noise signals of $100\ (\mu\text{T})^2/\text{Hz}$ over many GHz in frequency could feasibly be amplified to a detectable threshold (Fig. 2.6(b)). The non-linearity of the scaling below 2 GHz is due to the counter rotating component of the AC Stark shift that is otherwise dropped in the rotating wave approximation (see Appendix B.1.1).

Fig. 2.6(b) further compares the noise floor of our dressed state DD to that of conventional DD noise magnetometry under comparable conditions. Conventional DD noise magnetometry is analyzed via the following relationship between $\langle\phi^2\rangle$ and the noise floor η. In the limit of target

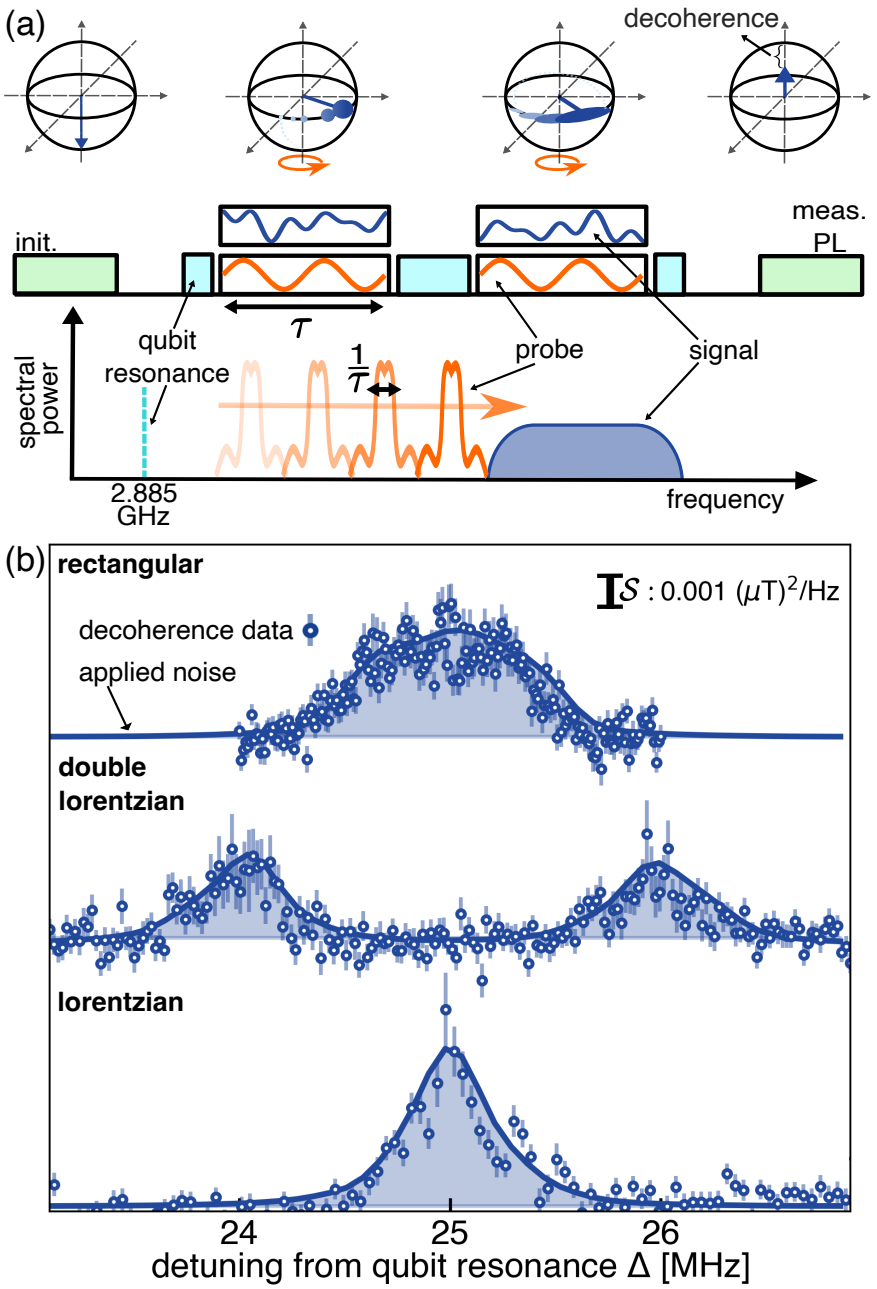


Figure 2.5: Measurement of broadband noise spectra using qubit dressed states. (a) Dressed state spin echo sequence with probe field and noisy RF signal during both arms of length τ. The noise mixes with the probe field via the quadratic dependence of the qubit AC Stark shift on the total field amplitude. This mixing effectively imprints the noise onto the probe field, producing a fluctuating effective Rabi rate that induces decoherence in the qubit's x–y plane. Sweeping the spin echo sequence filter function, which is set by the probe field frequency f_{probe}, and repeating spin echo measurements allows determination of S, the noise spectral density of the RF signal field. Bloch sphere representation (upper panel) shows effect of pulse sequence and applied fields on the qubit spin. Schematic spectrum (lower panel) illustrates relative frequency locations and bandwidths of the qubit bare resonance, swept spin echo filter function, and noise signal. (b) Noise spectral density from NV decoherence measurements for three noise spectra. Solid lines represent independent measurements obtained using a conventional spectrum analyzer. The scale of S is indicated at the top of the panel.

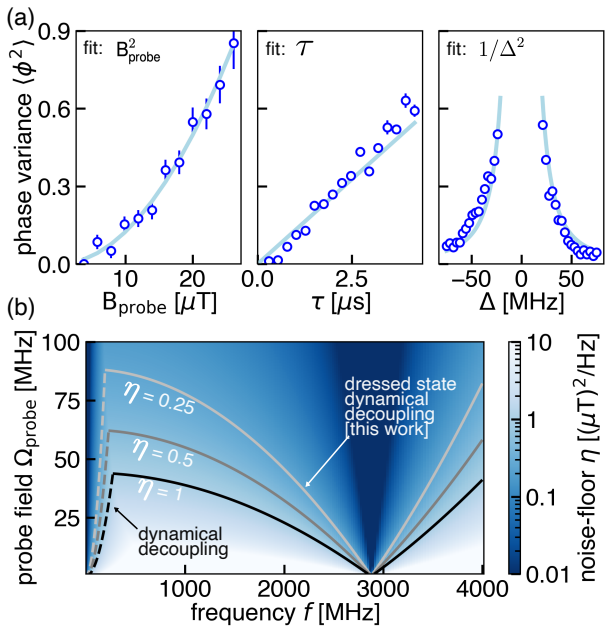


Figure 2.6: Scaling of dressed state DD RF noise measurements on experimental parameters. (a) Dependence of the experimentally determined NV spin phase variance $\langle\phi^2\rangle$ on probe field amplitude, B_{probe}, measurement time, τ, and probe field detuning from the NV resonance, Δ. The data is well-fitted by the scalings predicted by our model of this measurement scheme (Eq. 2.8). (b) Estimate of noise floor, i.e. minimal detectable RF noise spectral density, as a function of Rabi rate Ω_{probe} and noise signal frequency f, obtained by extrapolating the noise floor in our experiment for one second of integration where the Rabi rate ≈ 2.5 MHz.

noisy signal frequency much greater than DD sensing frequency, the decoherence signal in DD is given by $\langle\phi^2\rangle = \gamma^2 W_\tau(f) * \tau_{\text{eff}} * \eta$, where $W_\tau(f) \sim 1/f^2$, and the effective evolution time, τ_{eff}, is the total evolution time minus the time spent on π-pulses ($\sim 1/\Omega_{\text{Rabi}}$). In Fig. 2.6(b), the Rabi rate in conventional DD is set equal to the probe field strength in dressed state DD for the purpose of comparing the two protocols.

2.3.2 Measurements on a YIG thin film

We next apply the dressed state DD protocol to NV centers in proximity to a thin film of yttrium iron garnet (YIG), extracting both the magnon noise spectrum and the group velocity by sweeping the probe field frequency and making repeated spin echo measurements, as with the

RF noise signal demonstration described above. These experiments are performed with a room temperature apparatus (see Fig. 2.1 for details).

A 50 μm $\times$ 50 μm diamond chiplet containing a dense ensemble of NV centers is positioned approximately 300 nm above a 100 nm thick YIG thin film. A $\sim$10 μm wide gold stripline patterned on the YIG surface both applies the probe field to the NV centers and excites spin waves in the YIG (Fig. 2.7(a)). A static external magnetic field along the NV axis is tuned such that the YIG ferromagnetic resonance (FMR) lies approximately 300 MHz above the NV $|0\rangle \rightarrow |-1\rangle$ transition used in this experiment (see Appendix B.3.2), ensuring that the qubit frequency is below the magnon gap. We highlight that this configuration is inaccessible to conventional NV DD noise magnetometry due to limitations on the Rabi rate.

In this experiment, the effective NV Rabi rate Ω_{eff} has three contributions: the direct stripline drive Ω_{direct}, coherent magnons launched into the YIG Ω_{magnon}, and the intrinsic thermal magnon noise Ω_{signal}. As before, the AC Stark shift of the NV qubit depends on Ω_{eff}^2:

$$\Omega_{\text{eff}}^2 = \Big(\Omega_{\text{direct}}(f) + \Omega_{\text{magnon}}(f) + \Omega_{\text{signal}}(f)\Big)^2. \tag{2.9}$$

The choice of filter function W_τ in Eq. 2.7 determines which term contributes to the phase variance.

We perform a dressed state spin echo measurement with τ = 500 ns and the probe field (i.e., direct drive field) applied during both arms of the pulse sequence (Fig. 2.7(b)), sweeping f_{probe} from the NV resonance to 2.6 GHz and determining $\langle\phi^2\rangle$ at each frequency from NV decoherence measurements, as described in the previous section.

At $f_{\text{probe}} \approx 2.02$ GHz, a sharp peak in $\langle\phi^2\rangle$ appears from direct drive of the NV resonance due to the fact that the probe field, a Rabi drive when on resonance, has a random phase across

repeated spin echo measurements. $\langle\phi^2\rangle$ then remains zero within measurement uncertainty until f_{probe} reaches the YIG FMR near 2.3 GHz, where a second peak in $\langle\phi^2\rangle$ is observed. This signal originates from dressed state mixing of the probe field and the magnon response in the YIG film. An NV T_1 measurement with the probe field applied confirms that this peak does not originate from nonlinearities in the YIG response (see Appendix B.3.2).

To understand these features, we expand the square in Eq. 2.9 and drop Ω^2_{signal} as before. Two types of contributions remain: a coherent part $\Omega^2_{\text{coherent}} \propto (\Omega_{\text{direct}} + \Omega_{\text{magnon}})^2$ resulting from the direct drive (i.e., probe field) and the induced YIG magnons; and a cross term $\Omega^2_{\text{mix}} \propto \Omega_{\text{signal}} \cdot (\Omega_{\text{direct}} + \Omega_{\text{magnon}})$ that mixes thermal magnon noise with the coherently enhanced probe field.

As with the test signal experiment described previously, the symmetric spin echo protocol cancels the deterministic coherent contribution, leaving only the cross term. The experimentally determined NV spin phase variance in the YIG experiment is therefore related to the noise spectral density $\mathcal{S}$ via a modified version of Eq. 2.7 in which the effective probe field amplitude is enhanced by the coherent magnon response: $B^{\text{eff}}_{\text{probe}} \propto \Omega_{\text{direct}} + \Omega_{\text{magnon}}$. We model the thermal magnon noise spectral density, $\mathcal{S}$, as a k-integral over the Rayleigh-Jeans distribution, the magnon spectral density, and an effective filter in momentum space due to the finite separation between the NV ensemble and the YIG (see Appendix B.3.3) [30]. Fitting of this model to the experimentally determined NV phase variance (light blue line in Fig. 2.7(b)) yields an NV-sample distance $d \approx 450$ nm, which is comparable to the anticipated distance of about 300 nm (see Appendix B.3.3).

We next perform a measurement of the NV spin dephasing with the probe field (i.e., direct drive field) applied only during the first arm of the spin echo sequence with length $\tau = 500$ ns (Fig. 2.7(c)). We observe a peak in phase variance $\langle\phi^2\rangle$ near the NV $|0\rangle \rightarrow |-1\rangle$ transition

at 2.02 GHz; a gapped region where $\langle\phi^2\rangle$ remains zero within measurement uncertainty; and a steep rise in $\langle\phi^2\rangle$ when f_{probe} exceeds 2.3 GHz, after which oscillatory features appear in $\langle\phi^2\rangle$ as a function of f_{probe}.

These oscillatory features can be understood as arising from the coherent contribution $\Omega^2_{\text{coherent}}$, which creates a static AC Stark shift that is cancelled in the symmetric spin echo measurement, but remains in the single arm measurement, with significant effect likely due to inhomogeneous broadening of the NV spin resonance within the confocal volume. Ω_{coherent} contains a sum of two terms: the direct magnetic field experienced by the NV center from the stripline, and the magnetic field stemming from magnons launched in the YIG film [42]. The rectangular stripline launches magnons with a wavelength-dependent efficiency described by a sinc-shaped filter function in k-space [42], which imprints a periodic structure onto $\Omega^2_{\text{coherent}}$ as a function of probe frequency (see Appendix B.3.2).

Assuming a linear magnon dispersion, the $\langle\phi^2\rangle$ data can be fit to our model (see Appendix B.3.3), with results shown by the light blue line in Fig. 2.7(c). The periodicity of oscillations in the frequency spectrum can be converted to a magnon group velocity via the stripline width, yielding $v_{\text{magnon}} \approx 1450$ m/s, a value comparable to other literature results [8]. The suppressed first oscillation in the $\langle\phi^2\rangle$ data relative to this model could be a result of a smearing of the magnon gap and reduced inhomogeneous broadening at low k.

2.4 Discussion

This work demonstrates that the dressed state AC Stark shift can be used to extend the frequency bandwidth of qubit noise magnetometry well beyond the Rabi rate limit of conventional

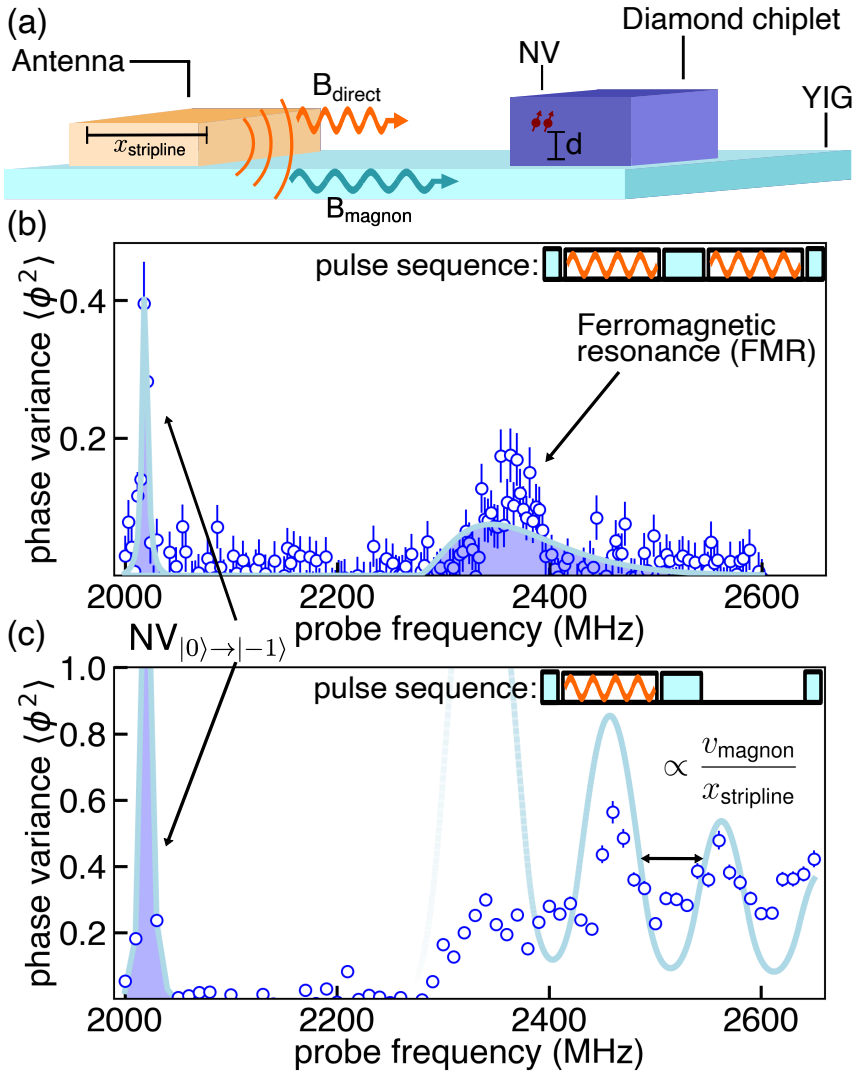


Figure 2.7: Probing the spin wave properties of YIG using dressed state DD. (a) Experimental setup consists of a gold stripline antenna that produces a MW probe field to coherently drive the electronic spins of an NV ensemble in two ways: directly and by launching magnons into the thin YIG film beneath. The NV spins are also affected by intrinsic thermal magnon MW noise produced by the YIG. (b) Dressed state spin echo sequence, for which the experimentally determined phase variance $\langle\phi^2\rangle$ of the NV sensor as a function of probe field frequency resolves both the NV bare resonance ($|0\rangle \rightarrow |-1\rangle$) and thermally populated magnons at the FMR enhanced by quadratic mixing with the coherent magnons induced by the stripline MW drive. (c) Dressed state single arm sequence reveals coherent interference between the probe field and propagating magnons in the YIG. Light blue lines in (b) and (c) are fits of $\langle\phi^2\rangle$ data to the model described in Appendix B.3.3.

dynamical decoupling (DD) measurement protocols. The quadratic dressed state mixing induced by a coherent probe tone and a noisy RF signal field, embedded in a symmetric DD sequence that cancels the probe-induced background, turns the qubit into a continuously tunable spectrum analyzer with center frequency set by the probe field. No change in magnetic field or hardware is required — only the probe frequency is swept to realize a sensitive, broadband qubit-based spectrum analyzer with nanoscale spatial resolution.

The sensitivity of the dressed state DD protocol scales as $(\Omega_{\text{probe}}/\Delta)^2$ in the large detuning limit $\Delta \gg \Omega_{\text{probe}}$, where Δ is the detuning of the probe field from the qubit bare resonance and Ω_{probe} is the probe field Rabi rate. The measurement bandwidth (i.e., largest Δ that can be probed with reasonable sensitivity) is therefore set by the probe tone strength. For NV centers, Rabi rates up to ~ 100 MHz are experimentally attainable [64, 65], implying a feasible spectrum analyzer bandwidth of several GHz. For example, in our dressed state DD measurements of a YIG film, we leveraged coherent magnons to amplify a thermal magnon signal hundreds of MHz away from the bare NV resonance. In principle, MW resonators could be used to apply directed MW probe fields to the NV sensor without disturbing the sensing volume.

More broadly, the dressed state DD protocol is naturally compatible with extensions to DD spectroscopy such as correlation spectroscopy [56], entanglement-enhanced sensing [71, 72], and quantum-computing-enhanced protocols [73]. The protocol is also platform-agnostic: any qubit with an AC Stark shift — including superconducting qubits and trapped ions — could implement this technique.

Chapter 3: Imaging Magnetization Reversal of Pinwheel Artificial Spin Ice with an Ensemble of NV Centers in Diamond

This chapter is adapted from a forthcoming publication: K. Everaert, S. Ravan, N. Reed, J. Cremer, A. Yacoby, and R. L. Walsworth, "Imaging magnetization reversal of pinwheel Artificial Spin Ice with an ensemble of NV centers in diamond" (in preparation).

Author contributions: I, along with K. Everaert, led the experimental design, and J. Cremer, K. Everaert, and I worked on the experimental setup. I developed the fabrication recipe and performed the sample preparation, and I assisted K. Everaert in the data collection and analysis. K. Everaert performed the simulations and both of us drafted the manuscript. This work was performed under the supervision of R. Walsworth and A. Yacoby. N. Reed performed analysis that is not discussed in this chapter but appears in the published work.

Notation in this chapter: here D denotes the nitrogen-vacancy zero-field splitting (≈ 2.87 GHz); the same symbol denotes the YIG film thickness in Chapter 1 and the magnon spectral density in Chapter 2, and the zero-field splitting itself is written Δ in Chapter 1. The gyromagnetic ratio is written $\gamma_{\mathrm{NV}} \approx 2\pi \times 28$ GHz/T, distinct from the symbol γ used in Chapters 1 and 2.

3.1 Introduction

Artificial spin ices (ASIs) are lithographically defined arrays of interacting single-domain nanomagnets, engineered to expose collective magnetic phenomena that range from frustration and emergent magnetic monopoles to slow ordering, ergodicity-breaking dynamics, and applications in information storage and neuromorphic computing [10, 74, 75]. Realizing this potential rests on the ability to visualize and quantify the magnetic configurations of an ASI directly, so that emergent behavior can be observed where it occurs in real space, across many islands, and as the system evolves.

Recent imaging experiments have begun to resolve thermodynamic phase transitions in tuned kagome geometries [76], and have shown that even when macroscopic hysteresis is fully reproducible, the microscopic switching trajectory is stochastic, with island-to-island correlations governed by the ratio of dipolar coupling to switching-field disorder [77]. Phenomena of this kind play out simultaneously across length scales spanning a single nanomagnet to the full array, and across timescales from individual reversal events to slow collective relaxation. Capturing them calls for an imaging modality with quantitative magnetic-field readout, fast acquisition, and a large field of view.

Previously, ASI magnetic configurations have been imaged across complementary techniques, including Lorentz transmission electron microscopy [78], and x-ray photoemission electron microscopy [79]. In parallel, magnetometry based on nitrogen-vacancy (NV) centers in diamond has emerged as a quantitative probe of magnetism across a broad range of condensed-matter systems [2, 80], offering nanoscale spatial resolution, sensitivity from cryogenic to ambient condi-

tions, and direct, calibrated readout of the magnetic field. NV centers are atomic-scale defects with an electronic spin-triplet ground state that can be optically initialized and read out; their spin resonance frequencies shift in response to local magnetic fields via the Zeeman effect, enabling sensing of static, dynamic, and narrowband signals. This combination has recently been brought to bear on ASI, with scanning single-NV magnetometry delivering spatial stray field maps in planar [81] and three-dimensional [82] ASI geometries. By using dense NV ensembles instead, sensitivity is enhanced through ensemble averaging, vector magnetometry is provided via the four crystallographic NV axes, and image fields range across $\sim$100 μm-scale areas with sub-micron resolution [11]: a much larger field of view, faster acquisition, and direct access to many islands at once compared to scanning single-NV magnetometry.

Here, we apply NV-ensemble magnetic-field imaging to artificial spin ice for the first time, mapping the local magnetic fields of superferromagnetic domains in a pinwheel ASI array as they reverse from one uniform configuration to the opposite direction under an applied static field at room temperature. We also verify that the oscillating microwave field used for sensing does not perturb the reversal at the powers used for imaging (Section 3.4).

3.2 Experimental Details

3.2.1 Sample fabrication

We fabricated the pinwheel ASI array on a diced silicon wafer by electron-beam lithography and liftoff. The wafer was solvent-cleaned by sonication in acetone and isopropanol (IPA) and given an oxygen plasma etch (150 W, 5 min). We spun a bilayer resist of 495K and 950K poly(methyl methacrylate) (PMMA) at 4000 rpm, the lower-molecular-weight bottom layer form-

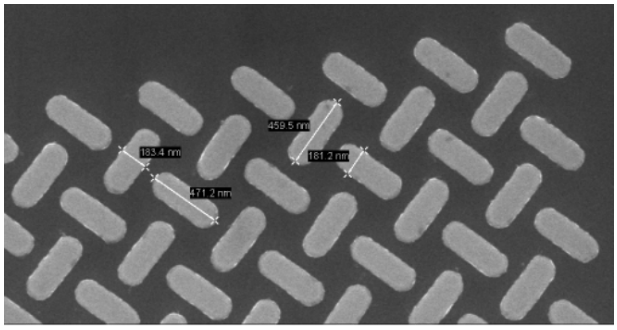


Figure 3.1: **ASI Image** An SEM image of the pinwheel array, with island dimensions indicated.

ing an undercut for clean liftoff; exposed the array by electron-beam lithography at a dose of $\sim$1000 μC/cm^2; and developed it in a chilled 3:1 IPA:water mixture. We then deposited 10 nm of permalloy capped with 3 nm of aluminium by electron-beam evaporation at 0.5 Å/s, rotating the sample during deposition to average the evaporation angle of the two-metal stack and keep the island footprint uniform, and lifted off in heated acetone (65 °C) with extended sonication. The completed array comprises 33×33 pinwheel islands of nominal in-plane size 480×180 nm following the geometry of Ref. [78], spanning $\sim 19 \times 19$ μm^2; atomic-force microscopy gives an island height of $\sim$13 nm, consistent with the deposited stack (Fig. 3.1). Separately, on the same wafer, we patterned the gold omega-loop stripline that delivers the microwave drive (inner diameter 700 μm, width 100 μm, 300 nm thickness) by direct-write laser lithography and liftoff. The stripline was fabricated before the buffer layer: with both structures complete, we deposited a 470 nm SiO_2 layer over the sample by chemical vapor deposition (CVD), spacing the array and stripline from the diamond sensor.

3.2.2 Experimental Setup

All measurements are performed at room temperature under ambient conditions with a home-built confocal microscope. Excitation light from a 532 nm laser is passed through an acousto-optic modulator (AOM) and an optical fiber, and focused onto the NV ensemble in a diamond microchip (described in Section 3.3.1) through a $100\times$, 0.9 NA air objective that also collects the spin-dependent photoluminescence (PL). The collection path is separated from the excitation by a dichroic mirror, spatially filtered through a confocal pinhole, and recorded on an avalanche photodiode (Thorlabs APD410A) behind a home-built 1.1 MHz low-pass filter. We address NV centers of a single crystallographic orientation within an excitation spot of $\sim$500 nm diameter.

Microwaves for the ODMR readout are synthesized by a signal generator (Stanford Research Systems) at -20 dBm, amplified by a Mini-Circuits ZHL-16W-43-S+, gated by an RF switch under the control of a pulse generator (SpinCore PulseBlaster), and delivered to the omega-loop stripline. The static bias field B_{DC} is provided by a cylindrical N52 permanent magnet (K&J Magnetics) on an independent three-axis translation stage (Thorlabs MTS25-Z8); we position the magnet to set the field magnitude and align it along one NV orientation class, at 19.5° to the ASI plane and 8° to the ASI array edge.

We build up spatially resolved magnetic field maps by raster-scanning the sample beneath the fixed optical focus with a piezoelectric stage (Physik Instrumente; coarse M-686.D64, fine P-54.2DD) and recording a continuous-wave ODMR spectrum at each pixel. At each pixel we fit the NV resonance frequency f_{res}, and use it to calculate the magnetic field from the ASI along the NV axis B_{ASI}. The magnetization reversal is driven by stepping B_{DC} between successive maps with the magnet stage.

3.3 Results

3.3.1 ASI magnetic field imaging

We apply NV-ensemble magnetic-field imaging to the 33×33 pinwheel ASI array as described above (Fig. 3.2). Magnetization reversal is driven by a static in-plane field B_{DC} generated by a cylindrical permanent magnet mounted on a translation stage. B_{DC} is aligned with the crystallographic axis of one NV orientation class, at 19.5° to the ASI plane and 8° to the array edge. All measurements are performed at room temperature under ambient laboratory conditions.

We probe the local magnetic field at the ASI surface using a 50×50 μm^2 diamond microchip (DMC) with a thickness of 2 μm. The DMC hosts an ensemble of NV centers at a depth of approximately 10 nm from its surface [83] and is placed directly on the sample. A 470 nm SiO_2 buffer layer separates the DMC from the ASI, allowing individual resonances within the NV ensemble to be resolved. Using a confocal scanning microscope, we optically address an ensemble of NV centers belonging to a single crystallographic orientation within an excitation region of approximately 500 nm diameter. We acquire the average optically detected magnetic resonance (ODMR) spectrum of the NV ensemble within the excitation region by sweeping the frequency of a microwave magnetic field delivered through a gold stripline, while recording the spin-dependent photoluminescence. The stripline is patterned as an omega loop beneath the buffer layer, such that the microwave field driving the NV spins is oriented normal to the ASI plane.

The local ASI stray field projected onto the probed NV axis, B_{ASI}, is extracted from the

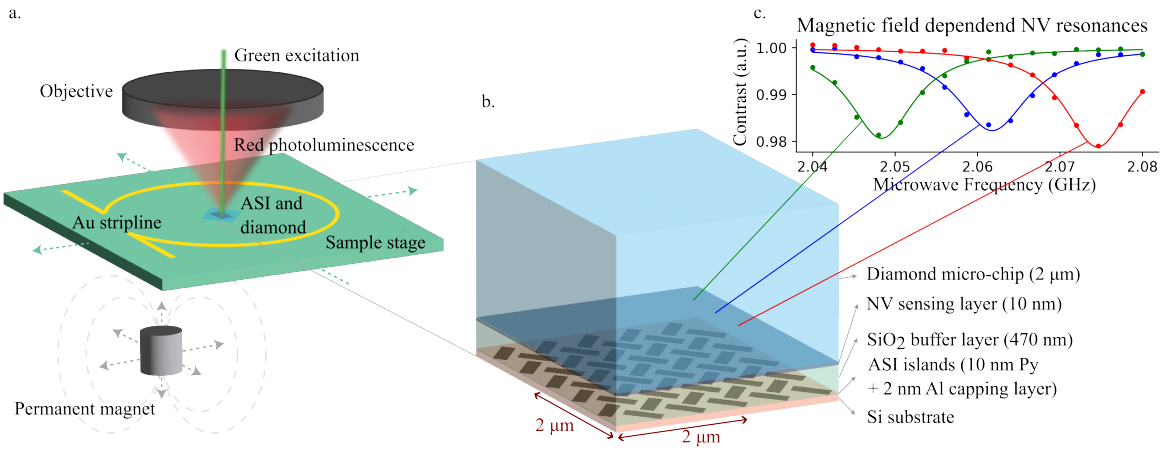


Figure 3.2: **NV ensemble imaging of the ASI magnetic field.** (a) Schematic diagram of the experimental geometry showing the ASI sample, diamond microchip with NV centers, stripline antenna, as well as the permanent magnet and optical objective. The sample is mounted on an XYZ translation stage, which is used to scan over the NV diamond. (b) Detailed schematic of the measured sample. The silicon carrier wafer with the ASI and the SiO_2 buffer layer is placed directly on the stage, and the diamond chip is stacked on top. The diamond is placed such that the NV sensing layer is facing the SiO_2 buffer layer. Optical NV excitation and photoluminescence collection is performed through the top side of the diamond chip. (c) Example NV ODMR spectra measured at different positions on the NV layer. The resonance frequency is positioned at a value of $D - \gamma_{\mathrm{NV}} (B_{\mathrm{DC}} + B_{\mathrm{ASI}})$, allowing the extraction of local ASI stray fields B_{ASI} from the spectra, with known NV zero field splitting D, gyromagnetic ratio γ_{NV}, and static field B_{DC}.

measured resonance frequency f_{res} in the ODMR spectrum according to

$$f_{\mathrm{res}} = D - \gamma_{\mathrm{NV}} (B_{\mathrm{DC}} + B_{\mathrm{ASI}}) , \tag{3.1}$$

where $D \approx 2.87$ GHz is the NV zero-field splitting and $\gamma_{\mathrm{NV}} \approx 2\pi \cdot 28$ GHz/T is the gyromagnetic ratio of the NV electronic spin. Spatially resolved magnetic-field maps are obtained by raster-scanning the optical excitation relative to the sample with a piezoelectric stage, thereby mapping the static ASI stray field at the NV layer.

3.3.2 Magnetization reversal imaging

To drive the magnetization reversal, the ASI is first fully magnetized with a strong in-plane field B_{DC} in the direction opposite the purple arrow in Fig. 3.3. We then reduce it to zero and subsequently increase it in the opposite direction (aligned with the purple arrow in Fig. 3.3) in a series of discrete steps. At each value of B_{DC}, we image the resonance spectra of the NVs in the confocal spot at each point of the raster scan and convert them into a local magnetic field value B_{ASI} following Eq. 3.1, producing a magnetic field map over the full ASI region. Magnetic field maps of the magnetization reversal for every B_{DC} value are presented in Fig. 3.3a.

The image in the top left of Fig. 3.3a shows the resonance shift map taken when the ramped field is equal to 16 mT. The ASI exhibits nearly uniform magnetization opposite to the applied static bias field, as indicated by sudden jumps in B_{ASI} at the border of the ASI region. These jumps are due to the sudden spatial change in the local stray field encountered at the edge of a fully magnetized sample. As the magnetic field continues to increase, islands in the ASI begin to switch, forming domains in the superstructure. This is seen in the subsequent images, where defects appear within the ASI structure. Each domain produces its own stray field, which we read out as a change in B_{ASI} of the NVs in that measurement. As we continue to ramp the field, these domains grow in size and eventually coalesce, as seen in the second and third rows of Fig. 3.3a. Finally, at a field of 28.5 mT, the magnetization becomes uniform again, now aligned with the external field B_{DC}.

The reversal process is stochastic, but with deterministic seeds [77], and repeating this reversal cycle multiple times produces similar trajectories. We attribute this to experimental variations in the fabrication of the sample; small variations in island height, inter-island spacing, crystal purity

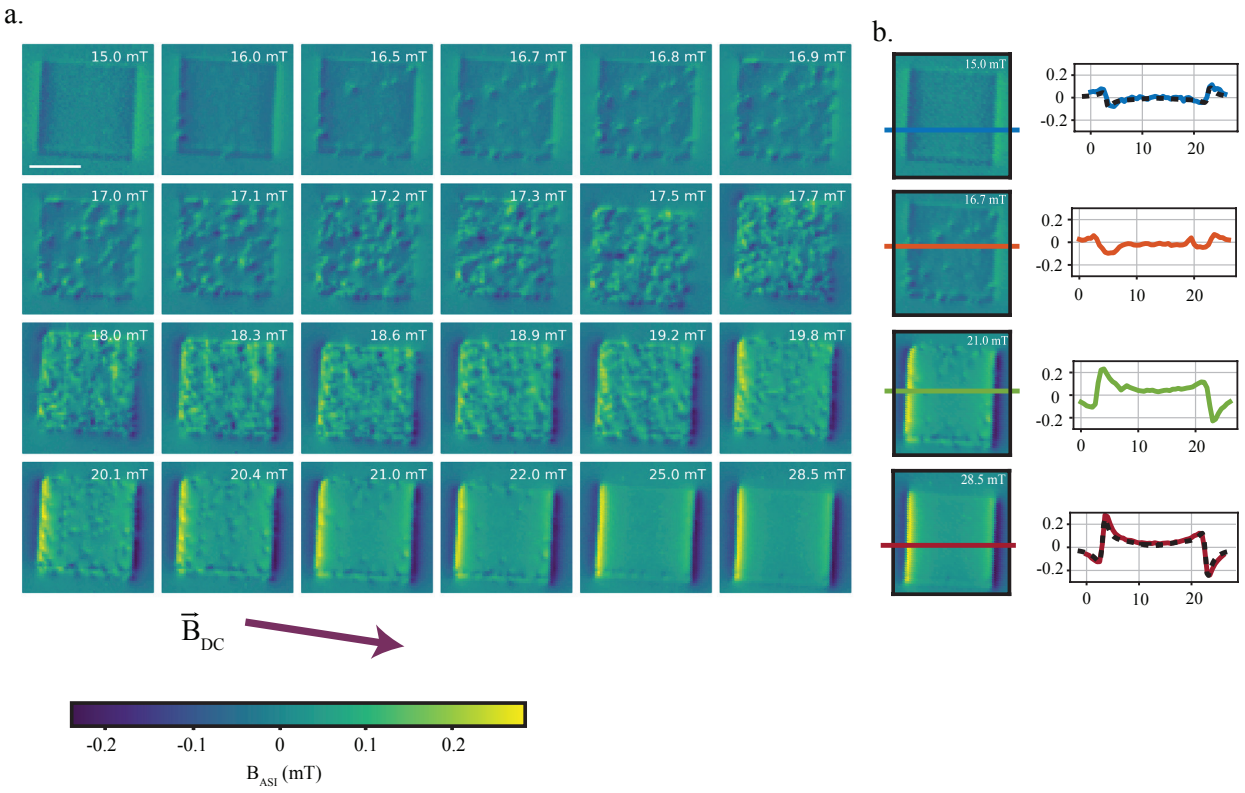


Figure 3.3: **Magnetization reversal images** (a) A series of magnetic field maps $B_{\mathrm{ASI}}(x, y)$ of the NV ensemble taken across the ASI region at increasing target field. Each image is labeled with the target field value in mT, beginning with 16 mT in the top left corner and increasing to 28.5 mT in the bottom right corner. A 10 μm scale bar is provided for reference. The field is ramped in the direction of the purple arrow. (b) Magnetic field maps $B_{\mathrm{ASI}}(x, y)$ of four fields (labeled in mT) are reproduced from (a), along with line cuts through the ASI region denoted by the colored lines. To the right, each line cut is plotted as a function of position (in μm) along the x-axis, with the magnetic field (in mT) plotted on the y-axis. The dashed lines indicate the expected magnetic field from mumax3.

and surface effects result in varying strengths of inter-island coupling, leading to certain regions with smaller switching fields than others [84].

3.3.3 Reversal state dependent magnetic field strength

From Fig. 3.3, the magnitude of B_{ASI} at the array boundaries in the post-reversal state is larger than in the initial pre-reversal state. This is due to more uniform intra-island magnetization after the reversal cycle than after the initial saturation alone. To verify our results, we simulate the reversal in our structure using mumax3 [85], modeling the array as a uniformly magnetized flat slab (whose stray field admits a closed-form solution [86]) rather than resolving the full ASI superlattice. In the top panel of Fig. 3.3b, we compare the measured shift in f_{res} with the simulated shift at 15 mT, before the magnetization reversal has occurred. We extract a line cut close to the center of the ASI region in both the measured and simulated data and overlay them in a plot to the right of the experimental magnetic image, finding excellent agreement. The vertical offset between the NV sensing layer and the ASI surface is 560 nm and is taken into account when extracting f_{res} from the simulation. We repeat this procedure in the bottom panel of Fig. 3.3b at 28.5 mT, after the reversal: the agreement demonstrates that the enhanced stray field we measure originates from the more uniform magnetization within the ASI islands after the reversal cycle. We also extract line cuts at two intermediate stages, at 16.7 mT, where only a few domains have formed, and at 21 mT, where the majority of islands have switched, demonstrating quantitative stray-field measurement throughout the reversal.

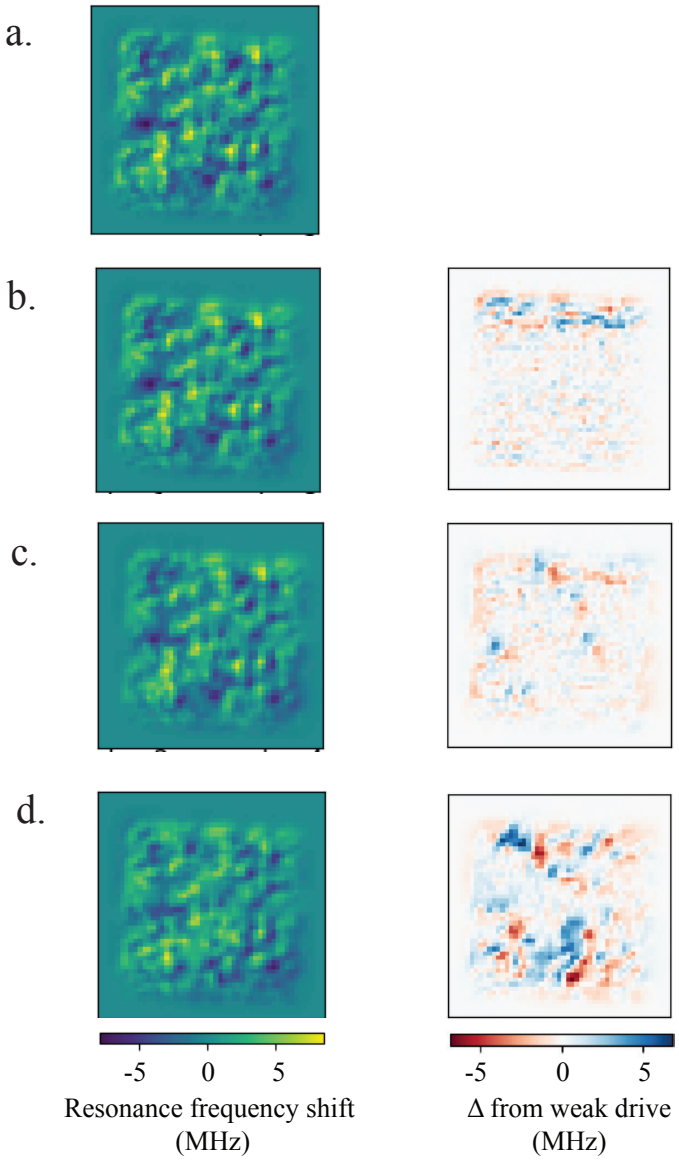


Figure 3.4: **Influence of the microwave field on the magnetization reversal at fixed static field.** NV f_{res} maps of the ASI acquired during the reversal at increasing microwave drive power (top to bottom). Left column: the measured f_{res} maps. Right column: the difference between each map and the one acquired at the lowest drive power. At the two lowest powers ($P_{\mathrm{MW}} = -25$ and -20 dBm), representative of the powers used for imaging, the difference maps are featureless and the inferred switching is indistinguishable from the static-field reversal of Fig. 3.3. At the highest power ($P_{\mathrm{MW}} = -1$ dBm) the difference map reveals a visibly modified switching pattern, showing that sufficiently strong microwave driving perturbs the reversal trajectory.

3.4 Effect of the microwave field on ASI magnetic field reversal

For our NV ensemble magnetic field imaging the microwave drive is delivered through the stripline approximately normal to the ASI plane, and is applied at the NV electronic spin resonance frequency rather than at the ferromagnetic resonance of the island macrospins. We therefore expect the microwave field to have minimal influence on the ASI magnetization reversal at the modest powers used for NV ODMR-imaging. To test this, we image the switching process under a range of microwave drive powers (Fig. 3.4): at the powers used for imaging the reversal is indistinguishable from the static-field reversal alone (Fig. 3.3), and only under substantially stronger driving does the microwave field visibly alter the switching pattern. The microwave power used for ODMR imaging therefore sits well below the threshold at which the drive measurably affects the reversal, so the field maps reported here reflect the intrinsic static-field reversal of the ASI. Where any residual microwave perturbation must be avoided, all-optical NV sensing provides an alternative that does not require resonant microwave driving [87, 88].

3.5 Discussion and outlook

We have demonstrated NV-ensemble magnetic-field imaging as a quantitative probe of magnetization reversal in pinwheel ASI at room temperature. The local stray-field maps acquired during a stepped field ramp resolve the full reversal trajectory of the superferromagnetic structure, from a uniformly magnetized state, through nucleation and growth of mesoscopic domains, to the reversed uniform state. These maps are reproduced quantitatively by mumax3 micromagnetic simulations of the corresponding uniform-magnetization slab, including the post-reversal enhance-

ment of the stray field that we attribute to a more uniform intra-island magnetization after reversal. The reversal trajectory is stochastic but seeded at the same locations across repeated cycles [77,84], and is unperturbed by the microwave drive used for imaging (Section 3.4).

Because the imaging parameter is the magnetic field rather than the magnetization itself, NV ensemble imaging is selectively sensitive to non-uniform magnetization configurations such as array edges, domain boundaries, and emergent magnetic monopoles; where the magnetization itself is required, NV studies have previously relied on forward-model fitting or constrained inversion [89–91]. NV ensemble readout captures the entire array in every field step providing direct access to many islands at once and to the spatial features of the reversal, in contrast to scanning single-NV magnetometry [81, 82], which trades field of view and acquisition speed for nanoscale spatial resolution. The modular drop-on diamond-microchip platform [83] makes the approach compatible with a wide range of patterned ASI samples without sample-specific NV fabrication, and the ambient-temperature operation removes the cryogenic constraint of synchrotron techniques such as XMCD-PEEM [76, 79].

These capabilities position NV ensemble magnetic imaging as a versatile tool for emergent ASI phenomena across geometries and timescales. Complementary NV-based sensing protocols, including dynamical decoupling sequences and T_1 relaxometry, would extend the modality from static field maps to the stochastic dynamics underlying phase transitions and slow ordering in ASI [76, 77], with temporal and spatial correlation parameters measurable simultaneously across the full array. Larger lattice constants or improved spatial resolution would expose single-island stray-field signatures and enable direct comparison with micromagnetic simulators such as flatspin [92]. A natural next step is to recover the full vector magnetization and track it through

the stochastic reversal dynamics. Extending the technique to alternative geometries (kagome, three-dimensional, and larger pinwheel arrays of several hundred microns) would further leverage NV-ensemble magnetic imaging to access classes of ASI behavior that complement the reach of existing techniques.

Conclusion

In Chapter 1 we used spatially resolved NV magnetometry to image the nonlinear scattering dynamics of magnons in a thin film of yttrium iron garnet, isolating the elementary four-magnon interaction with a two-tone wave-mixing protocol and extracting its strength directly from the spatial growth profile of the scattering product. The measured coupling exceeds the standard T-matrix prediction [47], a discrepancy we attribute to the restriction to $k_x = 0$ in our scattering model: in practice, magnons also scatter into $k_x \neq 0$ modes, inflating the extracted coupling beyond the prediction. Under strong single-tone driving, the system organizes into a spontaneous cascade of discrete, power-tunable parametric resonances whose growth is maximized along the slow-magnon contours where the group velocity vanishes. This resolves the pre-thermal approach to equilibrium as a structured hierarchy of discrete scattering channels rather than a diffusive continuum, in contrast to the continuum picture of wave turbulence theory [15]. The measurement rests on the absolute, calibrated, spatially resolved field readout of NV magnetometry, which turns propagation distance into a proxy for interaction time. In future work using NV magnetometry, spatially mapping the second-order coherence $g^{(2)}$ of the scattering products could expose the pairwise correlations that distinguish this discrete cascade from a stochastic turbulent flow.

In Chapter 2 we introduced a dressed-state spectrum analyzer that extends NV noise magnetometry beyond the Rabi-rate limit. Embedding an off-resonant microwave probe in a dynamical-

decoupling sequence uses the AC Stark shift to parametrically mix the probe with the target noise, so the accessible center frequency is set by the probe rather than the pulse repetition rate and is continuously tunable [9]. We validated the method on artificial test signals against a commercial spectrum analyzer, then applied it to a YIG thin film to extract the thermal magnon noise spectrum and group velocity at frequencies hundreds of megahertz above the NV resonance, beyond the reach of conventional NV dynamical decoupling measurements. The present method preserves the nanoscale spatial resolution of NV sensing while substantially extending its frequency reach: higher Rabi rates would push the accessible bandwidth to several gigahertz, and the protocol can carry over to scanning-probe NV microscopy and to other qubit platforms that exhibit an AC Stark shift.

In Chapter 3 we applied NV-ensemble magnetic-field imaging to artificial spin ice for the first time, placing an NV diamond microchip directly on a pinwheel array and mapping its stray fields through a field-driven reversal at room temperature. The maps resolve the full reversal of the superferromagnetic domain structure, from a uniform configuration through the nucleation, growth, and coalescence of mesoscopic domains to the reversed uniform state; repeated cycles show that the reversal is stochastic yet nucleates at the same locations. Micromagnetic simulations reproduce the measured magnetic field maps, and a control measurement confirms that the microwave sensing field does not perturb the reversal [10]. Because a dense NV ensemble images the whole array at once, NV magnetometry supplies quantitative, non-invasive vector field maps at sub-micron resolution under ambient conditions, where prior approaches required cryogenic or single-probe scanning techniques [2]; NV dynamical-decoupling and T_1 relaxometry could extend these static maps to stochastic dynamics, and the technique applies directly to other artificial spin

ice geometries.

Across the three projects, the common thread is the use of NV centers as a quantitative, nanoscale interface to magnetic phenomena that are difficult to reach by other means. Each project extends NV magnetometry along a different direction: imaging the spatial structure of nonlinear many-body dynamics, extending the accessible frequency range of noise spectroscopy, and bringing NV confocal imaging to lithographically patterned magnetic systems. Together they reinforce the standing utility of NV magnetometry as a central tool for probing magnetism at the nanoscale, whose room-temperature operation, calibrated field readout, and compatibility with diverse sample environments position it to address an expanding range of condensed matter questions [1, 2, 4].

Appendix A: Supplementary Information: Spatially Resolving the Pre-Thermal Anatomy of a Driven Bosonic Fluid

A.1 Sample Fabrication and Experimental Setup

A.1.1 YIG Thin Film

We use the technique described in [42] to image magnon wavelength for a series of magnetic field values. Using this information, we fit the dispersion relation of the magnons to obtain the saturation magnetization of the material. For the other constants, we use the generally accepted values in the literature. The relevant YIG film parameters used throughout this work are:

$$\begin{aligned} &D = 100\,\text{nm}, && M_s = 1.55 \times 10^5\,\text{A/m}\ (= 155\,\text{emu/cc}), \\ &\alpha = 10^{-4} && A_{\text{ex}} = 3.7 \times 10^{-12}\,\text{J/m}\ (= 3.7 \times 10^{-7}\,\text{erg/cm}), \end{aligned} \tag{A.1}$$

where D is the film thickness, M_s is the saturation magnetization, A_{ex} is the exchange stiffness, and α is the Gilbert damping constant. Additionally, the NV axis makes an angle $\theta_{\text{NV}} = -71^\circ$ with the film normal.

A.2 NV Center Physics

The NV center forms an electronic spin triplet, where the $m_S = \pm 1$ states are degenerate and split from the $m_S = 0$ state by the zero-field splitting $\Delta/(2\pi) = 2.87$ GHz. Applying a static magnetic field H^z lifts the degeneracy of the $m_S = \pm 1$ states. The Hamiltonian of a single NV center located at $\boldsymbol{r}_i$ interacting with a transverse oscillating magnetic field is:

$$\mathcal{H}_{\mathrm{NV}} = \frac{\Delta - \gamma H^z}{2}\left[\sigma^0 - \sigma^z\right] + \frac{\gamma}{\sqrt{2}}\left[H^+(\boldsymbol{r}_i, t)\sigma^- + H^-(\boldsymbol{r}_i, t)\sigma^+\right] \tag{A.2}$$

where σ^0 is the identity matrix, $\sigma^{\pm} = (\sigma^x \pm i\sigma^y)/2$, and $H^{\pm} = H^x \pm iH^y$ [93]. Throughout, $\gamma = \mu_0\gamma_e$ denotes the electron gyromagnetic ratio scaled by the vacuum permeability, with $\gamma_e = 2\pi \times 28$ GHz/T, so that γH is an angular frequency for fields and magnetizations expressed in A/m.

A.2.1 Coherent Dynamics: Rabi Frequency

When the local transverse field is a monochromatic coherent wave on resonance with the lower transition ($\omega \approx \Delta - \gamma H^z$), the system undergoes deterministic Rabi oscillations between $|0\rangle$ and $|-1\rangle$. Evaluating the Schrödinger equation in the rotating wave approximation yields a local transition probability $P_i(t) = \sin^2(\Omega_{R,i}t)$, where the squared local Rabi frequency is defined directly by:

$$\Omega_{R,i}^2 = \frac{\gamma^2}{2} H^+(\boldsymbol{r}_i, t) H^-(\boldsymbol{r}_i, t)\,. \tag{A.3}$$

A.2.2 Incoherent Dynamics: T_1 Transition Probability

Conversely, evaluating the transition probability via Fermi's Golden Rule allows us to establish the incoherent NV spin T_1 dynamics on the same footing. Treating the transverse field as a perturbation $\mathcal{H}'$ in the interaction picture, the probability of an upward transition $P_i^{\uparrow} \equiv P_i^{0\leftarrow -1}$ evaluates to:

$$\begin{aligned} P_i^{\uparrow} &= \left| \frac{1}{i} \int_0^t \mathrm{d}t' \, \langle 0 | \, \mathcal{H}'_I(t') \, | -1 \rangle \right|^2 \\ &= \frac{\gamma^2}{2} \int_0^t \mathrm{d}t_1 \, \mathrm{d}t_2 e^{-i\omega_{\mathrm{NV}}(t_1 - t_2)} H^-(\boldsymbol{r}_{\mathrm{NV}}^i, t_1) H^+(\boldsymbol{r}_{\mathrm{NV}}^i, t_2) \end{aligned} \tag{A.4}$$

where $\omega_{\mathrm{NV}} = \Delta - \gamma H^z$. Similarly, for the downward process $P_i^{\downarrow} \equiv P_i^{-1\leftarrow 0}$:

$$P_i^{\downarrow} = \frac{\gamma^2}{2} \int_0^t \mathrm{d}t_1 \, \mathrm{d}t_2 e^{i\omega_{\mathrm{NV}}(t_1 - t_2)} H^+(\boldsymbol{r}_{\mathrm{NV}}^i, t_1) H^-(\boldsymbol{r}_{\mathrm{NV}}^i, t_2) \tag{A.5}$$

Taking Fourier transformations isolates the frequency filtering components:

$$P_i^{\uparrow,\downarrow} = \frac{\gamma^2}{2} \int \frac{\mathrm{d}\omega \, \mathrm{d}\omega'}{(2\pi)^2} W_{\mathrm{T1}}^{\uparrow,\downarrow}(\omega, \omega') K_i^{\uparrow,\downarrow}(\omega, \omega') \tag{A.6}$$

where we introduced the magnetic field kernels:

$$K_i^{\uparrow}(\omega, \omega') = \int \mathrm{d}t_1 \, \mathrm{d}t_2 e^{-i\omega t_1 - i\omega' t_2} H^-(\boldsymbol{r}_{\mathrm{NV}}^i, t_1) H^+(\boldsymbol{r}_{\mathrm{NV}}^i, t_2) \, , \tag{A.7}$$

$$K_i^{\downarrow}(\omega, \omega') = \int \mathrm{d}t_1 \, \mathrm{d}t_2 e^{-i\omega t_1 - i\omega' t_2} H^+(\boldsymbol{r}_{\mathrm{NV}}^i, t_1) H^-(\boldsymbol{r}_{\mathrm{NV}}^i, t_2) \, , \tag{A.8}$$

and the corresponding frequency filtering functions:

$$W_{\mathrm{T1}}^{\uparrow}(\omega,\omega') = \frac{e^{-i(\omega_{\mathrm{NV}}-\omega)t}-1}{(\omega_{\mathrm{NV}}-\omega)}\frac{e^{i(\omega_{\mathrm{NV}}+\omega')t}-1}{(\omega_{\mathrm{NV}}+\omega')}\,, \tag{A.9}$$

$$W_{\mathrm{T1}}^{\downarrow}(\omega,\omega') = \frac{e^{i(\omega_{\mathrm{NV}}+\omega)t}-1}{(\omega_{\mathrm{NV}}+\omega)}\frac{e^{-i(\omega_{\mathrm{NV}}-\omega')t}-1}{(\omega_{\mathrm{NV}}-\omega')}\,. \tag{A.10}$$

For large enough times $t \gg \tau$ (where τ is the decay timescale of $K_i^{\uparrow,\downarrow}$), $W_{\mathrm{T1}}^{\uparrow}(\omega,\omega')$ is strongly peaked at $\omega \approx \omega_{\mathrm{NV}}$ and $\omega' \approx -\omega_{\mathrm{NV}}$, in which case we find $W_{\mathrm{T1}}^{\uparrow}(\omega_{\mathrm{NV}},-\omega_{\mathrm{NV}}) = t^2$. The same holds for interchanging ω and ω' in the downward process.

A.3 Magnon Physics and NV Coupling

We present the effective Hamiltonian of the driven magnon system, assuming a quartic nonlinearity. The third-order nonlinearity is kinematically disallowed in our target frequency range. The effective Hamiltonian is:

$$\frac{\mathcal{H}}{V} = \sum_{\boldsymbol{k}}(\omega_{\boldsymbol{k}} - i\Gamma_{\boldsymbol{k}})\Psi_{\boldsymbol{k}}^*\Psi_{\boldsymbol{k}} + \frac{1}{2}\sum_{\boldsymbol{k}_1,\boldsymbol{k}_2,\boldsymbol{k}_3,\boldsymbol{k}_4} g_{34}^{12}\delta_{34}^{12}\Psi_{\boldsymbol{k}_1}^*\Psi_{\boldsymbol{k}_2}^*\Psi_{\boldsymbol{k}_3}\Psi_{\boldsymbol{k}_4} + \sum_{\boldsymbol{k}}\left[S_{\boldsymbol{k}}(t)\Psi_{\boldsymbol{k}}^*(t) + \text{c.c.}\right] \tag{A.11}$$

The first term captures the kinetic energy of magnons with dispersion relation $\omega_{\boldsymbol{k}}$ and Gilbert damping $\Gamma_{\boldsymbol{k}} = \alpha\omega_{\boldsymbol{k}}$. The second term describes momentum-dependent scattering with coupling strength g_{34}^{12}, where δ_{34}^{12} enforces momentum conservation. The final term models the coherent stripline drive $S_{\boldsymbol{k}}(t)$. This Hamiltonian yields the equations of motion:

$$i\partial_t\Psi_{\boldsymbol{k}}(t) = \frac{\delta\mathcal{H}/V}{\delta\Psi_{\boldsymbol{k}}^*(t)} = (\omega_{\boldsymbol{k}} - i\Gamma_{\boldsymbol{k}})\Psi_{\boldsymbol{k}} + \sum_{\boldsymbol{k}_1,\boldsymbol{k}_2,\boldsymbol{k}_3} g_{3k}^{12}\delta_{3k}^{12}\Psi_1\Psi_2\Psi_3^* + S_{\boldsymbol{k}}(t) \tag{A.12}$$

Before solving this equation, we connect the phenomenological constants $\omega_{\boldsymbol{k}}$, g_{34}^{12}, and $S_{\boldsymbol{k}}$ to their microscopic origins and demonstrate how this continuum model governs the interaction with the macroscopic NV ensemble.

A.3.1 Dispersion Relation

The derivation of the dispersion relation $\omega_{\boldsymbol{k}}$ of exchange dipole magnons in thin films is established in standard literature [41, 93]. The full dispersion relation evaluates to $\omega(k, \phi_k) = \sqrt{\omega_2 \omega_3 - \omega_1^2}$, where:

$$\omega_1 = \gamma H_{\mathrm{d}} \sin\phi_k \cos\phi_k \cos\theta_0 f_k, \tag{A.13}$$

$$\omega_2 = \gamma \left[H_{\mathrm{int}} + H_{\mathrm{ex}} k^2 + H_{\mathrm{d}} \cos^2\phi_k f_k \cos^2\theta_0 + H_{\mathrm{d}}(1 - f_k) \sin^2\theta_0 \right], \tag{A.14}$$

$$\omega_3 = \gamma \left[H_{\mathrm{int}} + H_{\mathrm{ex}} k^2 + H_{\mathrm{d}} \sin^2\phi_k f_k \right], \tag{A.15}$$

where the demagnetization field is $H_{\mathrm{d}} = M_s$ and the exchange field is $H_{\mathrm{ex}} = 2A_{\mathrm{ex}}/(\mu_0 M_s)$. The internal magnetic field is $H_{\mathrm{int}} = H_{\mathrm{ext}} \cos(\theta - \theta_0) - H_{\mathrm{d}} \cos^2(\theta_0)$ where θ specifies the angle of the applied external magnetic field H_{ext}, and θ_0 represents the equilibrium magnetization angle. The demagnetization form factor is $f_k = 1 - (1 - \exp(-kD))/(kD)$.

Given our magnetic field aligns perpendicular to the axis of magnon propagation ($\phi_k = \pi/2$), we evaluate the Damon–Eshbach (DE) mode [94]:

$$\omega_{\mathrm{DE}}(k) = \gamma \sqrt{\left[H_{\mathrm{ext}} + H_{\mathrm{ex}} k^2 + H_{\mathrm{d}}(1 - f_k)\right] \left[H_{\mathrm{ext}} + H_{\mathrm{ex}} k^2 + H_{\mathrm{d}} f_k\right]}. \tag{A.16}$$

Expanding this to linear order yields $\omega_{\mathrm{lin}}^{\mathrm{DE}}(k_y) = \Delta_0 + v_y k_y$, where the gap is $\Delta_0 =$

$\gamma\sqrt{H_{\text{ext}}(H_{\text{d}}+H_{\text{ext}})}$ and the group velocity is $v_y \equiv v_{\text{DE}} = \gamma H_{\text{d}}^2 D/(4\sqrt{H_{\text{ext}}(H_{\text{d}}+H_{\text{ext}})})$. This linear form underlies the analytic selection rules and resonance condition derived in Sec. A.6; the numerical idler and growth-rate calculations (Sec. A.5, Sec. A.6.8) instead use the exact group velocity $v_g = \partial\omega/\partial k$, which falls below v_{DE} where the dispersion flattens at the experimental wavevectors.

A.3.2 Injection Profile

The magnetic field generated by the stripline determines the injection profile $S_{\boldsymbol{k}}$. Evaluating the Biot-Savart law for a current density $\boldsymbol{J}(\boldsymbol{\rho}, z, t) = \hat{x}\, I/(WH) f(y/W)\cos(\omega_d t)$ localized at $z = D/2$ yields the in-plane Fourier transformed field:

$$\boldsymbol{B}_{\boldsymbol{k}}(t) = -\mu_0 I \delta(k_x) h(k_y H) w(k_y W)\,[\hat{y} + i\,\text{sgn}(k_y)\hat{z}]\cos(\omega_d t) \tag{A.17}$$

where $w(k_y W)$ is the Fourier transform of the lateral current distribution and $h(k_y H) = (1 - \exp(-|k_y|H))/(|k_y|H)$.

The stripline field couples linearly to the dynamic magnetization. After projection onto the driven Damon–Eshbach branch, the effective source inherits the geometric momentum profile and directional polarization of the microwave field. We therefore parameterize it as

$$S_{\boldsymbol{k}}(t) = i\, S_0\, h(k_y H) w(k_y W)\theta(k_y)\delta_{k_x}\cos(\omega_d t) \tag{A.18}$$

where $S_0 \propto I$ contains the polarization and mode-overlap factors. The form factors h and w determine the momentum width of the injected mode, while $\theta(k_y)$ captures the chirality of the

DE-modes, confirming that injection occurs exclusively at positive momenta for the top surface of the sample.

A.3.3 Magnetic Field at the NV Center

The stray magnetic field at the NV center generated by the underlying magnons is evaluated within the near-field approximation. Performing an in-plane Fourier transform maps the sample magnetization to the local NV position $\boldsymbol{r}^i_{\mathrm{NV}}$ via the effective magnetostatic dipole tensor $\tilde{D}_{\boldsymbol{q}}$:

$$H^{\alpha}(\boldsymbol{\rho}^i_{\mathrm{NV}}, t) = \int \frac{\mathrm{d}\boldsymbol{q}}{(2\pi)^2} e^{-i\boldsymbol{q}\cdot\boldsymbol{\rho}^i_{\mathrm{NV}}} \tilde{D}^{\alpha\beta}_{\boldsymbol{q}} \tilde{m}^{\beta}_{\boldsymbol{q}}(t)\,, \tag{A.19}$$

where $\tilde{D}_{\boldsymbol{q}} = R_y(\theta_{\mathrm{NV}}) D_{\boldsymbol{q}}(z_{\mathrm{NV}}) R_y^T(\theta_0)$ applies the rotational matrices necessary to align the lab frame with the local quantization axes. The dipole tensor evaluates to:

$$D_{\boldsymbol{q}}(z_{\mathrm{NV}}) = -e^{-qz_{\mathrm{NV}}} \frac{1 - e^{-qD}}{2q} \begin{bmatrix} q_x^2/q & q_x q_y/q & iq_x \\ q_x q_y/q & q_y^2/q & iq_y \\ iq_x & iq_y & -q \end{bmatrix}. \tag{A.20}$$

A.3.4 Ensemble Averaging and Momentum Filter Tensors

The optical measurement integrates photon counts across the confocal volume, mapping local NV spin transitions to a macroscopic extensive observable. The coherent transition rate depends directly on the spatial sum of the field products across the i NV centers. Expanding this

product into momentum space yields:

$$\sum_{i\in W} H^{\alpha}(\boldsymbol{\rho}^i_{\mathrm{NV}}, t_1) H^{\alpha'}(\boldsymbol{\rho}^i_{\mathrm{NV}}, t_2)$$
$$= \int \frac{\mathrm{d}\boldsymbol{q}}{(2\pi)^2} \int \frac{\mathrm{d}\boldsymbol{q}'}{(2\pi)^2} \sum_i e^{-i(\boldsymbol{q}+\boldsymbol{q}')\cdot\boldsymbol{\rho}^i_{\mathrm{NV}}} \tilde{D}^{\alpha\beta}_{\boldsymbol{q}} \tilde{m}^{\beta}_{\boldsymbol{q}}(t_1) \tilde{D}^{\alpha'\beta'}_{\boldsymbol{q}'} \tilde{m}^{\beta'}_{\boldsymbol{q}'}(t_2)\,. \tag{A.21}$$

Approximating the discrete spatial sum as a continuous integral over the NV density $1/d^2_{\mathrm{NV}}$ generates a momentum-conserving Dirac delta function for a sufficiently large confocal spot. This collapses the cross-momentum integration ($\boldsymbol{q}' = -\boldsymbol{q}$):

$$\sum_{i\in W} H^{\alpha}(\boldsymbol{\rho}^i_{\mathrm{NV}}, t_1) H^{\alpha'}(\boldsymbol{\rho}^i_{\mathrm{NV}}, t_2) \approx \frac{1}{d^2_{\mathrm{NV}}} \int \frac{\mathrm{d}\boldsymbol{q}}{(2\pi)^2} \tilde{D}^{\alpha\beta}_{\boldsymbol{q}} \tilde{D}^{\alpha'\beta'}_{-\boldsymbol{q}} \tilde{m}^{\beta}_{\boldsymbol{q}}(t_1) \tilde{m}^{\beta'}_{-\boldsymbol{q}}(t_2)\,. \tag{A.22}$$

Expressing the transverse magnetization components in the circular basis, $\tilde{m}^{\pm} = \tilde{m}^x \pm i\tilde{m}^y$, organizes the tensor contraction into the geometric kernels $\tilde{\mathcal{D}}^{\uparrow\downarrow,\sigma\sigma'}_{\boldsymbol{q}}$. The superscripts $\uparrow$ and $\downarrow$ label the field combinations $H^- H^+$ and $H^+ H^-$ associated with the two NV transition channels. These

filter functions evaluate to:

$$\tilde{\mathcal{D}}_{\boldsymbol{q}}^{\uparrow,\pm\pm} = \left[1 - e^{-qD}\right]^2 \frac{e^{-2qz_{\mathrm{NV}}}}{16q^4} \left[-\left(q_y \pm i q_x \cos\theta_0\right)^2 + q^2 \sin^2\theta_0\right] \times \left[q_x^2 \cos^2\theta_{\mathrm{NV}} + \left(q_y + q\sin\theta_{\mathrm{NV}}\right)^2\right] ,$$

$$\tilde{\mathcal{D}}_{\boldsymbol{q}}^{\uparrow,\pm\mp} = \left[1 - e^{-qD}\right]^2 \frac{e^{-2qz_{\mathrm{NV}}}}{16q^4} \left[q_x^2 \cos^2\theta_0 + \left(q_y \mp q\sin\theta_0\right)^2\right] \times \left[q_x^2 \cos^2\theta_{\mathrm{NV}} + \left(q_y + q\sin\theta_{\mathrm{NV}}\right)^2\right] ,$$

$$\tilde{\mathcal{D}}_{\boldsymbol{q}}^{\downarrow,\pm\pm} = \left[1 - e^{-qD}\right]^2 \frac{e^{-2qz_{\mathrm{NV}}}}{16q^4} \left[-\left(q_y \pm i q_x \cos\theta_0\right)^2 + q^2 \sin^2\theta_0\right] \times \left[q_x^2 \cos^2\theta_{\mathrm{NV}} + \left(q_y - q\sin\theta_{\mathrm{NV}}\right)^2\right] ,$$

$$\tilde{\mathcal{D}}_{\boldsymbol{q}}^{\downarrow,\pm\mp} = \left[1 - e^{-qD}\right]^2 \frac{e^{-2qz_{\mathrm{NV}}}}{16q^4} \left[q_x^2 \cos^2\theta_0 + \left(q_y \mp q\sin\theta_0\right)^2\right] \times \left[q_x^2 \cos^2\theta_{\mathrm{NV}} + \left(q_y - q\sin\theta_{\mathrm{NV}}\right)^2\right] . \tag{A.23}$$

These kernels encode the angular selection rules and the evanescent decay. As plotted in Fig. A.1(a), given the experimental angle $\theta_{\mathrm{NV}} = -71^\circ$ and the equilibrium magnetization angle θ_0, the dominant contributions along the propagation axis q_y arise exclusively from the density-like terms $\tilde{\mathcal{D}}_{\boldsymbol{q}}^{\downarrow,+-}$ and $\tilde{\mathcal{D}}_{\boldsymbol{q}}^{\uparrow,-+}$. The anomalous terms ($\pm\pm$) are geometrically suppressed.

A.3.5 Macroscopic Rabi Frequency

When a magnon mode acquires a macroscopic population under a strong coherent drive, the stochastic fluctuations condense into a deterministic classical field, driving coherent transitions.

Because the optical measurement integrates photon counts across the entire confocal volume, the observed photoluminescence contrast reflects the ensemble-averaged transition probability of

the defects within the spot. To ensure thermodynamic consistency at room temperature, the ferrimagnetic lattice is mapped to an effective continuum ferromagnet using the effective macroscopic spin density s_{eff} (defined directly by the measured saturation magnetization via $M_s = \gamma_e \hbar s_{\text{eff}}$). The transformation is:

$$\tilde{m}^{+}_{\boldsymbol{q}}(t) = M_s \sqrt{\frac{2}{s_{\text{eff}}}} \alpha_{\boldsymbol{q}}(t)\,, \qquad \text{and} \qquad \tilde{m}^{-}_{\boldsymbol{q}}(t) = M_s \sqrt{\frac{2}{s_{\text{eff}}}} \alpha^{*}_{-\boldsymbol{q}}(t)\,. \tag{A.24}$$

In the coherent driven regime, the dynamics are governed by deterministic, monochromatic spin waves $\alpha_{\boldsymbol{q}}(t) = \alpha_{\boldsymbol{q}} e^{-i\omega_{\boldsymbol{q}} t}$. The extensive sum of the squared Rabi frequencies across the illuminated NV ensemble evaluates to:

$$\sum_i \Omega^2_{R,i} = \frac{\gamma^2 M_s^2}{s_{\text{eff}} d^2_{\text{NV}}} \int \frac{\mathrm{d}\boldsymbol{q}}{(2\pi)^2} \tilde{\mathcal{D}}^{\downarrow,+-}_{\boldsymbol{q}} \langle n_{\boldsymbol{q}} \rangle\,, \tag{A.25}$$

where $\langle n_{\boldsymbol{q}} \rangle = |\alpha_{\boldsymbol{q}}|^2$.

A.3.6 1D Propagation and Population Extraction

We model the driven magnon mode as a 1D wavepacket propagating along the y-direction. Because the spatial decay length of the magnon fluid is much larger than its carrier wavevector, we approximate the momentum spectrum by a Dirac delta function: $\langle n_{\boldsymbol{q}} \rangle = \langle \tilde{n}_0 \rangle (2\pi)^2 A_{\text{spot}} \delta(q_x) \delta(q_y - q_0)$. Furthermore, because a plane wave generates a spatially uniform field magnitude, every defect in the ensemble experiences an identical driving amplitude. The extensive NV ensemble sum thus reduces to the local single-spin value scaled by the spot area: $d^2_{\text{NV}} \sum_i \Omega^2_{R,i} \equiv A_{\text{spot}} \Omega^2_R$.

We now evaluate the detection efficiency for the driven mode at $q_x = 0$. Shape anisotropy renders the precession elliptical: the mode carries an in-plane transverse component and a smaller out-of-plane component in quadrature, with amplitude ratio $\eta \leq 1$ set by the dispersion [8]. Both components contribute coherently to the stray field above the film, yielding the phase-dependent geometric factor:

$$\mathcal{G}_\eta(s, \theta_{\mathrm{NV}}, \theta_0) = \frac{1}{\sqrt{\eta}} \left(1 - s\,\eta \cos\theta_0\right) \left(s - \sin\theta_{\mathrm{NV}}\right) , \tag{A.26}$$

where $s = \mathrm{sgn}(q_y) = \pm 1$ encodes the propagation direction of the detected mode and θ_0 is the small out-of-plane cant of the static magnetization. The factor $(1 - s\,\eta\cos\theta_0)$ sets the chirality of the spin-wave stray field, the factor $(s - \sin\theta_{\mathrm{NV}})$ projects the circularly polarized stray field onto the co-rotating component at the NV, and the prefactor $1/\sqrt{\eta}$ captures the larger transverse magnetization per magnon of an elliptical mode. The corresponding generalized filter tensor takes the form:

$$\tilde{\mathcal{D}}_\eta^{\mathrm{eff}}(q_0) = e^{-2|q_0|z_{\mathrm{NV}}} \left[\frac{1 - e^{-|q_0|D}}{4}\right]^2 |\mathcal{G}_\eta|^2 . \tag{A.27}$$

Substituting these spatial boundaries and elliptical limits into Eq. (A.25) cancels the spot area coefficients identically, yielding:

$$\Omega_R^2 = \frac{\gamma^2 M_s^2}{16 s_{\mathrm{eff}}} e^{-2|q_0|z_{\mathrm{NV}}} \left[1 - e^{-|q_0|D}\right]^2 |\mathcal{G}_\eta|^2 \langle \tilde{n}_0 \rangle . \tag{A.28}$$

Inverting this relation extracts the volumetric magnon population density $\langle \tilde{n}_0 \rangle$ directly from the

measured Rabi frequency:

$$\langle \tilde{n}_0 \rangle = s_{\text{eff}} \left(\frac{4\Omega_R}{\gamma M_s |\mathcal{G}_\eta|} \right)^2 \frac{e^{2|q_0|z_{\text{NV}}}}{\left(1 - e^{-|q_0|D}\right)^2} \,. \tag{A.29}$$

This matches the expression quoted as Eq. (1.1) by setting $\boldsymbol{q}_0 \equiv \boldsymbol{k}$, with the coupling constant $\mathcal{C}$ collecting the saturation magnetization together with the geometric, evanescent, and ellipticity prefactors:

$$\mathcal{C} \equiv M_s \, e^{-|q_0|z_{\text{NV}}} \frac{1 - e^{-|q_0|D}}{4} |\mathcal{G}_\eta| \,. \tag{A.30}$$

A.4 Height Mapping

To perform the density mapping detailed above, we must determine the average separation between the NV ensemble and the YIG film (z_{NV}). We exploit the T_1 measurement protocol, noting that the NVs detect magnetic noise within a specific momentum window governed by the $e^{-2qz_{\text{NV}}}$ filter tensor suppression. We sweep the magnetic field from approximately 12 mT to 30 mT. As the applied field increases, the resonant wavevector $\boldsymbol{k}$ decreases, increasing sensitivity to thermal magnons until the relaxation rate peaks near $|\boldsymbol{k}| \approx 1/(2z_{\text{NV}})$. We fit this response to extract the local separation.

A.4.1 Thermal Magnon Noise and T_1 Relaxation

Unlike the Rabi response driven by a coherent mode, the incoherent T_1 transition rate is driven by broadband thermal magnetic field fluctuations. However, the geometric coupling remains

strictly governed by the exact same momentum filter functions $\tilde{\mathcal{D}}_{\boldsymbol{q}}^{\uparrow\downarrow,\sigma\sigma'}$ established in Sec. A.3.

To model this thermal noise at room temperature and GHz frequencies ($\hbar\omega \ll k_B T$), we relate the equilibrium transverse magnetization fluctuations to the dynamic susceptibility $\chi_{\alpha\beta}(\boldsymbol{q},\omega)$ via the classical fluctuation-dissipation theorem:

$$C_{\alpha\beta}(\boldsymbol{q},\omega) = \frac{2k_B T}{\omega} \operatorname{Im} \chi_{\alpha\beta}(\boldsymbol{q},\omega)\,. \tag{A.31}$$

Substituting this thermal spectrum into the momentum integrals established by Fermi's Golden Rule yields the explicit functional form for $\Gamma^{\uparrow,\downarrow}(H_{\text{ext}})$.

A.4.2 Height Map Calculation

By performing the T_1 measurements across the diamond chip, we construct a spatial map of the NV-YIG separation. We plot these data points in Fig. A.1(c), along with the corresponding fits to the thermal magnon noise model. The fitted z_{NV} values range from approximately 250 nm to 500 nm as seen in Fig. A.1(b), reflecting non-uniform contact between the diamond and YIG surfaces. We use the locally-determined z_{NV} at each position to accurately calculate the magnon population densities from the measured Rabi frequencies.

A.5 Stimulated Four-Magnon Scattering Model

In this section and the next, we derive the theoretical framework for understanding four-magnon scattering processes observed in our experiments. We first establish a general approximation scheme for solving the nonlinear wave equation, then apply it to the two-tone (stimulated

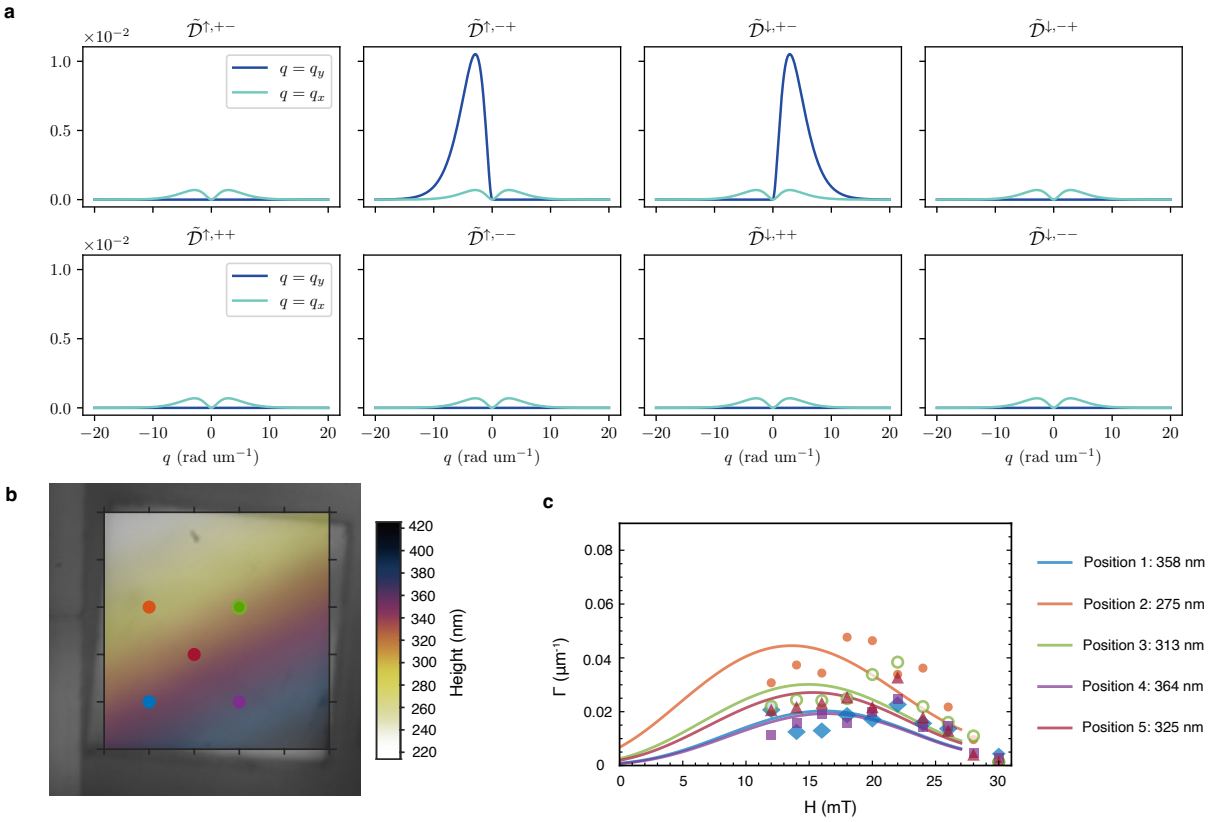


Figure A.1: **Height mapping of NV-YIG separation.** (a) Momentum filter function $\tilde{\mathcal{D}}_{\boldsymbol{q}}^{\downarrow,+-}$ for $\theta_{\mathrm{NV}} = -71^\circ$ and the equilibrium magnetization angle θ_0. Due to the geometry, the dominant contributions along the propagation axis q_y arise from the density-like tensor elements. (b) Spatial map of the diamond chip showing the five measurement positions and the extracted height map of z_{NV} across the chip. The variation in z_{NV} (250–500 nm) reflects non-uniform contact between the diamond and YIG surfaces. (c) T_1 relaxation rate vs. applied magnetic field at five different positions on the diamond chip. Solid lines show fits to the thermal magnon noise model with z_{NV} as the free parameter.

scattering) and single-tone (cascaded scattering) experiments.

A.5.1 Approximation Scheme for Driven Nonlinear Systems

Our starting point is the nonlinear wave equation Eq. (A.12) introduced in Sec. A.3. The full equation couples a continuum of momentum modes through the momentum-dependent four-magnon vertex, while also retaining propagation, damping, and the localized external drive. A

direct time-domain solution would be computationally demanding and offer limited interpretability of the individual resonances observed experimentally. The measurements instead probe a weakly nonlinear, narrowband, continuous-wave regime in which the dominant scattering pathways can be organized systematically around the directly driven mode. We use the following experimentally motivated approximations:

1. **Dominant driven mode.** The mode resonantly excited by the stripline carries the largest coherent population. Secondary modes can therefore be treated as fluctuations about this driven background.

2. **Weak nonlinear frequency scale.** The density-dependent nonlinear shifts and scattering rates, of order $|g|n$, remain small compared with the carrier frequencies of the participating magnons. This separation permits a perturbative expansion in the interaction.

3. **Stationary continuous-wave response.** The microwave tones are applied continuously, and the measurement is performed after propagation and damping transients have decayed. The relevant coherent amplitudes may therefore be described by stationary spatial envelope equations.

These approximations retain the energy- and momentum-matching conditions, spatial propagation, and damping that determine the observed resonances, while separating the individual nonlinear scattering channels.

A.5.2 Bogoliubov Decomposition

Following the first simplifying aspect, we decompose the magnon field into the directly driven mode and fluctuations:

$$\Psi_{\boldsymbol{k}}(t) = \psi_{\boldsymbol{k}}(t) + \delta\psi_{\boldsymbol{k}}(t), \tag{A.32}$$

where $\psi_{\boldsymbol{k}}$ represents the directly driven mode and $\delta\psi_{\boldsymbol{k}}$ captures new modes excited through nonlinear interactions. Substituting this decomposition into Eq. (A.12) and keeping terms to leading order in $\delta\psi$, we obtain for the driven mode:

$$i\partial_t\psi_{\boldsymbol{k}}(t) = (\omega_{\boldsymbol{k}} - i\Gamma_{\boldsymbol{k}})\psi_{\boldsymbol{k}} + \sum_{\boldsymbol{k}_1,\boldsymbol{k}_2,\boldsymbol{k}_3} g^{12}_{3k}\delta^{12}_{3k}\psi_1\psi_2\psi^*_3 + S_{\boldsymbol{k}}(t), \tag{A.33}$$

and for the fluctuations:

$$i\partial_t\delta\psi_{\boldsymbol{k}}(t) = (\omega_{\boldsymbol{k}} - i\Gamma_{\boldsymbol{k}})\delta\psi_{\boldsymbol{k}} + \sum_{\boldsymbol{k}_1,\boldsymbol{k}_2,\boldsymbol{k}_3} g^{12}_{3k}\delta^{12}_{3k}\left[2\delta\psi_1\psi_2\psi^*_3 + \psi_1\psi_2\delta\psi^*_3\right]. \tag{A.34}$$

A.5.3 Perturbative Expansion

Even Eq. (A.33) remains nonlinear. Following the second simplifying aspect, we treat the nonlinearity perturbatively. Introducing a formal expansion parameter ϵ ($g^{12}_{3k} \to \epsilon g^{12}_{3k}$), we expand:

$$\psi_{\boldsymbol{k}} = \psi^{(0)}_{\boldsymbol{k}} + \epsilon\psi^{(1)}_{\boldsymbol{k}} + \epsilon^2\psi^{(2)}_{\boldsymbol{k}} + \ldots \tag{A.35}$$

To zeroth order, interactions are absent:

$$i\partial_t \psi_{\boldsymbol{k}}^{(0)}(t) = \left[\omega_{\boldsymbol{k}} - i\Gamma_{\boldsymbol{k}}\right] \psi_{\boldsymbol{k}}^{(0)}(t) + S_{\boldsymbol{k}}(t). \tag{A.36}$$

For a general multi-tone drive of the form $S_{\boldsymbol{k}}(t) = \sum_j S_{\boldsymbol{k}_j} e^{-i\omega_j t}$, the steady-state solution is:

$$\psi_{\boldsymbol{k}}^{(0)}(t) = \sum_j \frac{S_{\boldsymbol{k}_j}}{\omega_{\boldsymbol{k}} - \omega_j - i\Gamma_{\boldsymbol{k}}} e^{-i\omega_j t} \equiv \sum_j A_j^{(0)}(\boldsymbol{k} - \boldsymbol{k}_j) e^{-i\omega_j t}, \tag{A.37}$$

where $A_j^{(0)}(\boldsymbol{k} - \boldsymbol{k}_j)$ is the envelope function for the j-th drive tone, peaked around the resonant wavevector $\boldsymbol{k}_j$ satisfying $\omega(\boldsymbol{k}_j) = \omega_j$.

At first order, the driven modes interact to generate new frequency components:

$$\left(i\partial_t - \omega_{\boldsymbol{k}} + i\Gamma_{\boldsymbol{k}}\right) \psi_{\boldsymbol{k}}^{(1)}(t) = \sum_{\boldsymbol{k}_1, \boldsymbol{k}_2, \boldsymbol{k}_3} g_{3k}^{12} \delta_{3k}^{12} \psi_1^{(0)} \psi_2^{(0)} \psi_3^{(0),*}. \tag{A.38}$$

The right-hand side contains products of three zeroth-order fields, generating frequencies that are sums and differences of the input frequencies.

A.5.4 Application to Two-Tone Drive

We now specialize to the two-tone experiment, where we apply simultaneous microwave drives at a pump frequency ω_p and a signal frequency ω_s. The zeroth-order solution Eq. (A.37) becomes:

$$\psi_{\boldsymbol{k}}^{(0)}(t) = A_p(\boldsymbol{k} - \boldsymbol{k}_p) e^{-i\omega_p t} + A_s(\boldsymbol{k} - \boldsymbol{k}_s) e^{-i\omega_s t}, \tag{A.39}$$

where the envelope functions A_p and A_s are determined by the injection profile derived in Sec. A.3, and the wavevectors satisfy the dispersion relation: $\omega_p = \omega(\boldsymbol{k}_p)$ and $\omega_s = \omega(\boldsymbol{k}_s)$.

A.5.5 Derivation of the Idler Envelope Equation

Substituting the two-tone solution Eq. (A.39) into the first-order equation Eq. (A.38), the right-hand side contains terms oscillating at frequencies ω_p, ω_s, $2\omega_p - \omega_s$, and $2\omega_s - \omega_p$. At this level, the labels "pump" and "signal" are completely interchangeable: both $2\omega_p - \omega_s$ and $2\omega_s - \omega_p$ are generated on equal footing. We focus on the idler frequency $\omega_i = 2\omega_p - \omega_s$, which in our experiment is tuned to match the NV resonance.

To derive the spatial evolution of the idler, we assume the envelope functions are slowly varying compared to the carrier wavelength. Writing the idler as $\psi^{(1)}_{\boldsymbol{k}}(t) = A_i(\boldsymbol{k} - \boldsymbol{k}_i)e^{-i\omega_i t}$, where $\boldsymbol{k}_i$ satisfies $\omega(\boldsymbol{k}_i) = \omega_i$, we expand the dispersion relation to linear order:

$$\omega(\boldsymbol{k}) \approx \omega(\boldsymbol{k}_i) + \boldsymbol{v}_{\boldsymbol{k}_i} \cdot (\boldsymbol{k} - \boldsymbol{k}_i), \qquad \text{where} \qquad \boldsymbol{v}_{\boldsymbol{k}_i} = \nabla_{\boldsymbol{k}}\omega\big|_{\boldsymbol{k}=\boldsymbol{k}_i} \tag{A.40}$$

is the group velocity at $\boldsymbol{k}_i$. Transforming to real space via the Fourier convention

$$A(\boldsymbol{k}) = \frac{1}{L^2}\int \mathrm{d}\boldsymbol{r}\, A(\boldsymbol{r})\, e^{i\boldsymbol{k}\cdot\boldsymbol{r}}, \quad A(\boldsymbol{r}) = \sum_{\boldsymbol{k}} A(\boldsymbol{k})e^{-i\boldsymbol{k}\cdot\boldsymbol{r}}, \tag{A.41}$$

we obtain the envelope equation in steady state:

$$\left[\boldsymbol{v}_{\boldsymbol{k}_i} \cdot \nabla + \Gamma_i\right] A_i(\boldsymbol{r}) = -ig^{pp}_{si} A_p^2(\boldsymbol{r}) A_s^*(\boldsymbol{r}) e^{i\boldsymbol{\Delta k}\cdot\boldsymbol{r}}, \tag{A.42}$$

where $\Gamma_i = \Gamma(\boldsymbol{k}_i)$ is the damping rate at the idler wavevector, and $\boldsymbol{\Delta k} = 2\boldsymbol{k}_p - \boldsymbol{k}_s - \boldsymbol{k}_i$ is the phase mismatch. This equation describes stimulated four-magnon scattering: the idler amplitude grows proportionally to $A_p^2 A_s^*$, representing the annihilation of two pump magnons to create a signal and an idler magnon, stimulated by the seeded signal mode.

A.5.6 Solution for Damon–Eshbach Propagation

In our geometry, magnons propagate predominantly along the y-direction (Damon–Eshbach configuration). Restricting to this direction, Eq. (A.42) becomes:

$$\left[v_i^y \partial_y + \Gamma_i\right] A_i(y) = -i g_{si}^{pp} A_p^2(y) A_s^*(y) e^{i\Delta k^y y}, \tag{A.43}$$

where $v_i^y = \mathrm{sgn}(k_i^y)\, v_g(k_i^y)$ is the exact y-component of the group velocity evaluated at the idler wavevector.

Assuming the pump and signal envelopes decay exponentially due to damping:

$$A_p(y) = A_p(0) e^{-\lambda_p y}, \qquad A_s(y) = A_s(0) e^{-\lambda_s y}, \tag{A.44}$$

where $\lambda_{p,s} = \Gamma_{p,s}/v_{p,s}^y$ are the spatial decay rates, Eq. (A.43) can be solved with the boundary condition $A_i(0) = 0$ (no idler at the stripline). Defining $\lambda_i = \Gamma_i/v_i^y$, $\lambda_0 = 2\lambda_p + \lambda_s$, and $A_0 = -i g_{si}^{pp} A_p^2(0) A_s^*(0)/v_i^y$, the solution is:

$$A_i(y) = \frac{A_0}{\lambda_0 - \lambda_i - i\Delta k^y} \left[e^{-\lambda_i y} - e^{(-\lambda_0 + i\Delta k^y) y}\right]. \tag{A.45}$$

For phase-matched propagation ($\Delta k^y = 0$) and negligible idler damping ($\lambda_i \ll \lambda_0$), this simplifies to:

$$A_i(y) \approx \frac{A_0}{\lambda_0}\left[1 - e^{-\lambda_0 y}\right]. \tag{A.46}$$

In the limit of weak pump/signal damping, the idler grows linearly with propagation distance: $A_i(y) \approx A_0 y$. This linear growth regime is characteristic of stimulated four-magnon scattering and underlies our detection scheme.

A.5.7 Connection to Measured Signal

The idler frequency $\omega_i = 2\omega_p - \omega_s$ is tuned to the NV resonance ω_{NV}, so the NV detects the idler alone; the pump and signal are far off-resonance and do not contribute. The idler envelope Eq. (A.45) therefore sets the local magnon population density $\langle \tilde{n}_i(y) \rangle = |A_i(y)|^2$, which maps to the measured Rabi frequency through Eq. (A.29) of Sec. A.3, evaluated with the local separation z_{NV} from Sec. A.4 and the idler wavevector q_y fixed by the dispersion relation.

To extract the four-magnon interaction vertex g_{si}^{pp}, we fit the spatial profile of the measured idler population profile, $\langle \tilde{n}_i(y) \rangle = |A_i(y)|^2$, to the squared magnitude of Eq. (A.45). The source amplitude $A_0 = -ig_{si}^{pp} A_p^2(0) A_s^*(0)/v_i^y$ contains the coupling constant g_{si}^{pp} as an unknown parameter, while the pump and signal amplitudes $A_p(0)$, $A_s(0)$ are independently determined from single-tone Rabi measurements and the stripline current calibration (see Sec. A.7). This fitting procedure yields the extracted values of g_{si}^{pp} shown in Fig. 1.5(F).

A.6 Cascaded Scattering Model

When driving the magnon system with a single tone at frequency ω_0, the directly excited mode can become parametrically unstable above a threshold power, spontaneously generating pairs of magnons at new frequencies. These secondary modes can themselves become unstable, leading to a cascade of parametric resonances. Here we derive the conditions for this cascaded instability and show how it determines the observable resonance structure.

A.6.1 Parametric Instability from Four-Magnon Scattering

We begin with the Bogoliubov decomposition introduced in the previous section. For a single-tone drive, the zeroth-order solution is:

$$\psi_{\boldsymbol{k}}^{(0)}(t) = A_0(\boldsymbol{k} - \boldsymbol{k}_0)e^{-i\omega_0 t}, \tag{A.47}$$

where ω_0 is the drive frequency and $\boldsymbol{k}_0$ satisfies the dispersion relation $\omega(\boldsymbol{k}_0) = \omega_0$. Unlike the two-tone case where we treated the idler perturbatively, here we examine the stability of the driven mode against spontaneous decay into pairs of secondary modes.

The fluctuation equation Eq. (A.34) describes how small perturbations evolve in the presence of the driven mode. We write the fluctuations as a superposition of two modes with frequencies ω_1 and ω_2 constrained by energy conservation ($\omega_1 + \omega_2 = 2\omega_0$):

$$\delta\psi_{\boldsymbol{k}}(t) = A_1(\boldsymbol{k} - \boldsymbol{k}_1)e^{-i\omega_1 t} + A_2(\boldsymbol{k} - \boldsymbol{k}_2)e^{-i\omega_2 t}. \tag{A.48}$$

Momentum conservation requires $\boldsymbol{k}_1 + \boldsymbol{k}_2 = 2\boldsymbol{k}_0$.

A.6.2 Coupled Mode Equations

Substituting into Eq. (A.34) and using the slow-envelope approximation, we obtain coupled equations for the spatial evolution of the two modes. Including the mean-field frequency shift from the driven mode, the equations in steady state become:

$$\left[\omega_1 - \tilde{\omega}(\boldsymbol{k}_1) + i\boldsymbol{v}_{\boldsymbol{k}_1} \cdot \nabla + i\Gamma(\boldsymbol{k}_1)\right] A_1(\boldsymbol{r}) = g_{12}^{00} A_0^2(\boldsymbol{r}) A_2^*(\boldsymbol{r}), \tag{A.49}$$

$$\left[\omega_2 - \tilde{\omega}(\boldsymbol{k}_2) - i\boldsymbol{v}_{\boldsymbol{k}_2} \cdot \nabla - i\Gamma(\boldsymbol{k}_2)\right] A_2^*(\boldsymbol{r}) = g_{12}^{00} [A_0^*(\boldsymbol{r})]^2 A_1(\boldsymbol{r}), \tag{A.50}$$

where the renormalized dispersion relation includes the mean-field shift:

$$\tilde{\omega}(\boldsymbol{k}) \approx \omega(\boldsymbol{k}) + 2g_{0k}^{0k} |A_0|^2. \tag{A.51}$$

The structure of Eqs. (A.49)–(A.50) is characteristic of parametric amplification: the gain of mode A_1 is proportional to A_2^*, and vice versa. This mutual coupling enables exponential growth when the parametric drive exceeds a threshold.

A.6.3 Spatial Growth Rate

For modes propagating along the y-direction, we seek solutions of the form:

$$A_1(y) = a_1 e^{\lambda y}, \qquad A_2(y) = a_2 e^{\lambda y}, \tag{A.52}$$

where λ is the spatial growth rate. Substituting into the coupled mode equations yields the matrix equation:

$$\begin{bmatrix} \omega_1 - \tilde{\omega}(\boldsymbol{k}_1) + iv^y_{\boldsymbol{k}_1}\lambda + i\Gamma(\boldsymbol{k}_1) & -g^{00}_{12}[A^*_0]^2 \\ -g^{00}_{12}A^2_0 & \omega_2 - \tilde{\omega}(\boldsymbol{k}_2) - iv^y_{\boldsymbol{k}_2}\lambda - i\Gamma(\boldsymbol{k}_2) \end{bmatrix} \begin{bmatrix} a_1 \\ a^*_2 \end{bmatrix} = 0. \tag{A.53}$$

For non-trivial solutions, the determinant must vanish. Defining the frequency-momentum mismatch parameters:

$$v^y_{\boldsymbol{k}_1} q_1 = \omega_1 - \tilde{\omega}(\boldsymbol{k}_1), \tag{A.54}$$

$$v^y_{\boldsymbol{k}_2} q_2 = \omega_2 - \tilde{\omega}(\boldsymbol{k}_2), \tag{A.55}$$

the solvability condition in the absence of damping gives:

$$\lambda = -\frac{i}{2}(q_1 - q_2) \pm \frac{1}{2}\sqrt{\frac{4|g^{00}_{12}A^2_0|^2}{v^y_{\boldsymbol{k}_1} v^y_{\boldsymbol{k}_2}} - (q_1 + q_2)^2}. \tag{A.56}$$

For the growth rate to be real (indicating true instability rather than oscillation), we require the expression under the square root to be positive. Setting $q_1 = q_2 = q$ for maximum growth, where:

$$q = \frac{\tilde{\omega}(\boldsymbol{k}_1) + \tilde{\omega}(\boldsymbol{k}_2) - 2\omega_0}{v^y_{\boldsymbol{k}_1} + v^y_{\boldsymbol{k}_2}}, \tag{A.57}$$

the growth rate simplifies to:

$$\lambda = \pm\sqrt{\frac{|g^{00}_{12}A^2_0|^2}{v^y_{\boldsymbol{k}_1} v^y_{\boldsymbol{k}_2}} - q^2}. \tag{A.58}$$

A.6.4 Selection Rules for Unstable Modes

Equation (A.58) reveals important constraints on which modes can become unstable:

1. **Group velocity sign constraint:** The product $v^y_{\boldsymbol{k}_1} v^y_{\boldsymbol{k}_2}$ must be positive for λ to be real. Since the Damon–Eshbach group velocity $v^y_{\boldsymbol{k}} = \mathrm{sgn}(k^y) v_{\mathrm{DE}}$, this requires both k^y_1 and k^y_2 to have the same sign. Combined with momentum conservation $k^y_1 + k^y_2 = 2k^y_0$, this restricts the allowed range to $0 \leq k^y_1 \leq 2k^y_0$ (assuming $k^y_0 > 0$).

2. **Boundary dominance:** The growth rate diverges as $v^y_{\boldsymbol{k}} \to 0$, which occurs at $k^y = 0$ or $k^y = 2k^y_0$. Consequently, the most unstable modes lie along these boundaries in momentum space, corresponding to one of the daughter magnons having near zero y-momentum.

3. **Energy conservation competition:** The detuning term q^2 penalizes modes that are off-shell. The most unstable mode balances the large growth from small group velocities against the cost of energy mismatch.

A.6.5 Cascade Hierarchy

Once the primary instability generates modes at $\boldsymbol{k}_1$ and $\boldsymbol{k}_2$, these can themselves act as "pump" modes for subsequent parametric processes. The cascade proceeds hierarchically: each scattering step feeds the next.

Since the most unstable modes have one daughter at $k^y = 0$ or $k^y = 2k^y_{\mathrm{in}}$, the cascade preferentially populates modes along specific lines in momentum space. For a drive at $\boldsymbol{k}_0$, the dominant cascade path places one daughter at $k^y = 0$ while the other carries all the y-momentum. Successive steps thus produce modes at $k^y = 2k^y_0, 3k^y_0, \ldots$, and we label each resonance by its

cascade order n (the same index used in Chapter 1), defined such that the order-n process involves the mode at $k^y = n\,k_0^y$. The primary instability corresponds to $n = 2$.

The NV center detects magnons resonant at ω_{NV}. The order-n cascade reaches the NV resonance when:

$$\omega\big(n\,\boldsymbol{k}_0\big) = \omega_{\mathrm{NV}}. \tag{A.59}$$

A.6.6 Mean-Field Frequency Shift and Resonance Condition

The mean-field shift Eq. (A.51) modifies the resonance condition. For the linearized Damon–Eshbach dispersion $\omega_{\boldsymbol{k}} = \Delta_0 + v_{\mathrm{DE}}|k^y|$, the renormalized dispersion becomes:

$$\tilde{\omega}_{\boldsymbol{k}} = \Delta_0 + 2\omega_{\mathrm{NL}} + v_{\mathrm{DE}}|k^y|, \tag{A.60}$$

where $\omega_{\mathrm{NL}} \approx g_{0k}^{0k} n_0 \propto |A_0|^2$ depends on the pump magnon density. Because the driven magnon amplitude scales linearly with the stripline current ($A_0 \propto I$; see Sec. A.7), the pump density is quadratic in the current, $n_0 = |A_0|^2 \propto I^2$, and the mean-field shift is therefore quadratic, $\omega_{\mathrm{NL}} \propto I^2$. This justifies the parameterization $\omega_{\mathrm{NL}} = \beta I^2$ used below.

For the order-n cascade to reach the NV resonance, the drive frequency must satisfy:

$$\omega_0(n, \omega_{\mathrm{NL}}) = \frac{\omega_{\mathrm{NV}} + (n-1)\Delta_0}{n} + \frac{2(n-1)}{n}\omega_{\mathrm{NL}}. \tag{A.61}$$

This equation predicts that the resonance frequencies shift with drive power (through ω_{NL}), providing a distinctive experimental signature of the cascaded scattering mechanism.

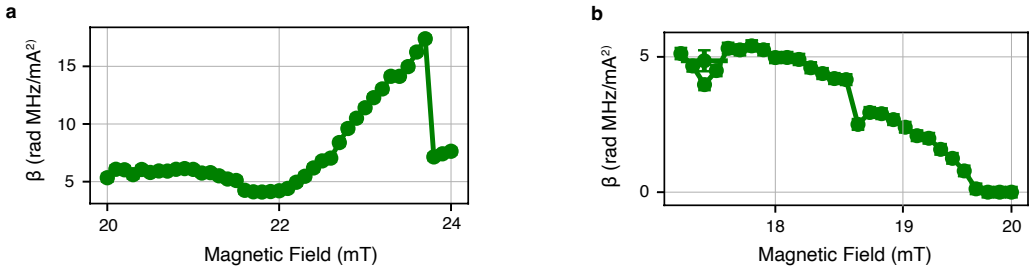


Figure A.2: **Mean-field frequency shifts of the cascade resonances.** Fitted parameters of the resonance condition Eq. (A.61), extracted from the power-dependent frequency shift of the cascade resonances. For each applied magnetic field H_{ext}, we plot the mean-field shift coefficient β (defined via $\omega_{\text{NL}} = \beta I^2$) together with the fitted cascade order n. (a) Results for the resonance shown in Fig. 1.6(C)(i). The fitted cascade order $n = 1.51(\pm 0.91)$ is consistent with $n = 2$. (b) Results for the resonance shown in Fig. 1.6(C)(ii). The fitted cascade order $n = 2.85(\pm 0.77)$ is consistent with $n = 3$.

A.6.7 Fitting the Cascade Resonances

To fit the observed resonances, we use Eq. (A.61) with $\omega_{\text{NL}} = \beta I^2$, where I is the stripline current and β is a fitting parameter that encodes the magnon-magnon interaction strength and the relation between current and magnon density. The cascade order n determines the slope of the power-dependent frequency shift, allowing us to identify which cascade order produces each observed resonance. The predicted resonance structure, discrete peaks that shift with power according to their cascade order, matches the experimental observations and confirms the cascaded parametric scattering mechanism. The fitted mean-field coefficient β and cascade order n for each resonance are shown in Fig. A.2.

A.6.8 Numerical Prediction of the Resonance Map

The analytical results derived above including the parametric growth rate (Eq. (A.58)), the cascade hierarchy, and the resonance condition (Eq. (A.61)) predict that specific drive frequencies

ω_0 will produce magnons at the NV resonance ω_{NV} for each applied field H_{ext}. To obtain a quantitative prediction of the full resonance structure shown in Fig. 1.6, we numerically evaluate the cascaded growth rate and its overlap with the NV momentum filter across a two-dimensional grid of $(H_{\mathrm{ext}}, \omega_0)$ values. The bright ridges in the resulting color map trace out a resonance structure, identifying the drive frequencies at which parametric scattering most efficiently channels magnon population into the NV detection window.

A.6.8.1 Drive momentum and field-dependent parameters

The calculation sweeps over magnetic fields $\mu_0 H_{\mathrm{ext}} \in [17, 24]\,\mathrm{mT}$ and drive frequencies $\omega_0/(2\pi) \in [1.75, 2.10]\,\mathrm{GHz}$. For each H_{ext}, we compute the equilibrium magnetization angle θ_0 and the full dispersion relation. The NV resonance frequency is

$$\omega_{\mathrm{NV}}(H_{\mathrm{ext}}) = 2\pi \times 2.87\,\mathrm{GHz} - \gamma H_{\mathrm{ext}}\,. \tag{A.62}$$

For each drive frequency ω_0, the corresponding drive momentum $\boldsymbol{k}_0 = (0, k_0^y)$ is found by numerically inverting the one-dimensional Damon–Eshbach dispersion relation along k_y: we find k_0^y such that $\omega(0, k_0^y) = \omega_0$. The constraint $k_0^x = 0$ follows from the stripline injection profile derived in Sec. A.3, which confines excitation to the $k_x = 0$ subspace. When the mean-field shift is included, the inversion uses the renormalized dispersion $\tilde{\omega}(\boldsymbol{k}) = \omega(\boldsymbol{k}) + 2\omega_{\mathrm{NL}}$.

A.6.8.2 Growth rate on the two-dimensional momentum grid

At each $(H_{\mathrm{ext}}, \omega_0)$ point, the parametric growth rate from Eq. (A.58) is evaluated over a two-dimensional momentum grid spanning $k_x \in [-40, 40]\,\mu\mathrm{m}^{-1}$ and $k_y \in [-0.1, 4]\,\mu\mathrm{m}^{-1}$ with

$10^3 \times 10^3$ points. Each grid point represents a candidate daughter momentum $\boldsymbol{k}_3$; the partner is fixed by momentum conservation, $\boldsymbol{k}_4 = \boldsymbol{k}_1 + \boldsymbol{k}_2 - \boldsymbol{k}_3$, where $\boldsymbol{k}_1$ and $\boldsymbol{k}_2$ are the two input momenta for the scattering process. The growth rate is

$$\lambda(\boldsymbol{k}_3) = \begin{cases} \sqrt{\dfrac{|g_{34}^{12}\, A_1\, A_2|^2}{v^y_{\boldsymbol{k}_3}\, v^y_{\boldsymbol{k}_4}} - q^2} & \text{if the argument is positive}\,, \\ 0 & \text{otherwise}\,, \end{cases} \tag{A.63}$$

where the energy–momentum mismatch is

$$q = \frac{\tilde{\omega}(\boldsymbol{k}_3) + \tilde{\omega}(\boldsymbol{k}_4) - \omega_{\boldsymbol{k}_1} - \omega_{\boldsymbol{k}_2}}{v^y_{\boldsymbol{k}_3} + v^y_{\boldsymbol{k}_4}}\,, \tag{A.64}$$

and A_1, A_2 and $\omega_{\boldsymbol{k}_1}$, $\omega_{\boldsymbol{k}_2}$ are the amplitudes and frequencies of the two incoming modes. The group velocities are evaluated using the exact numerical derivative $v^y_{\boldsymbol{k}} = \mathrm{sgn}(k^y)\, \partial\omega/\partial k$ to properly account for the flattening of the dispersion curve. The bare four-magnon interaction strength is taken to be momentum-independent and normalized by the effective macroscopic spin density s_{eff}:

$$g \approx -\frac{\gamma M_s}{2 s_{\mathrm{eff}}}\,, \tag{A.65}$$

corresponding to the dominant dipolar contribution to the T-matrix and evaluates to $g/(2\pi) \approx -0.3$ Hz μm^3. This simplification replaces the full momentum-dependent vertex g_{34}^{12} in Eq. (A.63) with the single value g. Using the full momentum-dependent vertex shifts the position of the maximum only marginally, since the group-velocity enhancement and off-shell penalty provide the dominant momentum dependence.

A.6.8.3 Cascade through four scattering steps

The cascade is computed iteratively: the most unstable output momenta from each step serve as inputs for the next. The branching structure proceeds as follows:

1. **Step 1** (order $n = 2$): Two pump magnons scatter, $\boldsymbol{k}_0 + \boldsymbol{k}_0 \to \boldsymbol{k}_1 + \boldsymbol{k}_2$. This produces one growth rate map and identifies the most unstable pair $(\boldsymbol{k}_1^{\max}, \boldsymbol{k}_2^{\max})$.

2. **Step 2** (order $n = 3$): The pump scatters with each first-step daughter, $\boldsymbol{k}_0 + \boldsymbol{k}_1^{\max} \to \boldsymbol{k}_3 + \boldsymbol{k}_4$ and $\boldsymbol{k}_0 + \boldsymbol{k}_2^{\max} \to \boldsymbol{k}_3' + \boldsymbol{k}_4'$, producing 2 growth rate maps.

3. **Step 3** (order $n = 4$): Four standard branches arise from the pump scattering with each second-step output. Two additional branches exploit the dispersion relation symmetry under $k_x \to -k_x$: the first-step daughter $\boldsymbol{k}_1^{\max}$ scatters with its mirror image $\boldsymbol{k}_{1,\mathrm{mirror}} = (-k_{1x}^{\max},\, k_{1y}^{\max})$, and similarly for $\boldsymbol{k}_2^{\max}$. This yields 6 branches total.

4. **Step 4** (order $n = 5$): Each of the 12 output momenta from step 3 scatters with the pump, producing 12 branches.

At each generation, we retain only the momentum that maximizes the growth rate on each parent branch. Because the higher-order mode populations are not independently known, all input modes are assigned the same momentum-independent reference amplitude, $A_{\mathrm{ref}} = \sqrt{n_0}$. This choice does not shift the momentum maximizing $\lambda(\boldsymbol{k})$ over the parameter range considered. The calculation therefore predicts the resonance positions and branching structure, not their spectral weights.

A.6.8.4 Overlap with the NV detection window

For each cascade order and branch, the predicted NV signal strength is computed as the overlap between the growth rate map and the NV-detectable region of momentum space. First, the NV-resonant momenta are identified as the set of wavevectors $\boldsymbol{k}$ on the 2D grid satisfying $|\omega(\boldsymbol{k}) - \omega_{\mathrm{NV}}| < \delta\omega$, forming an iso-energy contour in the (k_x, k_y) plane. Each point on this contour is then weighted by the NV momentum filter function $\tilde{\mathcal{D}}_{\boldsymbol{q}}^{\downarrow,+-}$ from Eq. (A.23), which encodes the dipolar coupling strength between magnons at wavevector $\boldsymbol{q}$ and the NV center. The filter captures the essential physics: the exponential suppression $e^{-2qz_{\mathrm{NV}}}$ of coupling to large wavevectors, and the angular selection rules set by the NV and magnetization orientations.

The overlap for a given branch at order n is

$$\mathcal{O}_n(H_{\mathrm{ext}}, \omega_0) = \sum_{\boldsymbol{k} \in \text{ NV contour}} \lambda^{(n)}(\boldsymbol{k})\, \hat{\mathcal{D}}(\boldsymbol{k})\,, \tag{A.66}$$

where $\hat{\mathcal{D}}(\boldsymbol{k})$ denotes the normalized and thresholded momentum filter. This scalar value quantifies the efficiency with which the order-n cascade delivers parametrically amplified magnons into the NV detection window at the given $(H_{\mathrm{ext}}, \omega_0)$ operating point.

A.6.8.5 Assembly and comparison with experiment

The overlap values $\mathcal{O}_n(H_{\mathrm{ext}}, \omega_0)$ are computed across the full parameter space, and the contributions from all branches within each order are summed. The resulting four two-dimensional maps, one per cascade order, constitute the resonance diagram. The bright ridges, where $\mathcal{O}_n$ is maximal, predict the drive frequencies at which the order-n cascade produces magnons at ω_{NV}.

Two cases are considered for comparison with experiment: for the lower cascade orders ($n = 2, 3$), the mean-field shift is set to zero ($\omega_{\mathrm{NL}} = 0$), appropriate for moderate pump densities where the power-dependent dispersion correction is small. For the higher orders ($n = 4, 5$), where the driven magnon density is large enough to appreciably shift the dispersion relation, a finite mean-field correction $\omega_{\mathrm{NL}} = g\, n_0$ is included. The predicted resonance map is compared with the experimental observations in Fig. 1.6, where the predicted tongue maxima align with the experimentally measured resonance frequencies across the full range of magnetic fields.

A.7 Power Calibration

A.7.1 Stripline Current Calibration

Throughout this work, the microwave stripline current I enters the theory as the source of the magnetic field that drives magnons in the YIG film. In particular, the injection amplitude $S_0 \propto I$ derived in Sec. A.3 sets the driven magnon population, and the pump amplitude $|A_0|^2 \propto I^2$ determines the parametric gain in Sec. A.6. Here we describe how I is determined from an experimentally accessible quantity: the microwave power measured at the output of the circuit.

A.7.1.1 Microwave circuit and measurement

As described in Chapter 1, the microwave circuit consists of a signal generator (50 Ω output impedance), connected via coaxial cables and a PCB trace to the gold stripline antenna on the YIG chip. One end of the stripline is wire bonded to the PCB; the other end is wire bonded back to a second PCB trace, which is connected to a 50 Ω termination, which is a Signal Hound spectrum

analyzer. Both terminations present a 50 Ω load. The spectrum analyzer records the transmitted power P_{SA} in dBm, from which the current at the output port is obtained as

$$I_{\mathrm{SA}} = \sqrt{\frac{2P_{\mathrm{SA}}}{Z_0}}\,, \qquad Z_0 = 50\ \Omega\,. \tag{A.67}$$

This is the current flowing through the input impedance of the spectrum analyzer. We now argue that I_{SA} is a faithful measure of the stripline current I.

A.7.1.2 Lumped-element argument

The gold stripline has a length of approximately 400 μm. At the operating frequencies of 1.5–3 GHz, the electromagnetic wavelength is on the order of centimeters, exceeding the stripline length by two orders of magnitude. The stripline is therefore electrically short and acts as a lumped series element (predominantly a small inductance). The same applies to the wire bonds, which contribute a small series inductance.

In this lumped-element limit, the entire path from one PCB pad through the wire bond, stripline, and second wire bond to the opposite PCB pad is a series network. In a series circuit, the current is the same at every point. The current flowing through the stripline is therefore equal to the current flowing into the 50 Ω termination:

$$I_{\mathrm{strip}} \approx I_{\mathrm{SA}}\,. \tag{A.68}$$

To verify this picture, we measure the forward transmission coefficient $|S_{21}|^2$ of the full circuit (from signal generator output to spectrum analyzer input) as a function of frequency across

the experimental bandwidth. The transmission is found to be approximately flat, with no significant resonant features.

A.7.2 Calculating the Pump and Signal Magnon Amplitudes

The fitting procedure described in Sec. A.5 requires knowledge of the pump and signal magnon population densities $\langle \tilde{n}_p \rangle$ and $\langle \tilde{n}_s \rangle$ at the stripline. These cannot be measured directly from the NV Rabi signal, as the pump and signal are far off-resonance with the NV transition, but can be inferred from single-tone Rabi measurements on resonance with the NV transition ($\omega_{\mathrm{NV}} = \omega_{\mathrm{drive}}$) combined with the stripline current calibration described above.

A.7.2.1 Reference calibration from single-tone Rabi measurements

In a single-tone experiment, the stripline drives magnons at a single frequency ω_d with current I. At the applied bias field, the NV resonance condition $\omega_{\mathrm{NV}} = \Delta - \gamma H^z$ selects a magnon wavevector k_{NV} via the dispersion relation. These magnons propagate away from the stripline, and the NV center detects the resulting stray field as a Rabi frequency Ω_R.

Using the macroscopic mapping equations derived in Sec. A.3 and the NV–YIG separation z_{NV} from the height map (Sec. A.4), we convert the measured Rabi frequency directly to a local magnon population density $\langle \tilde{n}_{\mathrm{NV}} \rangle$. This provides a reference calibration point: at current I_{ref} and the reference wavevector $k_{\mathrm{ref}} \equiv k_{\mathrm{NV}}$ of this measurement, we obtain a measured population density $\langle \tilde{n}_{\mathrm{ref}} \rangle$.

A.7.2.2 Pump and signal population densities

We calculate the current → magnon transduction directly as follows. Sweeping the bias field tunes the NV-resonant wavevector k_{NV} through the dispersion relation, and the per-current Rabi response defines the normalized transduction

$$R(k) \equiv \frac{\Omega_R(k)/I}{\Omega_R(k_{\mathrm{ref}})/I_{\mathrm{ref}}}\,, \tag{A.69}$$

i.e., the relative current → magnon conversion efficiency at wavevector k, normalized to the reference measurement $\langle\tilde{n}_{\mathrm{ref}}\rangle$ above. We fit the experimentally-determined $R(k)$ to an exponentially decaying envelope, which we evaluate at the pump and signal wavevectors below. We can approximate $R(k) \approx \tilde{S}(k)/\tilde{S}(k_{\mathrm{ref}})$, with $\tilde{S}(k) = h(kH)w(kW)$ being the injection profile of Sec. A.3.

For the two-tone experiment, the pump (frequency ω_p, current I_p) and signal (frequency ω_s, current I_s) excite modes at wavevectors k_p and k_s. Since the magnon amplitude scales linearly with current and the density is quadratic in the amplitude, $\langle\tilde{n}\rangle = |A|^2$, the local densities at the NV location are

$$\langle\tilde{n}_p(y_{\mathrm{NV}})\rangle = \langle\tilde{n}_{\mathrm{ref}}\rangle \left(\frac{I_p}{I_{\mathrm{ref}}}\right)^2 R(k_p)^2\,, \tag{A.70}$$

$$\langle\tilde{n}_s(y_{\mathrm{NV}})\rangle = \langle\tilde{n}_{\mathrm{ref}}\rangle \left(\frac{I_s}{I_{\mathrm{ref}}}\right)^2 R(k_s)^2\,. \tag{A.71}$$

Because the scattering equations of Sec. A.5 are integrated forward from the stripline at $y = 0$, these boundary amplitudes are back-propagated from the NV location y_{NV} to the source through

their spatial decay lengths $\lambda = \Gamma / v_g$:

$$|A_p(0)|^2 = \langle \tilde{n}_p(y_{\mathrm{NV}}) \rangle \, e^{2\lambda_p y_{\mathrm{NV}}} \, , \tag{A.72}$$

$$|A_s(0)|^2 = \langle \tilde{n}_s(y_{\mathrm{NV}}) \rangle \, e^{2\lambda_s y_{\mathrm{NV}}} \, . \tag{A.73}$$

This ensures the parametric gain equations use the true magnon intensities at the stripline interaction boundary.

Appendix B: Supplementary Information: A Nanoscale Magnetic Spectrum Analyzer Based on Qubit Dressed States

B.1 Theoretical framework

B.1.1 AC Stark shift and three-level dressed state picture

For a two-level system, the Hamiltonian $\hat{H}$ can be written as:

$$\hat{H} = h\,\gamma B_0 \hat{S}_z + h\,\gamma B_{\text{probe}} \cos\left(2\pi f_{\text{probe}} t + \phi\right) \hat{S}_x. \tag{B.1}$$

Let the eigenstates of $\hat{S}_z$ be $|0\rangle, |+1\rangle$; Eq. B.1 can then be expressed as:

$$\hat{H} = \frac{h\,\gamma}{2} \begin{pmatrix} 0 & B_{\text{probe}} \cos(2\pi f_{\text{probe}} t + \phi) \\ B_{\text{probe}} \cos(2\pi f_{\text{probe}} t + \phi) & 2B_0 \end{pmatrix}. \tag{B.2}$$

The state Ψ of the system evolves in time according to the Schrödinger equation:

$$i\,h \frac{d\Psi}{dt} = 2\pi\,\hat{H}\,\Psi. \tag{B.3}$$

When we apply a unitary transformation $\hat{U}$ to Ψ and transfer it to the rotating frame, with $\tilde{\Psi} = \hat{U}\Psi$, the transformed state $\tilde{\Psi}$ evolves according to the following effective Hamiltonian $\hat{H}'$:

$$\hat{H}' \;=\; \hat{U}\hat{H}\hat{U}^{\dagger} + i\,\frac{h}{2\pi}\,(\partial_t \hat{U})\,\hat{U}^{\dagger}, \tag{B.4}$$

where

$$\hat{U} \;=\; \exp\Big(i\,2\pi f_{\text{probe}}\,t\,|+1\rangle\langle+1|\Big). \tag{B.5}$$

Using the rotating-wave approximation (RWA), $\hat{H}'$ can be written as:

$$\hat{H}' \;=\; h\begin{pmatrix} 0 & \dfrac{\Omega}{2}\,e^{i\phi} \\ \dfrac{\Omega}{2}\,e^{-i\phi} & \Delta \end{pmatrix}, \tag{B.6}$$

where

$$\Delta \;=\; f_{\text{res}} - f_{\text{probe}}, \qquad f_{\text{res}} = \gamma B_0, \qquad \Omega = \gamma B_{\text{probe}}\,c \;=\; \frac{1}{T_{\text{Rabi osc.}}}. \tag{B.7}$$

Here c is the matrix element $|\langle 0|\,\hat{S}_x/\hbar\,|1\rangle|$, which is $1/2$ for a spin $1/2$ system. The eigenenergies $E_{\pm}$ of this effective Hamiltonian are then:

$$E_{\pm} \;=\; \frac{h}{2}\,(\Delta \pm \sqrt{\Delta^2 + \Omega^2}), \tag{B.8}$$

so that the energy splitting in the high detuning limit is given by:

$$E_+ - E_- \;=\; h\sqrt{\Delta^2+\Omega^2} \;\approx\; h\left(\Delta + \frac{\Omega^2}{2\Delta}\right) \quad (\Delta \gg \Omega), \tag{B.9}$$

and the change in the splitting due to the probe field is therefore:

$$\delta E \;=\; (E_+ - E_-) - h\Delta \;=\; h\,\frac{\Omega^2}{2\Delta}. \tag{B.10}$$

B.1.1.1 Three level model

The NV has an electronic spin $S = 1$ system with basis $\{|0\rangle, |+1\rangle, |-1\rangle\}$. In the rotating frame at f_{probe} and within the RWA, the effective Hamiltonian reads:

$$\hat{H}' \;=\; h\begin{pmatrix} 0 & \frac{\Omega}{2}\,e^{+i\phi_+} & \frac{\Omega}{2}\,e^{+i\phi_-} \\ \frac{\Omega}{2}\,e^{-i\phi_+} & \Delta_+ & 0 \\ \frac{\Omega}{2}\,e^{-i\phi_-} & 0 & \Delta_- \end{pmatrix}, \tag{B.11}$$

where the detunings and Rabi rates are simply

$$\Delta_+ = f_{0\to+1} - f_{\text{probe}}, \qquad \Delta_- = f_{0\to-1} - f_{\text{probe}}, \qquad \Omega = \gamma B_{\text{probe}}\, c \;=\; \frac{1}{T_{\text{Rabi osc.}}}. \tag{B.12}$$

The matrix element $|\langle 0|\,\hat{S}_x/\hbar\,|\pm 1\rangle|$ is now $c = 1/\sqrt{2}$ for both NV spin transitions.

The eigenvalues in the high detuning regime are in this case:

$$E_0 \approx -\,h\left(\frac{\Omega^2}{4\,\Delta_+} + \frac{\Omega^2}{4\,\Delta_-}\right), E_+ \approx h\left(\Delta_+ + \frac{\Omega^2}{4\,\Delta_+}\right), E_- \approx h\left(\Delta_- + \frac{\Omega^2}{4\,\Delta_-}\right). \tag{B.13}$$

As we are interested in the change in energy between only one transition ($0 \rightarrow +1$ in the present experiments), the relevant energy shift is therefore:

$$\delta E = (E_+ - E_0) - h\Delta_+ = h(\frac{\Omega^2}{2\Delta_+} + \frac{\Omega^2}{4\Delta_-}) = h\frac{\Omega^2}{2\tilde{\Delta}^2} \tag{B.14}$$

When the probe field is above the $0 \rightarrow +1$ transition it is possible to write $\Delta_- = \epsilon + \Delta_+$ where ϵ is the NV Zeeman splitting due to the external magnetic bias field.

As our model is meant to be useful over a broad range of frequencies, we also account for the situation where we can no longer assume $\Delta \ll f_{\text{probe}}, f_{0\rightarrow+1}$ and hence we can no longer assume the RWA. We follow the appendix calculation of [7], where the Schrieffer-Wolff formalism is used. From there we get:

$$\widetilde{\hat{H}}_{\text{eff}} = \hat{H}_0 + h \begin{pmatrix} A & 0 & 0 \\ 0 & B-A & 0 \\ 0 & 0 & -B \end{pmatrix}, \tag{B.15}$$

$$A = \frac{\Omega^2 f_{0\rightarrow+1}}{2(f_{0\rightarrow+1} - f_{\text{probe}})(f_{0\rightarrow+1} + f_{\text{probe}})}, \quad B = \frac{-\Omega^2 f_{0\rightarrow-1}}{2(f_{0\rightarrow-1} - f_{\text{probe}})(f_{0\rightarrow-1} + f_{\text{probe}})}. \tag{B.16}$$

where the difference from [7] is due to our definition of the Rabi rate to include the matrix element.

We note that in the limit of the RWA ($\Delta \ll f_{\text{probe}}, f_{0\rightarrow+1}$) we can write $f_{0\rightarrow\pm1} + f_{\text{probe}} \approx 2f_{0\rightarrow\pm1}$ and recover the result of Eq. B.14. As visible in Fig. B.1, the deviation between the full model and the simple 2 level approach is not substantial especially in the high detuning regime.

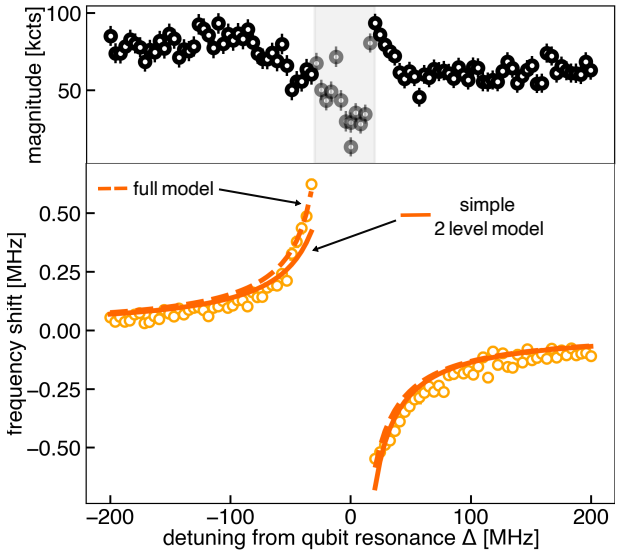


Figure B.1: Magnitude Λ and frequency shift with respect to the detuning of the probe field. Close to resonance the magnitude decreases due to a resonant drive. The full and the simple model are fitted to the frequency shift.

The phase data close to the resonance is not considered as the system begins to be driven on resonance (seen by the clear decrease in magnitude in the upper panel).

B.1.2 Qubit dressed state spectrum analyzer

The functionality of the qubit dressed state spectrum analyzer arises from four key physical effects or points:

1. Applying an off resonant MW field to a two (or three) level system changes the energy difference of the eigenstates by $\delta E \approx \frac{\Omega^2}{2\Delta}$.

2. A relative shift in qubit eigenenergies leads to phase accumulation over time if the qubit is in a superposition state.

3. Decoherence of a qubit follows the variance of the phase via $\Lambda(T) = \exp\left(-\frac{1}{2}\langle\phi^2(T)\rangle\right)$. [70]

4. A non linear mixing element, including the response of the qubit to RF fields arising from the AC Stark shift enables downconversion of a noise spectrum by an arbitrary LO frequency.

To connect these points, we introduce a situation in which the qubit experiences not only the coherent probe field but also an additional noisy signal field. In the rotating frame, these contributions add, such that the qubit evolves under an effective Rabi frequency

$$\Omega_{\text{eff}}(t) = \Omega_{\text{probe}}(t) + \Omega_{\text{s}}(t). \tag{B.17}$$

Using **point 1**, the corresponding drive-induced shift of the dressed-state splitting relative to the bare states is

$$\begin{aligned} \delta E(t)/h &= \frac{\Omega_{\text{eff}}^2(t)}{2\Delta} = \frac{1}{2\Delta}\Big(\Omega_{\text{probe}}^2(t) + \Omega_{\text{s}}^2(t) + 2\,\Omega_{\text{probe}}(t)\Omega_{\text{s}}(t)\Big) \\ &\approx \frac{1}{2\Delta}\Big(\Omega_{\text{probe}}^2(t) + 2\,\Omega_{\text{probe}}(t)\Omega_{\text{s}}(t)\Big) \\ &= \frac{\gamma^2}{2c^2\Delta}\Big(B_{\text{probe}}^2\cos^2(2\pi f_{\text{probe}}t) + 2B_{\text{probe}}\cos(2\pi f_{\text{probe}}t)\,B_{\text{s}}(t)\Big), \end{aligned} \tag{B.18}$$

where we neglect the term quadratic in the signal field, $\Omega_{\text{s}}^2(t) \propto B_{\text{s}}^2(t)$ as it is typically small and far off resonance.

From **point 2** we can derive the expected phase for one instance of the measurement through $h\phi = \int_0^\tau \delta E$. As we will average over thousands of individual experiments, this phase will not be deterministic over all experiments. We can define the variance of the accumulated phase due to the "noisy" AC Stark effect in analogy to [70] :

$$h^2\langle\phi^2(\tau)\rangle = \int_0^\tau dt_1 \int_0^\tau dt_2 \langle\delta E(t_1)\delta E(t_2)\rangle. \tag{B.19}$$

This is where **point 3** becomes crucial as the qubit's phase variance can be determined by measuring the magnitude Λ (Eq. 2.4). In order to calculate this variance we can start by dropping the deterministic, noiseless part of Eq. B.18, $\delta E(t)_{\text{det}}/h = \frac{\gamma^2}{2c^2\Delta} B^2_{\text{probe}} \cos^2(2\pi f_{\text{probe}} t)$, as it will not contribute to the variance. We are thus left with the *crossterm* dependent on a multiplication of probe field and the signal field:

$$\delta E_{\text{mix}}/h = \frac{\gamma^2}{c^2\Delta} B_{\text{p}} \cos(2\pi f_{\text{probe}} t) B_{\text{s}}(t). \tag{B.20}$$

The result enables the use of **point 4**. Multiplication of the noise signal and the coherent probe field, arising from the quadratic dependency of the AC Stark shift on the effective magnetic field, effectively shifts upward the measurable frequency range of a qubit dynamical decoupling (DD) measurement sequence, enabling detection of the signal spectra.

The calculation starts by introducing the scaling prefactor $\alpha \equiv \left(\frac{\gamma^2 B_{\text{probe}}}{c^2\Delta}\right)^2$. For an idealized two-level system, Δ is simply the probe detuning. For the NV center, a three-level treatment leads to the effective replacement $\frac{1}{\Delta} \rightarrow \frac{1}{\Delta_+} + \frac{1}{2\Delta_-}$, together with the corresponding choice $c = \sqrt{1/2}$, as discussed in Appendix B.1.1.1.

We next calculate the argument of the integral in Eq. B.19:

$$\begin{aligned} \langle \delta E(t_1) \delta E(t_2) \rangle / \alpha &= \cos(2\pi f_{\text{probe}} t_1) \cos(2\pi f_{\text{probe}} t_2) \langle B_s(t_1) B_s(t_2) \rangle & \text{(B.21)} \\ &= \cos(2\pi f_{\text{probe}} t_1) \cos(2\pi f_{\text{probe}} t_2) \int_{-\infty}^{\infty} df\, e^{-i2\pi f(t_2 - t_1)}\, S_s(f). & \text{(B.22)} \end{aligned}$$

Using $\cos x \cos y = \frac{1}{2}[\cos(x-y) + \cos(x+y)]$ with $x = 2\pi f_{\text{probe}} t_1$ and $y = 2\pi f_{\text{probe}} t_2$ yields:

$$\langle \delta E(t_1) \delta E(t_2) \rangle / \alpha = \frac{1}{2} \Big[\cos\big(2\pi f_{\text{probe}}(t_2 - t_1)\big) + \cos\big(2\pi f_{\text{probe}}(t_2 + t_1)\big) \Big] \int_{-\infty}^{\infty} df \, e^{-i2\pi f(t_2 - t_1)} \, S_s(f). \tag{B.23}$$

To justify neglecting the second term, it is convenient to switch to sum- and difference-time coordinates:

$$u = \frac{t_1 + t_2}{2}, \qquad v = t_2 - t_1, \tag{B.24}$$

for which $dt_1 \, dt_2 = du \, dv$ and the square $(t_1, t_2) \in [0, \tau]^2$ maps to $v \in [-\tau, \tau]$ and $u \in [|v|/2, \ \tau - |v|/2]$. In these variables:

$$\cos\big(2\pi f_{\text{probe}}(t_2 - t_1)\big) = \cos(2\pi f_{\text{probe}} v), \qquad \cos\big(2\pi f_{\text{probe}}(t_2 + t_1)\big) = \cos(4\pi f_{\text{probe}} u). \tag{B.25}$$

Since the correlator depends only on the time difference v, the sum-time contribution oscillates rapidly in u and is therefore suppressed in the double integral:

$$\left| \int_{|v|/2}^{\tau - |v|/2} du \, \cos(4\pi f_{\text{probe}} u) \right| = \left| \frac{\sin(4\pi f_{\text{probe}} u)}{4\pi f_{\text{probe}}} \Big|_{|v|/2}^{\tau - |v|/2} \right| \leq \frac{1}{2\pi f_{\text{probe}}} \ll \tau \qquad (f_{\text{probe}} \tau \gg 1). \tag{B.26}$$

Consequently, the term $\cos\big(2\pi f_{\text{probe}}(t_2 + t_1)\big)$ is referred to as fast-rotating and can be neglected compared to the surviving term, whose u-integration scales as $\int du \sim \tau$.

Keeping only the difference-time term results in:

$$\langle \delta E(t_1) \delta E(t_2) \rangle / \alpha \ \simeq \ \frac{1}{2} \cos\big(2\pi f_{\text{probe}}(t_2 - t_1)\big) \int_{-\infty}^{\infty} df \, e^{-i2\pi f(t_2 - t_1)} \, S_s(f). \tag{B.27}$$

Now the "mixer" identity from **point 4** can be used:

$$2\cos\big(2\pi f_{\text{probe}}(t_2-t_1)\big)e^{-i2\pi f(t_2-t_1)} = e^{-i2\pi(f+f_{\text{probe}})(t_2-t_1)} + e^{-i2\pi(f-f_{\text{probe}})(t_2-t_1)}, \tag{B.28}$$

and the argument can be rewritten as

$$\langle \delta E(t_1)\delta E(t_2)\rangle/\alpha \;\simeq\; \frac{1}{4}\int_{-\infty}^{\infty} df\,\left(e^{-i2\pi(f+f_{\text{probe}})(t_2-t_1)} + e^{-i2\pi(f-f_{\text{probe}})(t_2-t_1)}\right) S_s(f). \tag{B.29}$$

Inserting this back into Eq. B.19 to obtain the variance of the phase:

$$\begin{aligned}\langle\phi^2\rangle &= \frac{\alpha}{4}\int_0^\tau dt_1\int_0^\tau dt_2\int_{-\infty}^{\infty} df\,\left(e^{-i2\pi(f+f_{\text{probe}})(t_2-t_1)} + e^{-i2\pi(f-f_{\text{probe}})(t_2-t_1)}\right) S_s(f) &\text{(B.30)}\\ &= \frac{\alpha}{4}\int_{-\infty}^{\infty} df\, S_s(f)\left(\Big|\int_0^\tau e^{i2\pi(f-f_{\text{probe}})t}\,dt\Big|^2 + \Big|\int_0^\tau e^{i2\pi(f+f_{\text{probe}})t}\,dt\Big|^2\right). &\text{(B.31)}\end{aligned}$$

where we used that the only time dependence is in the exponentials,
$\big(\int_0^\tau e^{+i\theta t_1}dt_1\big)\big(\int_0^\tau e^{-i\theta t_2}dt_2\big) = \big|\int_0^\tau e^{i\theta t}dt\big|^2$.

As a last step we can now identify the scaled frequency filter function

$$W_\tau(\theta) = \frac{\alpha}{2}\Big|\int_0^\tau e^{i\theta t}\,dt\Big|^2 \tag{B.32}$$

and state:

$$\langle\phi^2\rangle(f_{\mathrm{p}}) = \frac{1}{2}\int_{-\infty}^{\infty} df\, S_s(f)\left[W_\tau(f - f_{\text{probe}}) + W_\tau(f + f_{\text{probe}})\right] \tag{B.33}$$

$$= \int_{-\infty}^{\infty} df\, S_s(f) W_\tau(f + f_{\text{probe}}) \tag{B.34}$$

$$= (S_s * W_\tau)(f_{\text{probe}}) \tag{B.35}$$

Here, it is assumed in the second equal sign that the noise is real and wide-sense stationary, which effectively means that it is symmetric $S(f) = S(-f)$.

Equation B.35 is the central result of this theoretical framework, as it captures the effective spectrum analyzer response in a compact form. The AC-Stark *crossterm* acts as a frequency translator: by tuning the probe field frequency f_{probe}, the same intrinsic filter function W_τ is shifted along the frequency axis and therefore samples different parts of the noise spectrum. In other words, the measured phase variance $\langle\phi^2\rangle(f_{\text{probe}})$ is given by the convolution of the signal power spectral density $S_s(f)$ with a probe-frequency–shifted filter function. Mathematically this is equivalent to a down conversion of the noise.

Fig. B.2 visualizes this result using the (rescaled) spin echo filter function:

$$W_\tau(f)_{\text{spin echo}} = \frac{1}{2}\left(\frac{B_{\text{probe}}\gamma^2}{c^2\Delta}\right)^2 \frac{16}{(2\pi f)^2}\,\sin^4\left(\frac{\pi f\tau}{2}\right). \tag{B.36}$$

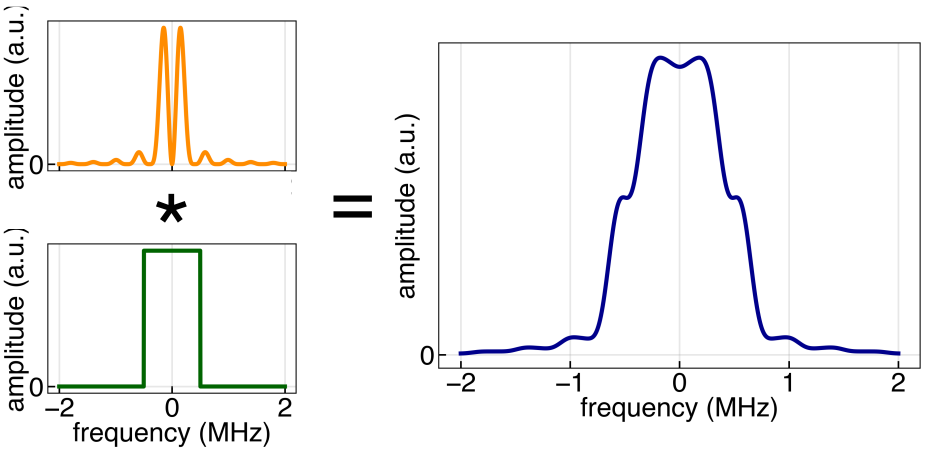


Figure B.2: Visualization of the convolution of a spin echo filter function $W_{\tau=4000\text{ns}}(f)$ (orange) and a perfectly rectangular noise power spectral density $S_s(f)$ (green). The result is directly proportional to the probe frequency dependent phase variance $\langle\phi^2\rangle(f_\text{p})$ (blue).

B.1.3 Scaling for broadband noise

When the noise width of $\mathcal{S}_s(\omega)$ is much larger than the width of the filter function $W_\tau(\theta)$ ($\approx 1/\tau$) analysis of Eq. B.35 is straight-forward. In this case we can assume that the noise distribution is an effective constant $\mathcal{S}_s(f) = \mathcal{S}_s$ and calculate:

$$\langle\phi^2\rangle = \frac{S_s}{2}\left(\frac{B_\text{probe}\gamma^2}{c^2\Delta}\right)^2 \int_{-\infty}^{\infty} df\, \frac{16}{(2\pi f)^2}\sin^4\frac{\pi f\tau}{2} = \frac{S_s}{2}\left(\frac{B_\text{probe}\gamma^2}{c^2\Delta}\right)^2 \tau \tag{B.37}$$

$$= \beta\frac{B_\text{probe}^2\cdot\tau}{\Delta^2} \quad \text{where} \quad \beta = 8S_s\,\gamma^4, \tag{B.38}$$

given that $c = \sqrt{1/2}$ for a three level system.

When comparing this result to a conventional DD measurement of qubit decoherence, we observe an effective scaling with $\propto (\frac{\Omega_p}{\Delta})^2$, directly following from the rescaled filter function $W_\tau(f)$.

B.2 Characterization results

B.2.1 Spectra

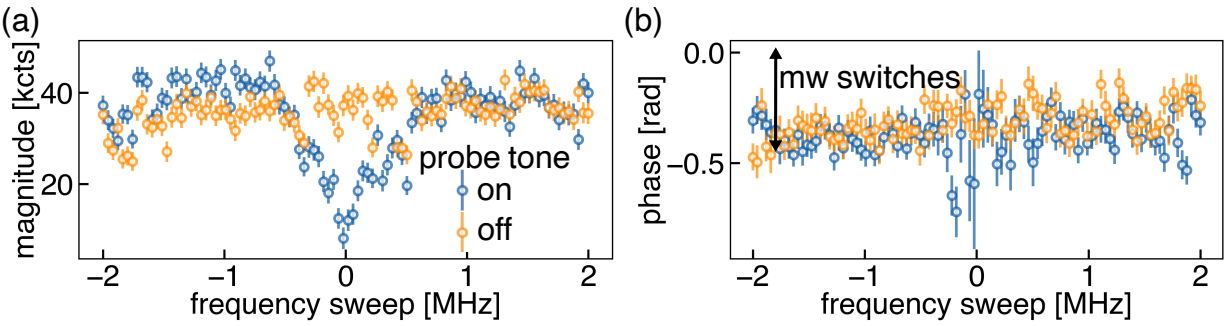


Figure B.3: Dressed state spin echo and reference spin echo measurements for the probe field on and off, with application of a Lorentzian noise signal. Data is expressed in terms of the unnormalized NV ensemble spin (a) magnitude Λ and (b) phase ϕ. For the dressed state spin echo measurement, mixing of the probe field and noise signal due to the AC Stark shift leads to a clear decrease in Λ when the probe field frequency overlaps with the Lorentzian noise spectrum. No such decrease is observed for the reference measurement, as the noise signal is weak and detuned from the NV bare resonance by $\Delta = 25$ MHz. Here, the frequency zero on the x-axis is about 2.903 GHz. The MW switches induce an offset of about -0.3 rad in the NV spin phase determination, as indicated in (b).

As the NVs in our experiments are also subject to environmental noise, we immediately follow each dressed state spin echo or Ramsey measurement with a reference measurement without the probe field applied; and then take the logarithm of the ratio of the resulting NV spin magnitudes (with and without probe field) to obtain the decoherence value. Fig. B.3 shows example data using the NV-diamond pillar for the probe field on and off, with application of a Lorentzian noise signal (as in Fig. 2.5, lowest panel). Figs. B.3(a,b) show results for the (unnormalized) NV spin magnitude and phase, respectively. For the scaling in Fig. 2.5 the data was normalized to 1s measurement time. This was done by taking the time per measurement ($t_{\text{measurement}} = 3700 + 540 + 2 * 4200$) and then obtaining a number for measurements per second ($N_{1s} = 1/t_{\text{measurement}}$). This

was then scaled with the actual taken measurements of $N_{total} = 16$mil by $A_{scale} = \sqrt{N_{total}}/N_{1s}$.

B.2.2 Experimental parameter calibrations and systematic dependencies

B.2.2.1 Probe field amplitude and NV phase variance

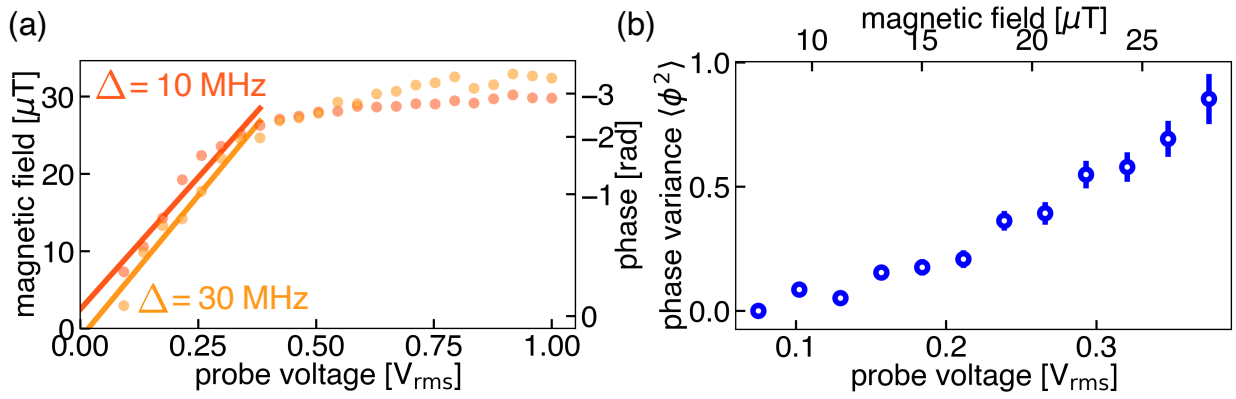


Figure B.4: Calibration of the probe field. (a) B_{probe} as a function of the voltage applied on the I and Q channels of the I-Q mixer and connected to MW2 to generate the probe field, for two values of probe field detuning Δ from the NV bare resonance. The output of the I-Q mixer saturates after the linear regime up to 0.4 V. The magnetic field is calculated from the accumulated phase. (b) NV phase variance $\langle\phi^2\rangle$ as a function of the probe I-Q voltage and hence B_{probe}, determined from dressed state spin echo measurements in the presence of the rectangular noise spectrum shown in Fig. 2.5.

Dressed state spin calibration measurements relate the voltage on the I-Q channels to the probe field magnetic field amplitude at the NV sensor. The calibration exploits the relation:

$$B_{\text{probe}} = \frac{\sqrt{2}}{\gamma}\Omega_{\text{probe}} = \frac{2}{\gamma}\sqrt{\frac{|\phi|\Delta}{\tau}} \tag{B.39}$$

which is a rewritten form of Eq. (2.6).

Example experimental results for this calibration are shown in Fig. B.4(a), where B_{probe} (given by Eq. B.39 from experimentally determined values for $|\phi|$ and control parameters τ and

Δ) is plotted against the probe field voltage of the I-Q mixer. This calibration shows that the output of the I-Q mixer saturates at approximately $0.4\ \mathrm{V_{rms}}$, a value we independently confirmed using a commercial spectrum analyzer (Signalhound SA1W24B). For the experimental results presented in Chapter 2 and elsewhere in this appendix, we only use the linear regime up to $0.4\ \mathrm{V_{rms}}$.

To calibrate the induced NV phase variance $\langle\phi^2\rangle$ for a given voltage of the I-Q mixer (and hence probe field amplitude B_{probe}), we employ the rectangular noise spectrum shown in Fig. 2.5, and with the probe field frequency tuned to be at the center of the noise band. Fig. B.4(b) displays the experimentally determined phase variance $\langle\phi^2\rangle$ and the corresponding I-Q mixer voltage, as well as B_{probe} at the NV center determined from the calibration obtained in panel (a).

Each data point displayed in Fig. B.4 results from averaging over $2 \cdot 10^6$experiment repetitions, implying that each of the 100 noise time traces uploaded to the AWG is repeated (looped) about $2 \cdot 10^4$ times per data point.

B.2.2.2 τ dependence

To investigate how the pulse sequence length influences the NV spin variance $\langle\phi^2\rangle$ we repeat the dressed state spin echo measurement for different echo-arm durations τ ranging from 0 to 5000 ns. To obtain the one-dimensional spectral representation in Fig. 2.6, we define a noise signal region corresponding to the frequency band f_k in Eq. 2.3, i.e., the frequencies at which noise is applied, with BW $=$ 1 MHz. We then average all data points within this band and normalize the result by a reference region far detuned from the signal noise region. The reference region is

defined as the frequency intervals in which no noise is applied,

$$f_{\text{probe}} \notin \left[f_{\text{noise}} - \frac{\text{BW}}{2},\ f_{\text{noise}} + \frac{\text{BW}}{2} \right]. \tag{B.40}$$

As shown in Fig. B.5, the data largely follows the expected linear scaling of $\langle \phi^2 \rangle$ with τ. However, for $\tau < 100$ ns the measured phase variance is reduced. This deviation at short echo times results from the filter function becoming broader than the applied noise bandwidth of 1 MHz, thereby no longer following the assumed limit of $S \gg W$ and thus decreasing the effective noise contribution.

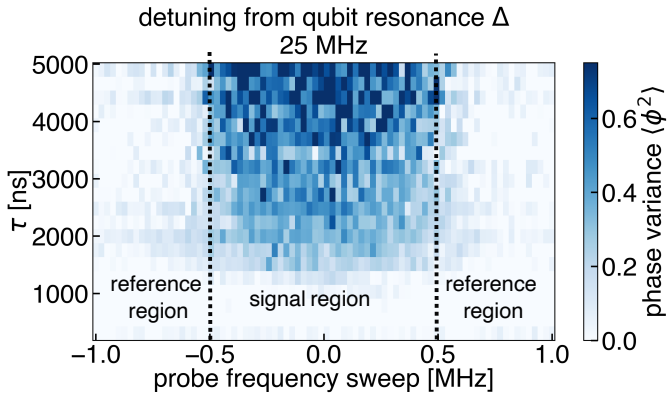


Figure B.5: 2D map of echo-arm duration τ dependency of the NV spin phase variance $\langle \phi^2 \rangle$. Defined signal and reference regions are used to normalize the data to a 1D spectral representation, as in Fig. 2.5.

B.2.2.3 Δ dependence

Fig. B.6 shows experimental characterization of the dependence of the qubit dressed state spectrum analyzer technique on probe field detuning Δ from the qubit bare resonance. The center frequency of an applied rectangular spectrum noise signal is iteratively shifted; and then NV dressed state spin echo measurements as a function of swept f_{probe} are performed as above, in the

large detuning limit, $\Delta \gg \Omega$. Similar to the characterization of τ dependence, defined signal and reference regions are used to obtain the results in Fig. 2.6.

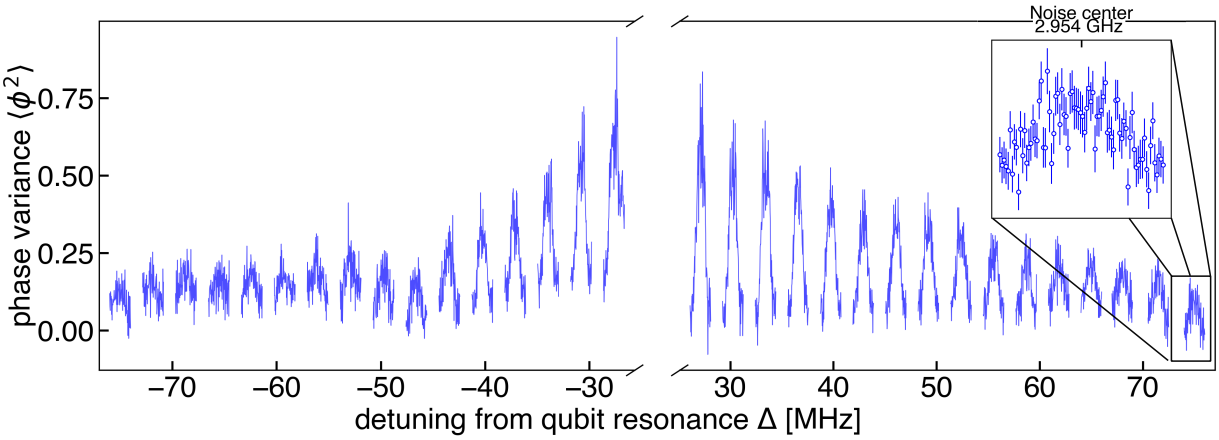


Figure B.6: Dependence of the NV spin phase variance $\langle\phi^2\rangle$ dependency on the probe field detuning Δ. For each value of the applied noise signal (with a rectangular spectrum), dressed state spin echo measurements are performed and the probe field frequency is swept, as is done in Fig. B.3. The spectrum of the applied noise signal is then shifted by 2.5 MHz; and the dressed state spin echo measurements, with sweeping of the probe field frequency, are repeated. The Rabi rate Ω used for the measurements is $\sim$ 2.5 MHz, thus enabling operation in the large detuning regime, $\Omega \ll \Delta$.

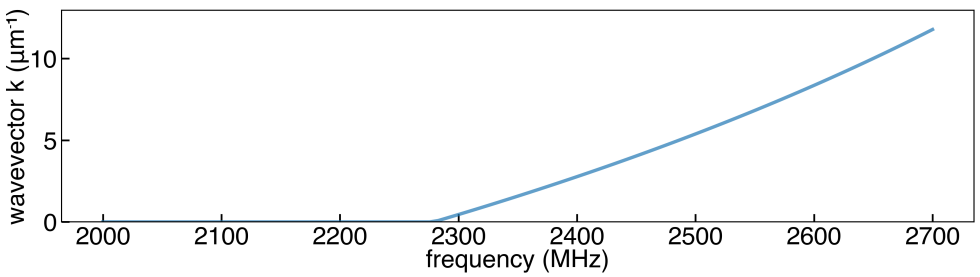


Figure B.7: Dispersion relation of Damon-Eshbach magnons. The frequency range of the x-axis is scaled to the relevant frequency range for NV measurements reported here. The YIG film ferromagnetic resonance (FMR) is at ≈ 2280 MHz for bias magnetic field $B_{\text{ext}} = 303$ G.

B.3 YIG

B.3.1 Damon-Eshbach magnons

Consistent with the literature for similar samples we find that the most relevant magnons for our measurement are Damon-Eshbach modes within the YIG film. The dispersion relation of Damon-Eshbach magnons in a film of thickness l can be written, in the magnetostatic limit, as

$$f_{\text{DE}}(k) = \gamma \sqrt{\left[B_{\text{ext}} + \frac{M_s}{2}\right]^2 - \left(\frac{M_s}{2}\right)^2 e^{-2kl}}, \tag{B.41}$$

where $f_{\text{DE}}(k)$ is the Damon-Eshbach magnon frequency, k is the in-plane wavevector of the spin wave, l is the thickness of the magnetic film, B_{ext} is the magnitude of the external magnetic field component along the NV axis, and M_s is the saturation magnetization [30].

For this experimental setup and YIG sample, the relevant parameters are $B_{\text{ext}} = 303$ G, $M_s = 1850$ G, and a film thickness of 100 nm. For this configuration, varying k traces out the Damon-Eshbach dispersion branch. This expected dispersion is displayed in Fig. B.7, indicating that the FMR (i.e., $k \approx 0$ magnon mode) is around 2280 MHz.

B.3.2 Characterization by NV ODMR and T_1 measurements

From previous NV measurements on a similar YIG film [42] $B_{\text{ext}} \approx 303$ G along the NV sensing axis is required for the FMR to have a higher frequency than the NV $f_{0\rightarrow -1}$ transition. This is crucial as the noise of the thermal magnons would otherwise directly decohere the NV spins. For this bias magnetic field, the NV bare resonance is at 2020 MHz while the magnon band begins around 2280 MHz.

To check these assumptions continuous NV ODMR measurements are performed, with the probe field driven by the stripline antenna and swept in frequency from about 2000 to 2400 MHz. As seen in Fig. B.8(a), the NV bare resonance is observed at 2020 MHz via a sharp decrease in NV PL contrast, consistent with direct drive of this transition by the probe field generated by the stripline antenna. A second, broad ODMR feature (reduction in NV PL contrast) is observed around 2275 MHz consistent with the stripline driving magnons in the YIG film, which then scatter and drive the $0 \rightarrow +1$ transition. The frequency onset of this FMR is consistent with the predicted dispersion relation, see Fig. B.7. The power to the stripline antenna is -20 dBm.

It is also important to test whether the observed decrease in NV PL contrast has an impact on timescales relevant for dressed state spectrum analyzer YIG measurements. This test is crucial to rule out that the observed decrease in NV spin magnitude Λ in a spectrum analyzer measurement arises from enhanced T_1 spin relaxation (e.g., from resonant drive or FMR-induced noise at the NV resonance) instead of the assumed NV spin decoherence induced by the AC Stark shift mixterm, as manifested in changes in the NV spin phase variance $\langle \phi^2 \rangle$. The test consists of a modified NV T_1 measurement consisting of (i) laser initialization and readout pulses, each 6 μs long and (ii) two $\tau = 500$ ns pulses of the probe field between the laser pulses, with a brief delay (110 ns) between

the probe field pulses. The frequency f_{probe} of the probe field pulses is then iterated across a range of about 600 MHz and the modified T_1 measurement is repeated for each f_{probe} value. Finally, the entire suite of measurements is repeated for three probe field powers (-25 dBm, -20 dBm, and -15 dBm). The 500 ns duration of the two probe field pulses is chosen to be consistent with the typical pulse durations used in the YIG experiments reported in Chapter 2. The result of this modified T_1 test, shown in Fig.B.8(b) confirms that FMR-enhanced NV T_1 relaxation is insignificant on the timescales of our YIG measurements.

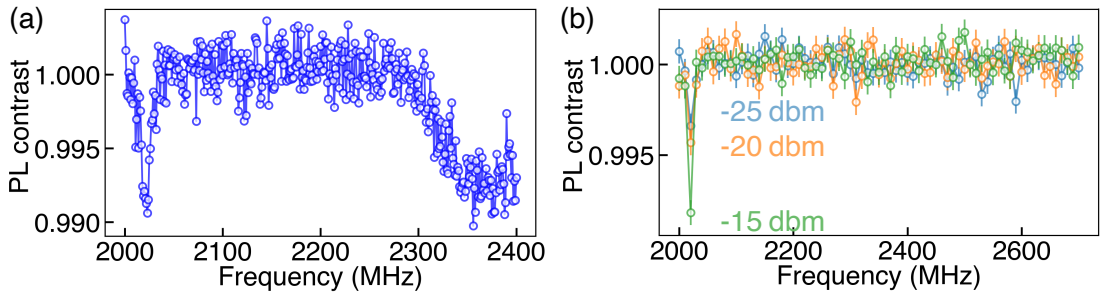


Figure B.8: Characterization of effect of YIG film on NV PL behavior in presence of probe field drive by the stripline antenna. (a) Continuous NV ODMR measurement with probe field frequency iteratively swept over about 400 MHz, from the expected NV resonance to the FMR of the YIG film. The applied probe field power is -20 dBm. (b) Modified NV T_1 measurements for a timescale used in the dressed state spectrum analyzer pulse sequences (500 ns) rule out FMR-enhanced longitudinal NV spin relaxation as the origin of observed decreases in NV PL contrast and NV spin magnitude far from the NV bare resonance. Consistent results are found for three probe field powers.

B.3.3 Fits

Spin Echo For the fit of the magnon spectra measured using the dressed state spin echo sequence, the following equation is used:

$$\mathcal{S}_s(f) \approx \int \mathrm{d}\mathbf{k} \cdot n(f,\mu)\, F(k,d)\, D(f,k) \approx n(f,\mu) \int \mathrm{d}\mathbf{k}' \cdot \delta_{k'-k(f)} k'\, e^{-2dk'} \left(1 - e^{-2t_{\text{yig}}k'}\right) \tag{B.42}$$

Here $n(f,\mu) = \frac{k_B T}{hf-\mu}$ is the Rayleigh-Jeans distribution for which we estimate $\mu = 0$ as the probe field driving the magnons is relatively weak compared to past work and the fit is used for qualitative interpretation. $F(k,d)$ is a filter function describing the field outside of the 2D plane. In this context t_{yig} is the thickness of the YIG film, in our case 100 nm [7]. $D(f,k)$ denotes the magnon spectral density which we estimate here as $D(f,k) = \frac{1}{\pi}\frac{W}{W^2+[k(f)-k]^2} \approx \delta_{k'-k(f)}$ given that the FMR spectrum is much narrower than that of the YIG thermal noise. $k(f)$ is the dispersion relation of eq. B.41.

Inserting these relations into Eq. (2.7) gives the final fit function:

$$\langle\phi^2\rangle(f_{\text{probe}}; A, d) = A \cdot \frac{1}{\Delta^2} \cdot \frac{k_B T}{h f_{\text{probe}}} \cdot k(f_{\text{probe}})^2 \, e^{-2dk(f_{\text{probe}})} \left(1 - e^{-2t_{\text{yig}} k(f_{\text{probe}})}\right). \tag{B.43}$$

where we assumed the broad noise limit discussed in Appendix B.1.3 for the frequency filter and included all prefactors besides the detuning scaling $\frac{1}{\Delta^2}$ into the amplitude A. *Note: the additional k is due to the volume element of the 2D integral.*

Ramsey For the Ramsey measurements we use:

$$\begin{aligned}\langle\phi^2\rangle(f_{\text{probe}}) &\propto (B_{\text{stripline}}\chi(k,f))^2 \\ &\approx \left(\int \mathrm{d}\mathbf{k} \cdot L(k,d)\, D(f,k)\right)^2 \approx \left(\int \mathrm{d}\mathbf{k}' \cdot \delta_{k'-k(f_{\text{probe}})} \,\mathrm{sinc}(k' \cdot x_{\text{stripline}}/2)\right)^2\end{aligned} \tag{B.44}$$

Here we introduce the stripline antenna filter function $L(k,l)$. We approximate this filter by assuming that the antenna has a rectangular shape in the x-z plane. In that case we get $L(k,d) =$

$\mathrm{sinc}(k' \cdot x_{\text{stripline}}/2)$, as all the launched magnons under the stripline interfere and thereby effectively create a Fourier transform of the stripline. The final fit function is then:

$$\langle \phi^2 \rangle (f; A, x_{\text{stripline}}) = A \cdot \frac{1}{\Delta^2} \cdot \sin(\pi \cdot k(f_{\text{probe}}) \cdot x_{\text{stripline}}/2)^2, \tag{B.45}$$

where the π originates from the sinc definition. When assuming the linear dispersion relation $k \propto f$, we can additionally take a Fourier transform of the data from the oscillations of $\langle \phi^2 \rangle$ as a function of probe frequency in the range $f_{\text{probe}} = [2400, 2650]$ MHz (see Fig. 2.7 (c)) and determine the oscillation spacing of about 100 MHz, which corresponds to a magnon group velocity $v_{\text{magnon}} \approx 1450 \frac{\text{m}}{\text{s}}$.

Bibliography

[1] C. L. Degen, F. Reinhard, and P. Cappellaro. Quantum sensing. *Reviews of Modern Physics*, 89(3):035002, July 2017.

[2] Francesco Casola, Toeno van der Sar, and Amir Yacoby. Probing condensed matter physics with magnetometry based on nitrogen-vacancy centres in diamond. *Nature Reviews Materials*, 3:17088, 2018.

[3] L Rondin, J-P Tetienne, T Hingant, J-F Roch, P Maletinsky, and V Jacques. Magnetometry with nitrogen-vacancy defects in diamond. *Reports on Progress in Physics*, 77(5):056503, May 2014.

[4] Jared Rovny, Sarang Gopalakrishnan, Ania C. Bleszynski Jayich, Patrick Maletinsky, Eugene Demler, and Nathalie P. De Leon. Nanoscale diamond quantum sensors for many-body physics. *Nature Reviews Physics*, 6(12):753–768, November 2024.

[5] A A Serga, A V Chumak, and B Hillebrands. YIG magnonics. *Journal of Physics D: Applied Physics*, 43(26):264002, July 2010.

[6] A. V. Chumak, V. I. Vasyuchka, A. A. Serga, and B. Hillebrands. Magnon spintronics. *Nature Physics*, 11(6):453–461, June 2015.

[7] Toeno van der Sar, Francesco Casola, Ronald Walsworth, and Amir Yacoby. Nanometre-scale probing of spin waves using single electron spins. *Nature Communications*, 6(1):7886, August 2015.

[8] Iacopo Bertelli, Joris J. Carmiggelt, Tao Yu, Brecht G. Simon, Coosje C. Pothoven, Gerrit E. W. Bauer, Yaroslav M. Blanter, Jan Aarts, and Toeno van der Sar. Magnetic resonance imaging of spin-wave transport and interference in a magnetic insulator. *Science Advances*, 6(46):eabd3556, November 2020.

[9] Guoqing Wang, Yi-Xiang Liu, Jennifer M. Schloss, Scott T. Alsid, Danielle A. Braje, and Paola Cappellaro. Sensing of Arbitrary-Frequency Fields Using a Quantum Mixer. *Physical Review X*, 12(2):021061, June 2022.

[10] Sandra H. Skjærvø, Christopher H. Marrows, Robert L. Stamps, and Laura J. Heyderman. Advances in artificial spin ice. *Nature Reviews Physics*, 2:13–28, 2020.

[11] Jiashen Tang, Zechuan Yin, Connor A. Hart, John W. Blanchard, Jner Tzern Oon, Smriti Bhalerao, Jennifer M. Schloss, Matthew J. Turner, and Ronald L. Walsworth. Quantum diamond microscope for dynamic imaging of magnetic fields. *AVS Quantum Sci.*, 5:044403, 2023.

[12] Anatoli Polkovnikov, Krishnendu Sengupta, Alessandro Silva, and Mukund Vengalattore. Colloquium: Nonequilibrium dynamics of closed interacting quantum systems. *Rev. Mod. Phys.*, 83:863–883, Aug 2011.

[13] Marcos Rigol, Vanja Dunjko, and Maxim Olshanii. Thermalization and its mechanism for generic isolated quantum systems. *Nature*, 452(7189):854–858, 2008.

[14] Rahul Nandkishore and David A. Huse. Many-body localization and thermalization in quantum statistical mechanics. *Annual Review of Condensed Matter Physics*, 6(1):15–38, 2015.

[15] Vladimir E. Zakharov, Victor S. L'vov, and Gregory Falkovich. *Kolmogorov Spectra of Turbulence I: Wave Turbulence*. Springer-Verlag, Berlin, 1992.

[16] Sergey Nazarenko. *Wave Turbulence*, volume 825 of *Lecture Notes in Physics*. Springer, Berlin, Heidelberg, 2011.

[17] Jürgen Berges, Michal P. Heller, Aleksas Mazeliauskas, and Raju Venugopalan. Qcd thermalization: Ab initio approaches and interdisciplinary connections. *Rev. Mod. Phys.*, 93:035003, Aug 2021.

[18] K. Hasselmann. On the non-linear energy transfer in a gravity-wave spectrum. part 1. General theory. *Journal of Fluid Mechanics*, 12(4):481–500, 1962.

[19] S. Y. Annenkov and V. I. Shrira. Spectral evolution of weakly nonlinear random waves: kinetic description versus direct numerical simulations. *Journal of Fluid Mechanics*, 844:766–795, 2018.

[20] Logan W. Clark, Anita Gaj, Lei Feng, and Cheng Chin. Collective emission of matter-wave jets from driven Bose–Einstein condensates. *Nature*, 551(7680):356–359, November 2017.

[21] Han Fu, Lei Feng, Brandon M. Anderson, Logan W. Clark, Jiazhong Hu, Jeffery W. Andrade, Cheng Chin, and K. Levin. Density Waves and Jet Emission Asymmetry in Bose Fireworks. *Physical Review Letters*, 121(24):243001, December 2018.

[22] J. H. V. Nguyen, M. C. Tsatsos, D. Luo, A. U. J. Lode, G. D. Telles, V. S. Bagnato, and R. G. Hulet. Parametric Excitation of a Bose-Einstein Condensate: From Faraday Waves to Granulation. *Physical Review X*, 9(1):011052, March 2019.

[23] Keisuke Fujii, Sarah L. Görlitz, Nikolas Liebster, Marius Sparn, Elinor Kath, Helmut Strobel, Markus K. Oberthaler, and Tilman Enss. Stable-fixed-point description of square-pattern formation in driven two-dimensional bose-einstein condensates. *Physical Review A*, 109(5):L051301, 2024.

[24] Nikolas Liebster, Marius Sparn, Elinor Kath, Jelte Duchene, Keisuke Fujii, Sarah L. Görlitz, Tilman Enss, Helmut Strobel, and Markus K. Oberthaler. Observation of pattern stabilization in a driven superfluid. *Physical Review X*, 15(1):011026, 2025.

[25] P. G. Savvidis, J. J. Baumberg, R. M. Stevenson, M. S. Skolnick, D. M. Whittaker, and J. S. Roberts. Angle-Resonant Stimulated Polariton Amplifier. *Physical Review Letters*, 84(7):1547–1550, February 2000.

[26] Jeremy J. Baumberg and Pavlos G. Lagoudakis. Parametric amplification and polariton liquids in semiconductor microcavities. *physica status solidi (b)*, 242(11):2210–2223, September 2005.

[27] S. O. Demokritov, V. E. Demidov, O. Dzyapko, G. A. Melkov, A. A. Serga, B. Hillebrands, and A. N. Slavin. Bose–Einstein condensation of quasi-equilibrium magnons at room temperature under pumping. *Nature*, 443(7110):430–433, September 2006.

[28] Alexander A. Serga, Vasil S. Tiberkevich, Christian W. Sandweg, Vitaliy I. Vasyuchka, Dmytro A. Bozhko, Andrii V. Chumak, Timo Neumann, Björn Obry, Gennadii A. Melkov, Andrei N. Slavin, and Burkard Hillebrands. Bose–Einstein condensation in an ultra-hot gas of pumped magnons. *Nature Communications*, 5(1):3452, March 2014.

[29] V. E. Demidov, O. Dzyapko, S. O. Demokritov, G. A. Melkov, and A. N. Slavin. Thermalization of a Parametrically Driven Magnon Gas Leading to Bose-Einstein Condensation. *Physical Review Letters*, 99(3):037205, July 2007.

[30] Chunhui Du, Toeno van der Sar, Tony X. Zhou, Pramey Upadhyaya, Francesco Casola, Huiliang Zhang, Mehmet C. Onbasli, Caroline A. Ross, Ronald L. Walsworth, Yaroslav Tserkovnyak, and Amir Yacoby. Control and local measurement of the spin chemical potential in a magnetic insulator. *Science*, 357(6347):195–198, July 2017.

[31] Thomas Sebastian, Katrin Schultheiss, BjÃ¶rn Obry, Burkard Hillebrands, and Helmut Schultheiss. Micro-focused Brillouin light scattering: imaging spin waves at the nanoscale. *Frontiers in Physics*, 3, June 2015.

[32] H. Schultheiss, K. Vogt, and B. Hillebrands. Direct observation of nonlinear four-magnon scattering in spin-wave microconduits. *Physical Review B*, 86(5):054414, August 2012.

[33] Victor S. L'vov. *Wave Turbulence Under Parametric Excitation: Applications to Magnets*. Springer Series in Nonlinear Dynamics. Springer Berlin Heidelberg, Berlin, Heidelberg, 1994.

[34] Sergio M. Rezende and Flavio M. de Aguiar. Spin-wave instabilities, auto-oscillations, and chaos in yttrium-iron-garnet. *Proceedings of the IEEE*, 78(6):893–908, 1990.

[35] Marin Soljačić, Steven G. Johnson, Shanhui Fan, Mihai Ibanescu, Erich Ippen, and J. D. Joannopoulos. Photonic-crystal slow-light enhancement of nonlinear phase sensitivity. *Journal of the Optical Society of America B*, 19(9):2052–2059, 2002.

[36] Yohei Hamachi, Shousaku Kubo, and Toshihiko Baba. Slow light with low dispersion and nonlinear enhancement in a lattice-shifted photonic crystal waveguide. *Optics Letters*, 34(7):1072–1074, 2009.

[37] Robert W. Boyd. Material slow light and structural slow light: similarities and differences for nonlinear optics. *Journal of the Optical Society of America B*, 28(12):A38–A44, 2011.

[38] Shahidul Asif, Hang Chen, Johannes Cremer, Shantam Ravan, Jeyson Támara-Isaza, Sagar Lamsal, Reza Ebadi, Yonglong Li, Ling-Jie Zhou, Cui-Zu Chang, John Q. Xiao, Amir Yacoby, Ronald L. Walsworth, and Mark J. H. Ku. Diamond micro-chip for quantum microscopy. *AVS Quantum Science*, 6(4):044405, 2024.

[39] J. F. Barry, J. M. Schloss, E. Bauch, M. J. Turner, C. A. Hart, L. M. Pham, and R. L. Walsworth. Sensitivity optimization for NV-diamond magnetometry. *Reviews of Modern Physics*, 92(1):015004, 2020.

[40] M. J. H. Ku, T. X. Zhou, Q. Li, Y. J. Shin, J. K. Shi, C. Burch, L. E. Anderson, A. T. Pierce, Y. Xie, A. Hamo, U. Vool, H. Zhang, F. Casola, T. Taniguchi, K. Watanabe, M. M. Fogler, P. Kim, A. Yacoby, and R. L. Walsworth. Imaging viscous flow of the Dirac fluid in graphene. *Nature*, 583(7817):537–541, 2020.

[41] B A Kalinikos and A N Slavin. Theory of dipole-exchange spin wave spectrum for ferromagnetic films with mixed exchange boundary conditions. *Journal of Physics C: Solid State Physics*, 19(35):7013–7033, December 1986.

[42] Tony X. Zhou, Joris J. Carmiggelt, Lisa M. Gächter, Ilya Esterlis, Dries Sels, Rainer J. Stöhr, Chunhui Du, Daniel Fernandez, Joaquin F. Rodriguez-Nieva, Felix Büttner, Eugene Demler, and Amir Yacoby. A magnon scattering platform. *Proceedings of the National Academy of Sciences*, 118(25):e2019473118, June 2021.

[43] Harry Suhl. The theory of ferromagnetic resonance at high signal powers. *Journal of Physics and Chemistry of Solids*, 1(4):209–227, 1957.

[44] T. Hula, K. Schultheiss, F. J. T. Gonçalves, L. Körber, M. Bejarano, M. Copus, L. Flacke, L. Liensberger, A. Buzdakov, A. Kákay, M. Weiler, R. Camley, J. Fassbender, and H. Schultheiss. Spin-wave frequency combs. *Applied Physics Letters*, 121(11):112404, September 2022.

[45] Joris J. Carmiggelt, Iacopo Bertelli, Roland W. Mulder, Annick Teepe, Mehrdad Elyasi, Brecht G. Simon, Gerrit E. W. Bauer, Yaroslav M. Blanter, and Toeno van der Sar. Broadband microwave detection using electron spins in a hybrid diamond-magnet sensor chip. *Nature Communications*, 14(1):490, January 2023.

[46] W. Wettling, W. D. Wilber, P. Kabos, and C. E. Patton. Light scattering from parallel-pump instabilities in yttrium iron garnet. *Physical Review Letters*, 51:1680–1683, 1983.

[47] Pavol Krivosik and Carl E. Patton. Hamiltonian formulation of nonlinear spin-wave dynamics: Theory and applications. *Physical Review B*, 82(18):184428, November 2010.

[48] H. J. Jason Liu, Grant A. Riley, César L. Ordóñez-Romero, Boris A. Kalinikos, and Kristen S. Buchanan. Time-resolved study of nonlinear three-magnon processes in yttrium iron garnet films. *Physical Review B*, 99:024429, 2019.

[49] Ruolan Xue, Nikola Maksimovic, Pavel E. Dolgirev, Li-Qiao Xia, Aaron Müller, Ryota Kitagawa, Francisco Machado, Dahlia R. Klein, David MacNeill, Kenji Watanabe, Takashi Taniguchi, Pablo Jarillo-Herrero, Mikhail D. Lukin, Eugene Demler, and Amir Yacoby. Magnon hydrodynamics in an atomically thin ferromagnet. *Science*, 392(6800):873–878, May 2026.

[50] Xiao Xiao, Masahiro O. Takahashi, Paul Stevenson, Satoshi Fujimoto, and Arun Bansil. Signatures of non-Abelian Kitaev quantum spin liquids in noise magnetometry. *Physical Review B*, 113(20):L201103, May 2026.

[51] Patrick A. Lee and Sid Morampudi. Proposal to detect emergent gauge field and its Meissner effect in spin liquids using NV centers. *Physical Review B*, 107(19):195102, May 2023.

[52] Jonathan B. Curtis, Nikola Maksimovic, Nicholas R. Poniatowski, Amir Yacoby, Bertrand Halperin, Prineha Narang, and Eugene Demler. Probing the Berezinskii-Kosterlitz-Thouless vortex unbinding transition in two-dimensional superconductors using local noise magnetometry. *Physical Review B*, 110(14):144518, October 2024. arXiv:2404.06147 [cond-mat].

[53] Zhongyuan Liu, Ruotian Gong, Jaewon Kim, Oriana K. Diessel, Qiaozhi Xu, Zackary Rehfuss, Xinyi Du, Guanghui He, Abhishek Singh, Yun Suk Eo, Erik A. Henriksen, G. D. Gu, Norman Y. Yao, Francisco Machado, Sheng Ran, Shubhayu Chatterjee, and Chong Zu. Quantum noise spectroscopy of superconducting dynamics in thin film Bi$_2$Sr$_2$CaCu$_2$O$_{8+\delta}$, February 2025. arXiv:2502.04439 [cond-mat].

[54] B. I. Halperin and P. C. Hohenberg. Hydrodynamic Theory of Spin Waves. *Physical Review*, 188(2):898–918, December 1969.

[55] Nabeel Aslam, Hengyun Zhou, Elana K. Urbach, Matthew J. Turner, Ronald L. Walsworth, Mikhail D. Lukin, and Hongkun Park. Quantum sensors for biomedical applications. *Nature Reviews Physics*, 5(3):157–169, February 2023.

[56] David R. Glenn, Dominik B. Bucher, Junghyun Lee, Mikhail D. Lukin, Hongkun Park, and Ronald L. Walsworth. High-resolution magnetic resonance spectroscopy using a solid-state spin sensor. *Nature*, 555(7696):351–354, March 2018.

[57] N. Bar-Gill, L.M. Pham, C. Belthangady, D. Le Sage, P. Cappellaro, J.R. Maze, M.D. Lukin, A. Yacoby, and R. Walsworth. Suppression of spin-bath dynamics for improved coherence of multi-spin-qubit systems. *Nature Communications*, 3(1):858, May 2012.

[58] Philipp Hauke, Markus Heyl, Luca Tagliacozzo, and Peter Zoller. Measuring multipartite entanglement through dynamic susceptibilities. *Nature Physics*, 12(8):778–782, August 2016.

[59] E. L. Hahn. Spin Echoes. *Physical Review*, 80(4):580–594, November 1950.

[60] G. De Lange, Z. H. Wang, D. Ristè, V. V. Dobrovitski, and R. Hanson. Universal Dynamical Decoupling of a Single Solid-State Spin from a Spin Bath. *Science*, 330(6000):60–63, October 2010.

[61] J. M. Taylor, P. Cappellaro, L. Childress, L. Jiang, D. Budker, P. R. Hemmer, A. Yacoby, R. Walsworth, and M. D. Lukin. High-sensitivity diamond magnetometer with nanoscale resolution. *Nature Physics*, 4(10):810–816, October 2008.

[62] Jonas Meinel, MinSik Kwon, Rouven Maier, Durga Dasari, Hitoshi Sumiya, Shinobu Onoda, Junichi Isoya, Vadim Vorobyov, and Jörg Wrachtrup. High-resolution nanoscale NMR for arbitrary magnetic fields. *Communications Physics*, 6(1):302, October 2023.

[63] S. Cronenberger, D. Scalbert, D. Ferrand, H. Boukari, and J. Cibert. Atomic-like spin noise in solid-state demonstrated with manganese in cadmium telluride. *Nature Communications*, 6(1):8121, September 2015.

[64] Han Sae Jung, Johannes Cremer, Aoyang Zhang, Shuhao Fan, Sangha Kim, Guang Yang, Ronald L. Walsworth, and Donhee Ham. Impedance-Tuned Microwave Loop for Fast, Homogeneous Rabi Oscillations of a Dense Ensemble of NV-Diamond Electronic Spins. *Nano Letters*, 25(43):15566–15571, October 2025.

[65] G. D. Fuchs, V. V. Dobrovitski, D. M. Toyli, F. J. Heremans, and D. D. Awschalom. Gigahertz Dynamics of a Strongly Driven Single Quantum Spin. *Science*, 326(5959):1520–1522, December 2009.

[66] Farshad Foroughi, Jan-Michael Mol, Tristan Mueller, John R. Kirtley, Kathryn A. Moler, and Hendrik Bluhm. A micro-SQUID with dispersive readout for magnetic scanning microscopy. *Applied Physics Letters*, 112(25):252601, June 2018. arXiv:1803.07636 [cond-mat].

[67] Zechuan Yin, Justin J. Welter, Connor A. Hart, Paul V. Petruzzi, and Ronald L. Walsworth. High-resolution and wide-frequency-range magnetic spectroscopy with solid-state spin ensembles. *npj Quantum Information*, 11(1):190, December 2025.

[68] Changjiang Wei, Andrew S M Windsor, and Neil B Manson. A strongly driven two-level atom revisited: Bloch - Siegert shift versus dynamic Stark splitting. *Journal of Physics B: Atomic, Molecular and Optical Physics*, 30(21):4877–4888, November 1997.

[69] J. R. Maze, P. L. Stanwix, J. S. Hodges, S. Hong, J. M. Taylor, P. Cappellaro, L. Jiang, M. V. Gurudev Dutt, E. Togan, A. S. Zibrov, A. Yacoby, R. L. Walsworth, and M. D. Lukin. Nanoscale magnetic sensing with an individual electronic spin in diamond. *Nature*, 455(7213):644–647, October 2008.

[70] Francisco Machado, Eugene A. Demler, Norman Y. Yao, and Shubhayu Chatterjee. Quantum Noise Spectroscopy of Dynamical Critical Phenomena. *Physical Review Letters*, 131(7):070801, August 2023.

[71] Gang-Qin Liu, Yu-Ran Zhang, Yan-Chun Chang, Jie-Dong Yue, Heng Fan, and Xin-Yu Pan. Demonstration of entanglement-enhanced phase estimation in solid. *Nature Communications*, 6(1):6726, April 2015.

[72] Xu Zhou, Mengqi Wang, Xiangyu Ye, Haoyu Sun, Yuhang Guo, Shuo Han, Zihua Chai, Wentao Ji, Kangwei Xia, Fazhan Shi, Ya Wang, and Jiangfeng Du. Entanglement-enhanced nanoscale single-spin sensing. *Nature*, 647(8091):883–888, November 2025.

[73] Richard R. Allen, Francisco Machado, Isaac L. Chuang, Hsin-Yuan Huang, and Soonwon Choi. Quantum Computing Enhanced Sensing, January 2025. arXiv:2501.07625 [quant-ph].

[74] Peter Schiffer and Cristiano Nisoli. Artificial spin ice: Paths forward. *Applied Physics Letters*, 118(11):110501, 2021.

[75] Rawnak Sultana, Amrit Kumar Mondal, Vinayak Shantaram Bhat, Kilian Stenning, Yue Li, Daan M. Arroo, Aastha Vasdev, Margaret R. McCarter, Lance E. De Long, J. Todd Hastings, Jack C. Gartside, and M. Benjamin Jungfleisch. Artificial spin ice: A tutorial on design and control of geometry, microstate, magnon dynamics & neuromorphic computing. *Journal of Applied Physics*, 138(6):061101, 2025.

[76] Kevin Hofhuis, Sandra H. Skjærvø, Sergii Parchenko, Hanu Arava, Zhaochu Luo, Armin Kleibert, Peter M. Derlet, and Laura J. Heyderman. Real-space imaging of phase transitions in bridged artificial kagome spin ice. *Nature Physics*, 18:699–705, 2022.

[77] Susan Kempinger, Robert D. Fraleigh, Paul E. Lammert, Sheng Zhang, Vincent H. Crespi, Peter Schiffer, and Nitin Samarth. Imaging the stochastic microstructure and dynamic development of correlations in perpendicular artificial spin ice. *Phys. Rev. Research*, 2:012001(R), 2020.

[78] Yue Li, Gary W. Paterson, Gavin M. MacAuley, Fabio S. Nascimento, Ciaran Ferguson, Sophie A. Morley, Mark C. Rosamond, Edmund H. Linfield, Donald A. MacLaren, Rair MacEdo, Christopher H. Marrows, Stephen McVitie, and Robert L. Stamps. Superferromagnetism and domain-wall topologies in artificial pinwheel spin ice. *ACS Nano*, 13:2213–2222, 2019.

[79] E. Mengotti, L. J. Heyderman, A. Fraile Rodríguez, F. Nolting, R. V. Hügli, and H.-B. Braun. Real-space observation of emergent magnetic monopoles and associated dirac strings in artificial kagome spin ice. *Nature Physics*, 7:68–74, 2011.

[80] Jared Rovny, Sarang Gopalakrishnan, Ania C. Bleszynski Jayich, Patrick Maletinsky, Eugene Demler, and Nathalie P. de Leon. Nanoscale diamond quantum sensors for many-body physics. *Nature Reviews Physics*, 6:753–768, 2024.

[81] Ephraim Spindler, Vinayak Shantaram Bhat, Elke Neu, Mathias Weiler, and M. Benjamin Jungfleisch. Nanoscale dipolar fields in artificial spin ice probed by scanning nv magnetometry. *arXiv:2509.02233*, 2025.

[82] Arjen van den Berg, Peter Rickhaus, Frank Barrows, Cristiano Nisoli, and Sam Ladak. Direct visualization of the magnetic monopole field in a 3d artificial spin ice. *arXiv:2511.04877*, 2025.

[83] Shahidul Asif, Hang Chen, Johannes Cremer, Shantam Ravan, Jeyson Támara-Isaza, Saurabh Lamsal, Reza Ebadi, Yan Li, Ling-Jie Zhou, Cui-Zu Chang, John Q Xiao, Amir Yacoby, Ronald L Walsworth, and Mark J H Ku. Diamond micro-chip for quantum microscopy. *AVS Quantum Sci.*, 6:044405, 2024.

[84] N. S. Bingham, S. Rooke, J. Park, A. Simon, W. Zhu, X. Zhang, J. Batley, J. D. Watts, C. Leighton, K. A. Dahmen, and P. Schiffer. Experimental realization of the 1d random field ising model. *Phys. Rev. Lett.*, 127:207203, 2021.

[85] Arne Vansteenkiste, Jonathan Leliaert, Mykola Dvornik, Mathias Helsen, Felipe Garcia-Sanchez, and Bartel Van Waeyenberge. The design and verification of mumax3. *AIP Advances*, 4:107133, 2014.

[86] R. Engel-Herbert and T. Hesjedal. Calculation of the magnetic stray field of a uniaxial magnetic domain. *J. Appl. Phys.*, 97:074504, 2005.

[87] Xiechen Zheng, Jeyson Támara-Isaza, Zechuan Yin, Johannes Cremer, John W. Blanchard, Connor A. Hart, Michael Crescimanno, Paul V. Petruzzi, Matthew J. Turner, and Ronald L. Walsworth. All-optical photoluminescence response of nitrogen-vacancy ensembles in diamond at low magnetic fields. *Phys. Rev. Applied*, 24:064049, 2025.

[88] A. Finco, A. Haykal, R. Tanos, F. Fabre, S. Chouaieb, W. Akhtar, I. Robert-Philip, W. Legrand, F. Ajejas, K. Bouzehouane, N. Reyren, T. Devolder, J.-P. Adam, J.-V. Kim, V. Cros, and V. Jacques. Imaging non-collinear antiferromagnetic textures via single spin relaxometry. *Nature Communications*, 12:767, 2021.

[89] Thomas Hingant, Jean-Philippe Tetienne, Loïc J. Martínez, Karim Garcia, Dafiné Ravelosona, Jean-François Roch, and Vincent Jacques. Measuring the magnetic moment density in patterned ultrathin ferromagnets with submicrometer resolution. *Phys. Rev. Applied*, 4:014003, 2015.

[90] Yuliya Dovzhenko, Francesco Casola, Stephen Schlotter, Tony X. Zhou, Felix Büttner, Ronald L. Walsworth, Geoffrey S. D. Beach, and Amir Yacoby. Magnetostatic twists in room-temperature skyrmions explored by nitrogen-vacancy center spin texture reconstruction. *Nature Communications*, 9:2712, 2018.

[91] Lucas Thiel, Zhe Wang, Märta A. Tschudin, Dominik Rohner, Ignacio Gutiérrez-Lezama, Nicolas Ubrig, Marco Gibertini, Enrico Giannini, Alberto F. Morpurgo, and Patrick Maletinsky. Probing magnetism in 2d materials at the nanoscale with single-spin microscopy. *Science*, 364:973–976, 2019.

[92] Johannes H. Jensen, Anders Strømberg, Odd Rune Lykkebø, Arthur Penty, Magnus Själander, Erik Folven, and Gunnar Tufte. flatspin: A large-scale artificial spin ice simulator. *Phys. Rev. B*, 106:064408, 2022.

[93] Avinash Rustagi, Iacopo Bertelli, Toeno van der Sar, and Pramey Upadhyaya. Sensing chiral magnetic noise via quantum impurity relaxometry. *Physical Review B*, 102(22):220403, December 2020.

[94] R. W. Damon and J. R. Eshbach. Magnetostatic modes of a ferromagnet slab. *Journal of Physics and Chemistry of Solids*, 19(3):308–320, May 1961.